UNIVERSITÉ DE GRENOBLE

THÈSE

pour obtenir le grade de

DOCTEUR d'Université de Grenoble

préparée au Laboratoire des Matériaux et du Génie Physique (LMGP) et au Laboratoire d'Electrochimie et de Physicochimie des Matériaux et des Interfaces (LEPMI)

Spécialité* : *« Physique pour Sciences du Vivant »

présentée et soutenue publiquement
par

Marius SOCOL

le 20 May 2010

La synchronisation électrochimique de l'étalement cellulaire sur des surfaces solides

Thèse dirigé par **M. Franz BRUCKERT** et
co-dirigé par **M. Didier DELABOUGLISE**

Jury

Jacques Derouard	Président
Annie Viallat	Rapporteur
Pierre Cosson	Rapporteur
Jean-Paul Rieu	Examinateur
Didier Delabouglise	Examinateur
Franz Bruckert	Examinateur

Remerciements

Je tiens tout d'abord à remercier infiniment mes directeurs de thèse, Messieurs **Franz Bruckert** et **Didier Delabouglise**, deux grands Professeurs et leur grand coeur.

Je remercie spécialement Madame **Marianne Weidenhaupt**, pour sa gentillesse, ses bonnes idées et conseils scientifiques et aussi pour son aide pour la correction de la thèse.

Un grand merci a mon meilleur ami, **Mihai Miron**, qui m'a convaincu de venir en France, pour toute son aide, morale, financière et scientifique: réalisation de lamelles recouvertes avec Ti, Pt et Au et les discussions en physique.

Je remercie beaucoup les personnes qui m'ont aidé pour la mesure du potentiel Zeta: **Eric Chainet**, **Carole Pernel** et **Guillaume Costa**.

Je remercie **Alain Denoyelle** et **Christine Lefrou** pour leurs conseils et discussions dans le domaine de l'électrochimie.

Je remercie les personnes suivantes, qui m'ont beaucoup aidé: **Bertrand Fourcade (CNRS), Gérard Klein, Laurence Aubry** et **Michel Satre (CEA)**.

Je remercie **Annie Viallat, Pierre Cosson, Jean-Paul Rieu, Jacques Derouard,** d'avoir bien voulu examiner ma thèse

Je remercie également l'**Ecole Doctorale de Physique de Grenoble et le soutien de la région (CPER, Macodev).**

Je remercie également mes collègues doctorants, **Sébastien Keller** qui m'a beaucoup aidé quand j'ai été stagiaire, **Renaud Cornut**, qui m'a beaucoup aidé dans les simulations en *Comsol*, **Mael Manesse**, **Paolo Actis, Laure Fourel, Ofelia Maniti, Germain Rey, Laurent Nault, Nicolas Chaban, Claire Holtzinger, Mouna Messaoud** et **Thomas Ballet** pour leur compagnie agréable et stimulante.

Je remercie tout particulièrement ma famille et spécialement mon épouse **Olga**, à qui je dédie cette thèse.

Présentation de la thèse

Le travail de cette thèse s'inscrit dans le cadre d'une recherche sur l'analyse biophysique de l'adhésion de l'amibe *Dictyostelium discoideum* sur son substrat.

Dictyostelium discoideum est une cellule eucaryote simple, qui possède un génome haploïde contenant un nombre de gènes égal à la moitié de celui du génome humaine et qui peut être manipulé avec des techniques standards de génétique moléculaire. Elle est capable d'adhérer et de s'étaler sur différents matériaux aux propriétés de surface assez variables. En conséquence, cette amibe est un très bon modèle expérimental pour étudier la formation de contacts cellule-surface.

Le contact d'une cellule avec une surface solide est un processus très complexe qui initie d'importants chemins de signalisation intracellulaire, conduisant à l'adhésion et l'étalement cellulaire, la polarisation, la motilité, la prolifération et parfois la différenciation.

Le nombre des protéines impliquées dans l'adhésion cellulaire est assez important et suppose beaucoup d'interactions moléculaires. En dépit de la connaissance de nombreux éléments qui jouent un rôle dans l'adhésion, leur hiérarchie temporelle et organisation spatiale ne sont que partiellement connues. Certaines protéines membranaires impliquées dans cette adhésion ont été découvertes. Quelques unes de ces protéines sont similaires aux intégrines qui interviennent dans l'interaction des cellules mammifères avec les protéines de la matrice extracellulaire. *Dictyostelium discoideum* possède aussi beaucoup de protéines connues comme faisant partie des structures d'adhésion chez cellules mammaliennes, comme par exemple la taline, la paxilin, la coronine, qui stimulent la polymérisation de l'actine et relient les microfilaments d'actine de la membrane plasmique.

En utilisant la «reflection interference contrast microscopy» (RICM), Sébastien Keller du groupe conduit par Franz Bruckert, a observé récemment que la cellule *Dictyostelium discoideum* s'étale avec une activité de protrusion périodique. La période des cycles d'activité est d'environ 11 secondes et les cycles persistent au moins durant l'étalement (approximativement 1 minute). Cette activité cyclique révèle une organisation temporelle très complexe des événements moléculaires qui conduisent à l'étalement.

C’est un défi d’identifier la formation successive des complexes protéiniques qui mènent à établir des contacts stables entre la surface et la cellule. Pour cela, il serait nécessaire de synchroniser le point de départ de l’étalement cellulaire pour avoir accès à différentes étapes de cette activité.

Notre objectif était de synchroniser le contact cellule-surface pour une population des cellules, ceci étant un élément déterminant pour préparer du matériel cellulaire enrichi avec des complexes des protéines actives après un certain temps après le contact.

Le mémoire de thèse commence par le chapitre **introduction** qui a deux parties. La première partie porte sur les paramètres biologiques qui influencent l’adhésion et l’étalement de l'amibe *Dictyostelium discoideum*, le modèle cellulaire utilisé tout au long de ce travail. Les mécanismes qui assurent l'adhésion des cellules sur leur substrat sont passés en revue. La deuxième partie donne un état de l’art de la manipulation des cellules avec des champs électriques. Les techniques existantes de manipulation des cellules sont exposées et leurs mécanismes physiques associés sont décrits par les concepts de base, les différentes forces et les grandeurs physiques mises en jeu.

Le chapitre deux est consacré aux **matériels et aux méthodes** et porte sur les méthodes expérimentales spécifiques développées pour synchroniser l’adhésion cellulaire des amibes. Les expériences d’électrochimie, les simulations numériques, les méthodes d’observation et les méthodes d’analyse y sont présentées. Cette description est accompagnée de considérations sur les bases physiques et biologiques des méthodes utilisées: principe de la double couche électrique et détail de la théorie de Gouy-Chapman, potentiel Zeta, théorie DLVO et modèle de l’adhérence cellulaire sur des surfaces chargées en fonction de la force ionique.

Le troisième chapitre est consacré aux **résultats**. Le premier sous chapitre concerne l’adhésion non synchrone (étalement des cellules sous l’influence de la gravité). On y confirme les études précédentes qui montrent que *Dictyostelium discoideum* s’étale avec une activité de protrusion périodique, associée à une polymérisation de l’actine (suivie par microscopie de fluorescence en utilisant des cellules marquées avec $LimE^{\Delta coil}$-GFP) selon des périodes similaires. L’influence du champ électrique sur des cellules adhérentes sur différents matériaux (ITO, Ti, Pt et Au) est ensuite étudiée. Des potentiels positifs mais aussi négatifs ont été testés. Cette partie est suivie d'une description des

paramètres pouvant être manipulés afin de contrôler l'adhésion et l'étalement cellulaire (notamment la force ionique et la charge de surface), afin de définir comment des cellules vivantes peuvent être maintenues en lévitation à une certaine distance d'une surface par le jeu des propriétés électrostatiques des cellules et des surfaces. La polymérisation de l'actine sur des cellules en lévitation a été aussi étudiée dans ce sous-chapitre.

Deux méthodes sont ensuite analysées pour synchroniser l'adhésion cellulaire: l'augmentation de la concentration du tampon utilisé, par diffusion ionique et l'application d'un pulse électrique. Le volet suivant des résultats concerne la synchronisation de cellules qui se trouvent d'abord en lévitation puis adhérent de manière synchrone par diffusion ionique. Dans ce cas là, le temps de synchronisation obtenu a été trop long par rapport à la période de polymérisation de l'actine. Le dernier sous chapitre des résultats décrit comment la synchronisation a été obtenue avec succès sur un substrat d'ITO en appliquant des pulses électriques très courts (5V pendant 0.1 s). Les conditions expérimentales testées sont récapitulées dans des tableaux et celles qui induisent le plus de cellules adhérentes sont retenues. La synchronisation a été démontrée en étudiant l'activité de polymérisation de l'actine pendant l'étalement d'une population de 14 cellules induit par pulse électrique.

Enfin, une **discussion** des résultats est proposée dans le quatrième chapitre. Les résultats concernant les distances entre cellules et substrat sont estimés par observation en RICM et comparées avec les valeurs obtenues théoriquement à l'aide de modélisations appropriées. Une figure synthétise ces résultats.

En **conclusion,** nous estimons que nous avons obtenu, pour la première fois, la synchronisation de l'étalement cellulaire d'un groupe de cellules grâce à une méthode électrochimique. Ceci pourrait permettre, en faisant une analyse biochimique appropriée, d'identifier les événements moléculaires qui conduisent à l'adhésion cellulaire. Nous estimons que les connaissances acquises au cours de cette étude pourraient également servir de base à d'autres études sur les mécanismes contrôlant l'adhésion cellulaire, soit en servant de modèle d'étude de mutants affectant diverses protéines cellulaires, soit en permettant des analyses plus fines des paramètres biophysiques mis en jeu.

Summary

I. Introduction 1

1.1 *Dictyostelium discoideum*: lifestyle and importance as a model organism to study cell spreading and adhesion mechanisms 1
1.2 Biological parameters that influence cell adhesion and spreading 4
1.2.1 Plasma membrane lipids and proteins: the main source of surface charge 4
1.2.2 *Dictyostelium* adhesion proteins 10
1.2.3 The cell cytoskeletons 12
1.2.4 Formation of microfilaments 15
1.2.5 Actin polymerization leads to cell membrane deformation 19
1.2.6 Morphological structures of *Dictyostelium* actin cytoskeleton 21
1.2.7 Focal adhesion/contact and adhesion sites in *D. discoideum* 24
1.2.8 Dictyostelium spreading 29
1.3 Cell manipulation using electric fields 31
1.3.1 Electroactive substrates to control cell adhesion 31
1.3.2 Influences of electrical field on the cells and cell-size model membrane systems (liposomes) 37
1.3.2.1 Electrotaxis 37
1.3.2.2 Electrical forces (and their effects) for manipulating cells at the microscale 40
1.3.2.3 Cells characterization, separation and handling using EP and DEP 44
1.4 Objectives 49

Chapter II. Materials and methods 51

2.1 Materials 51
2.1.1 Buffers and chemicals 51
2.1.2 *D. discoideum* culture and handling 51
2.1.3 Preparation of surfaces 52
2.1.4 Experimental chambers 52
2.1.5 Electrochemical experiments 53
2.1.6 Mathematical simulation of ion diffusion in the double chamber setup 55
2.1.7 Mathematical simulation of the pH in solution at the conductive surface 56
2.1.8 Optical observation of cell spreading 57
2.1.9 Analysis of cell spreading kinetics 61
2.1.10 Analysis of LimE-GFP fluorescence 61
2.2 Electrical phenomenon at the interface 62
2.2.1 Brief description of the electrical double layer 62
2.2.2 The Gouy-Chapman Theory 64
2.2.3 Tacking into account the finite size of electrolyte ions: the Stern modifications 67
2.2.4 Zeta potential measurements of surfaces 68
2.2.5 Surface charge density and point of zero charge 72
2.2.6 Water electrolysis 74
2.2.7 Electric proprieties of ITO material 75

2.2.8 Interactions between two charged particles: DLVO theory. Applications to the situation: one charged particle and a charged surface 77
2.2.9 Model of cell attachment to charged surfaces as a function of ionic concentration 82

Chapter III Results 84

3.1 Unsynchronized adhesions 84
3.1.1 Dynamics of cell-substrate contact areas during spreading and motility 84
3.1.2 Cyclic actin polymerisation activity during cell adhesion in SB 89
3.1.3 Cells that contact the surface under the action of gravity are not synchronized 92
3.2 Electric field influence on adherent cells 94
3.2.1 Influence of the electric field on the cells deposited on the ITO material 94
3.2.2 Influence of the electric field on the cells deposited on other conductive materials (Ti, Au and Pt) 101
3.3 Control of cellular adhesion by changing buffer concentration, salts nature or by surface chemical treatment 105
3.3.1. Electrostatic repulsion between *D. discoideum* cells and a glass surface 105
3.3.2. Electrostatic attraction between *D. discoideum* cells and a APTES treated glass surface 112
3.3.3. Actin polymerization of *D. discoideum* cells in state of levitation 113
3.4 Synchronization by ion diffusion 115
3.4.1 Electrostatic control of *D. discoideum* adhesion by ionic diffusion 115
3.4.2 Synchronization of *D. discoideum* cells using ionic diffusion 122
3.5 Synchronization by electrical pulse 126
3.5.1 Electrostatic control of *D. discoideum* adhesion by electrochemical means 126
3.5.2 Actin polymerization kinetics in electrochemically induced cell synchronization 134

IV Discussion 139

4.1 Actin polymerization at actin foci: does it require contact with the surface ? 139
4.2 Estimation of the repulsive electrostatic forces and distances between the cells and surfaces as a function on ionic concentrations 142
4.2.1 The effect of ionic concentration on the electrostatic repulsion and attraction 142
4.2.2 Electrostatic repulsive forces estimations 144
4.2.3 Distance calculation 147
4.3 Which has the main contribution to cell attraction when a pulse is applied: the electrophoretic force (EP) or the change of surface charge? 153
4.4 Synchronization of cellular adhesion 157

Perspectives 163

Bibliography 167

I. Introduction

1.1 *Dictyostelium discoideum*: lifestyle and importance as a model organism to study cell spreading and adhesion mechanisms

Dictyostelium discoideum is a soil-living amoeba belonging to the phylum Mycetozoa (Raper, 1935). *D. discoideum*, commonly referred to as slime mold, is a primitive eukaryote that is able to differentiate from unicellular amoebae into a multicellular organism and then into a fruiting body within its lifetime.

In the wild, *D. discoideum* can be found in soil and moist leaf litter. The primary diet of *D. discoideum* consists of bacteria, which are found in the soil and decaying organic matter. The amoebae feed on bacteria by phagocytosis.

When nutrients are available, *Dictyostelium discoideum* lives, divides and grows as single-cell amoebae (with an averaged diameter of 10 µm, if it is considered spherical). This growth phase is called vegetative stage (Fig. 1.1).

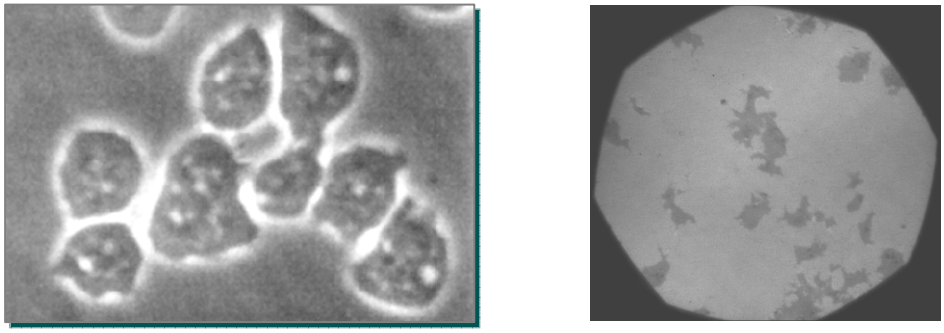

A **B**

Fig. 1.1 A. Phase contrast image and **B.** Reflection Interference Contrast Microscopy image of unicellular amoebae in vegetative stage.

The asexual life cycle of *D. discoideum* begins upon exhaustion of food sources, when vegetative cells aggregate to become multicellular (Aubry, 1999). *D. discoideum* has a multicellular development cycle (social cycle) that consists of four stages: vegetative, aggregation, migration, and culmination. Selected life stages are shown in Fig. 1.2 (Sameshima, 2001).

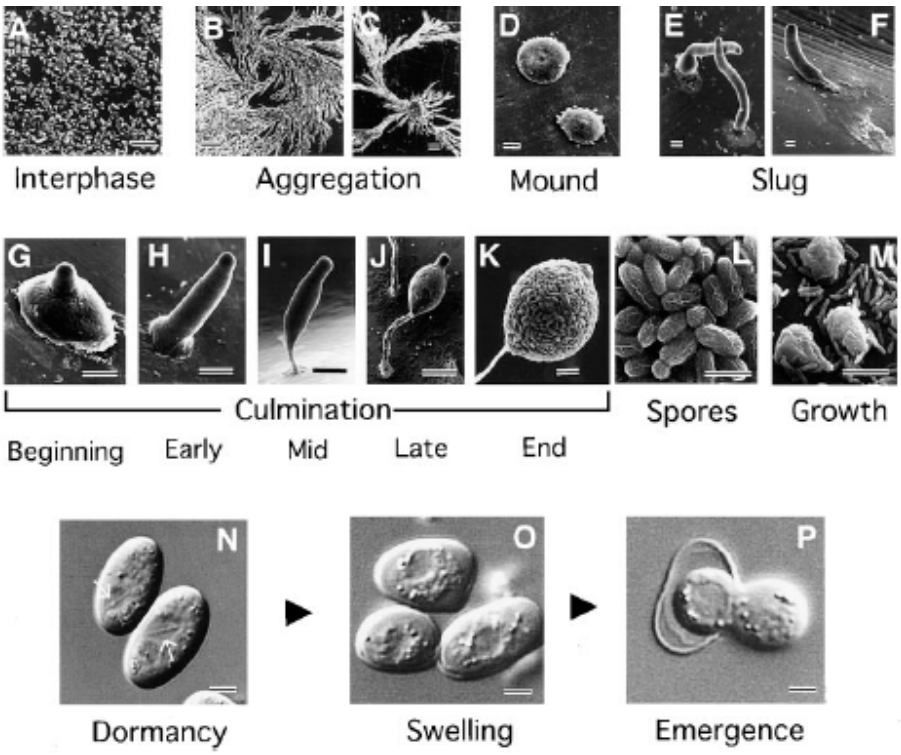

Fig. 1.2 Scanning electron micrographs of the asexual life cycle (A–M) and germination process observed by differential interferential contrast (DIC) (N–P) of *D. discoideum*, strain NC-4. (**A**) Interphase. (**B, C**) Aggregation stage. (**D**) Mound. (**E**) Nascent slug. (**F**) Migrating slug. (**G–K**) Beginning, early, mid, late, and end of culmination stage, respectively. At the end of the culmination stage, fruiting body formation is complete. (**L**) Spores in sorus. A part of **K** was enlarged. (**M**) Amoebae feeding on bacteria. (**N**) Dormant spores. (**O**) Swollen spores. (**P**) Emergence of nascent amoeba. Scale bar, 100 µm (**C**), 50 µm (**A**, **B**, **D–J**), 20 µm (**K**), 10 µm (**L**, **M**), 2 µm (**N–P**) (Sameshima, 2001).

Lab cultivation

D. discoideum's ability to be easily cultivated in the lab (Tyler, 2000) adds to its appeal as a model organism. The isolation of mutants that were able to grow axenically (Watts, 1970) made it possible to grow *Dictyostelium* in liquid nutritive medium without bacteria organisms. Organisms *D. discoideum* can be grown either in shaken liquid culture (e.g., HL5 medium) or on a bacterial lawn in Petri dishes. The cultures grow best at 22^{o}-24^{o}C (room temperature) and generation time is 8-12 hours in HL5 medium and 4-6 hours on a bacterial lawn.

D. discoideum cells can be fed on *E. coli*, which is adequate for starting the life cycle. When the food supply is diminished, the amoebae will aggregate. Soon, the dish will be covered with various stages of the social life cycle or sexual life cycle.

The establishment of a transformation system (Nellen, 1984) paved the way for the genetic manipulation of this organism.

Use as a model organism to study cellular adhesion

During their vegetative stage, *D. discoideum* cells adhere, move, emit and react to chemical signals and are able to differentiate. These processes present characteristics similar to cell migration in invasive cancer. The National Institute of Health (NIH) has been proposing amoeba as an attractive model for cancer research. Its genetic background cycle makes *D. discoideum* a valuable model organism to study genetic, cellular, and biochemical processes in more advanced organisms (see www.nih.gov/science/models/d_discoideum).

It can be observed at organism, cellular, and molecular levels primarily because of the restricted number of cell types, behaviors, and their rapid growth (Tyler, 2000). It is used to study cell differentiation, chemotaxis and programmed cell death, which are all natural cellular processes. It is also used to study common physiological phenomenon including cell sorting, pattern formation, phagocytosis, motility, and signal transduction (www.dictybase.org).

D. discoideum has a haploid genome with about half the number of genes of human beings, which can be manipulated by standard molecular genetic techniques. It carries similar genes and pathways making it a good candidate for gene knockout (Nag, 2008).

The entire genome of *D. discoideum* was sequenced (Eichinger, 2005) and is accessible in a public database called *dictyBase* (www.dictybase.org). Individual cell behavior accounts for many phases of health and disease. This is portrayed in *D. discoideum* in many different ways. Cytokinesis acts as part of immune response, tissue maintenance, and cancer, in the form of cell proliferation. Chemotaxis is involved in inflammation, arthritis, asthma, lymphocyte trafficking, and axon guidance. Phagocytosis is used in immune surveillance and necessary for antigen presentation, while cell-type determination, cell sorting, and pattern formation are basic features of embryogenesis.

D. discoideum is therefore a good model organism to study general cell biology problems such as the coupling between plasma membrane adhesion and the cytoskeleton or cell polarization during explorative motility.

1.2 Biological parameters that influence cell adhesion and spreading

Dictyostelium discoideum cells adher directly (no extra cellular matrix necessary) on different surfaces, hydrophilic or hydrophobic ones that exhibit different atomic or molecular structures at the interface with a liquid medium. Thus, we are strongly interested in cell surface charge, since plasma membrane lipids and proteins carry net charges, and how this aspect could influence cell adhesion. In addition, we are interested in mechanisms of cellular adhesion (adhesion proteins, distance interactions between cell membrane and surface molecules, signaling pathways).

1.2.1 Plasma membrane lipids and proteins: the main source of surface charge

An eukaryote is an organism whose cells contain complex structures enclosed within membranes. Many living organisms, including all animals, plants, fungi, etc. are eukaryotes. The defining membrane-bound structure that differentiates eukaryotic cells from prokaryotic cells is the nucleus, which gives these organisms their name. They have a variety of internal membranes and structures, called organelles, and a cytoskeleton composed of microtubules, microfilaments, and intermediate filaments, which play an important role in defining the cell's organization and shape. Eukaryotic DNA consists of several linear DNA molecules associated to specific proteins (histones), called chromosomes. During cell division a microtubules spindle assemble that helps to separate the chromosomes.

Given that in our present study, we used solutions very different from the usual culture medium (very low ionic strength, extreme pH values) and we applied electrical pulses in solutions containing cells, we are interested in electrical and chemical properties of the cell membrane determinated by its composition and architecture. In figure 1.3 we offer a simple illustration of an eukaryotic plasma membrane.

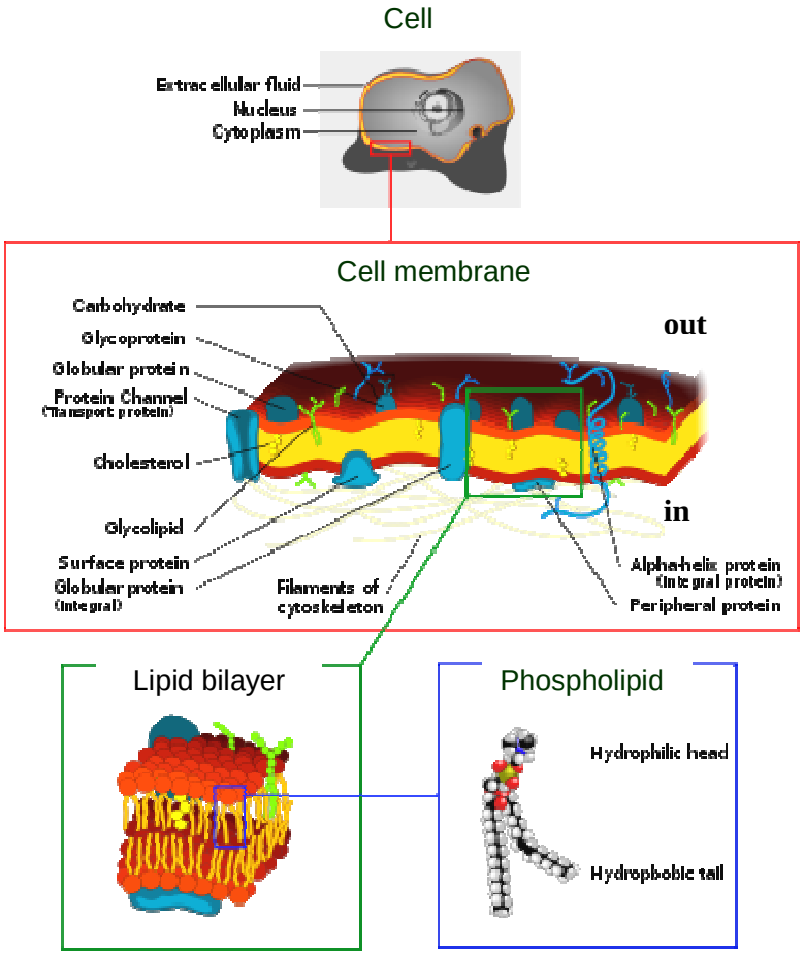

Fig. 1.3 Schematic representations of a eukaryotic cell membrane and some components (Alberts, 2008)

Despite their differing functions, all biological membranes have a common general structure: they are made of a very thin film of lipids and proteins held together by hydrophobic interactions. It is a continuous double layer approximately 5 nm thick, and in many membranes the two layers have a different composition. Lipid molecules constitute about 50% of the mass of most animal cell membranes, nearly all of the remainder being proteins. There are about 10^9 lipid molecules in the plasma membrane of a small animal cell (10 µm in diameter) and about 50 lipid molecules for each protein molecule in the cell membrane (lipid molecules are small compared with protein molecules) (Alberts, 2008).

Cell membranes are dynamic, fluid structures, intrinsically impermeable for most water-soluble molecules, and most of their molecules move about in the plane of the membrane. This basic fluid structure of the membrane is provided by the lipid bilayer.

The amount of each lipid depends upon the cell type (Lodish, 2004). The most abundant membrane lipids are phospholipids (phosphoglycerides, sphingolipids, see Fig. 1. 4), cholesterol and glycolipids (galactocerebroside and ganglioside that always contain one or more negatively charged sialic acid residues).

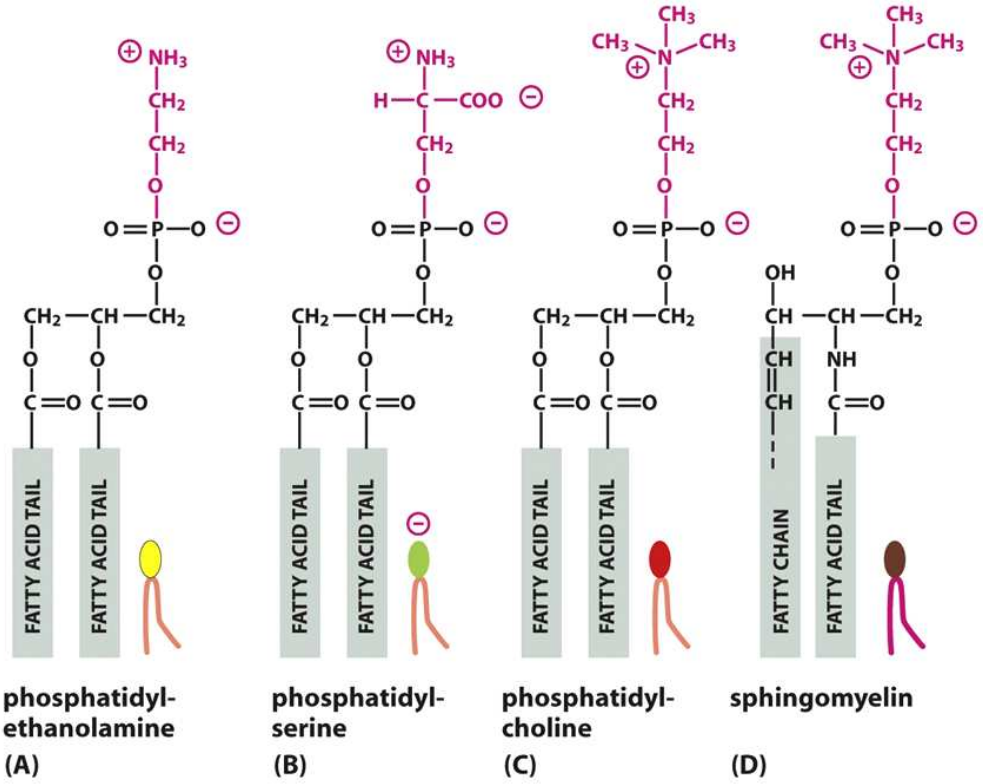

Fig 1.4 Four major phospholipids of the mammalian plasma membrane. The lipid molecules shown in **A**-**C** are phosphoglycerides, which are derived from glycerol. The molecule in **D** is sphingomyelin, which is derived from sphingosine and is therefore a sphingolipid. Note that only phosphatidylserine carries a net negative charge, the other three are electrically neutral at physiological pH, carrying one positive and one negative charge (Alberts, 2008).

Table 1.1 compares the lipid composition of several biological membranes.

Table 1.1 Appoximate lipid composition of different cell membranes

LIPID	PERCENTAGE OF TOTAL LIPID BY WEIGHT					
	LIVER CELL PLASMA MEMBRANE	RED BLOOD CELL PLASMA MEMBRANE	MYELIN	MITOCHONDRION (INNER AND OUTER MEMBRANES)	ENDOPLASMIC RETICULUM	*E. COLI* BACTERIUM
Cholesterol	17	23	22	3	6	0
Phosphatidylethanolamine	7	18	15	28	17	70
Phosphatidylserine	4	7	9	2	5	trace
Phosphatidylcholine	24	17	10	44	40	0
Sphingomyelin	19	18	8	0	5	0
Glycolipids	7	3	28	trace	trace	0
Others	22	13	8	23	27	30

Protein molecules that span the lipid bilayer (transmembrane proteins) mediate nearly all of the other functions of the membrane, transporting specific molecules across it, for example, or catalyzing membrane-associated reactions such as ATP synthesis (Curran, 2003). In the plasma membrane, some transmembrane proteins serve as structural links that connect the cytoskeleton through the lipid bilayer to the extracellular matrix (if it exists), a solid substrate or an adjacent cell (cell-cell adhesion), while others serve as receptors to detect and transduce chemical signals in the cell's environment (Sheetz, 2001).

Many membrane proteins are glycosylated (Lodish, 2004). These carbohydrates appear as oligosaccharide chains (fewer than 15 sugars) covalently bound to membrane proteins (glycoproteins). Another group, proteoglycans, which consist of long polysaccharide chains linked covalently to a protein core, is found mainly outside the cell, as part of the extracellular matrix. In the vegetative stage of *Dictyostelium discoideum,* the extracelullar matrix is missing (Traynor, 1992).

The membrane is selectively permeable and able to regulate what enters and exits the cell, thus facilitating the transport of materials needed for survival (electrically-neutral and small molecules pass the membrane easier than charged or large ones). There are two classes of membrane transport proteins: transporters and channels. Both form continuous protein pathways across the lipid bilayer. Whereas transmembrane movement mediated by transporters can be either active (pumps, using ATP hydrolysis, for example, see fig. 1.5) or passive (spontaneous), solute flow through channel protein is always passive (Gouaux, 2005).

The membrane also maintains the cell membrane potential, with the inside usually negative with respect to the outside. A membrane potential arises when there is a difference in the electrical charges on the two sides of a membrane. Such charge differences can result from active electrogenic pumping (see fig. 1.5) and from passive ion diffusion through ion protein channels.

The concentration gradient and the potential difference across the membrane (membrane potential) combine to form a net driving force, the electrochemical gradient, for each charged solute (Alberts, 2008). The electrochemical gradient influences the charged solute transport through the ion protein channels.

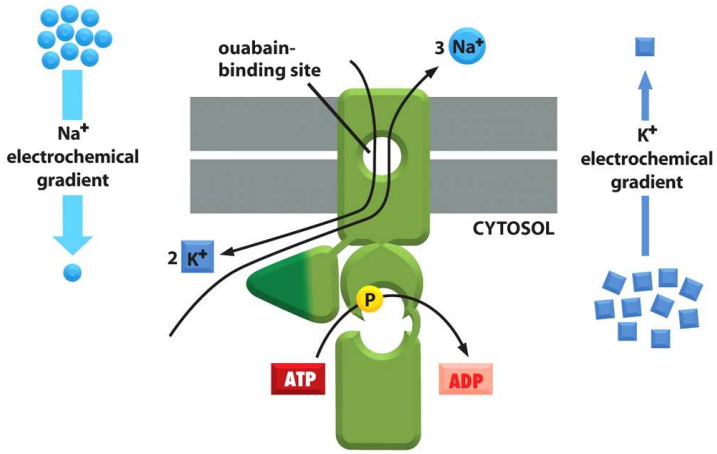

Fig. 1.5 The Na^+-K^+ pump. This transporter actively pumps Na^+ out and K^+ into a cell against their electrochemical gradient. For every molecule of ATP hydrolyzed inside the cell, three Na^+ are pumped out and two K^+ are pumped in (Alberts, 2008).

However, the electrogenic effect of the pumps, contributes only for approximately 10% to the membrane potential. The rest is attributed to the function of ion channels (narrow protein pores) that allow specific inorganic ions, primarily K^+, Na^+, Ca^{2+}, or Cl^-, to diffuse rapidly, with a rate of 100 million ions each second, down their electrochemical gradients across the lipid bilayer (Millhauser, 1988). In particular, nerve cells (neurons) have made a speciality of using ion channels to receive, conduct and transmit signals.

Only a small number of ions must move across the plasma membrane to set up the membrane potential (Fig. 1.6), which varies for an animal cell between 20 and 120 mV, depending on the organism and cell type. Thus, the membrane potential arises from movements of charges that leave ion concentrations practically unaffected and result in only a very slight discrepancy in the number of positive and negative ions on the two

sides of the membrane (fig. 1.6, Alberts, 2008). Knowing that the membrane capacitance for most animal cells is 1 $\mu F/cm^2$ one deduces that the movements of 173.000 K^+ ions across 300 μm^2 of membrane (surface of a spherical cell with diameter of 10 µm) which represent 1 positive charge per 180 nm^2, will carry sufficient charge to shift the membrane potential by about 100 mV. Moreover, these movements of charge are generally rapid, taking only a few milliseconds or less.

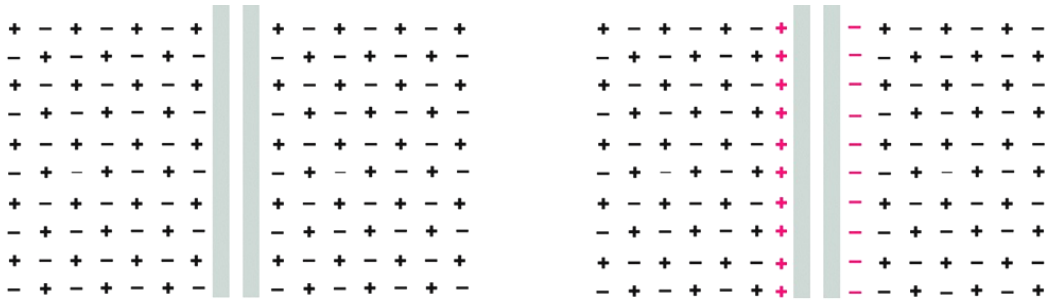

Fig. 1.6 The ionic basis of a membrane potential. A small flow of ions carries sufficient charge to cause a large change in the membrane potential

Although the K^+ gradient always has a major influence on this potential, the gradients of other ions (and the disequilibrating effects of ion pumps) also have a significant effect: the more permeable the membrane for a given ion, the more strongly the membrane potential tends to be driven toward the equilibrium value for that ion (Jacquez, 1971). Consequently, changes in a membrane's permeability to ions can cause significant changes in the membrane potential according to the Goldman equation (Goldman, 1943). This is one of the key principles relating the electrical excitability of cells to the activities of ion channels.

Mainly due to the presence of phosphatidylserine, ganglioside glycolipid and transmembrane proteins charges, but also to all hydroxyl groups in transmembrane glycoproteins, glycolipids, sphingomyelin, phosphatidylinositol, cholesterol, etc., the surface charge of an eukaryotic cell membrane is supposed to be negative in physiological conditions (pH~6-7) (Lakshminarayanaiah, 1975). Moreover, the membrane potential may influence the surface charge, especially when the extracellular

medium is lacking the inorganic ions. For example, the K^+ ions that go to form the layer of charge at the external side of the membrane, although their number is not significant, reduce the negative charges of the bilayer constituents.

A theoretical estimation of cell surface charge is very difficult to make and it widely differs in function of the cell type, including also here the influence of the membrane potential. Considering only phosphatidylserine and ganglioside glycolipid carrying negative charges, and additionaly supposing a symmetrical distribution in the two lipid layers of the membrane, we could estimate, on average, a minimum charge density of 1 negative elementary charge per 40 nm^2. For example, experimentally, the average values of the effective charge density present on the giant axon of the squid, frog muscle and barnacle muscle in their normal ionic environment, correspond to 1 negative charge per 2.22, 1.03 and 1.95 nm^2 respectively of the membrane area (Lakshminarayanaiah, 1975).

1.2.2 *Dictyostelium* adhesion proteins

There is less known about cell-substrate adhesion, the proteins involved and how motion and adhesive forces work together in *Dictyostelium* cells than in mammalian cells. Cell-substrate adhesion is a major aspect of amoeboid movement in the social amoeba *Dictyostelium* as well as certain mammalian blood and tumor cells. Cell-substrate adhesion is a crucial step in many biological processes such as development, wound healing, metastasis and phagocytosis (Fey, 2002). In mammalian cells, several proteins are involved in cellular adhesion, in particular cell-surface receptors, signaling molecules and components of the actin cytoskeleton. Integrin-mediated cell adhesion is one of the most widely studied adhesion mechanism. Integrins are heterodimeric type I transmembrane proteins composed of one α-subunit and one β-subunit, which bind to the extracelullar matrix by their extracellular domain and control cell spreading, migration, proliferation and survival (Schwartz, 2001).

In *Dictyostelium*, several proteins (glycoproteins) that mediate cell-cell adhesion during specific stages of development have been identified (e.g., gp 150, gp 130, gp 80, gp 24). Gp 24 protein (DdCAD-1) is a small, secreted but membrane anchored glycoprotein with similarities to vertebrate cadherins, expressed in the initial stages of

development (Brar, 1993). To date, it seems that only one of these molecules (glycoprotein gp 130) has been directly implicated in binding to substrate (Chia, 1996). It also plays role in phagocytosis.

To identify the molecular mechanisms involved in phagocytosis, Cornillon and colab. generated random insertion mutants of *Dictyostelium discoideum* and selected two mutants (phg1-1 and phg1-2) defective for phagocytosis (Cornillon, 2000). Both were characterized by insertions in the same gene, named *PHG1*. This gene encodes a polytopic membrane protein with an N-terminal luminal domain and nine potential transmembrane segments. Homologous genes can be identified in many species. Disruption of *PHG1* caused a selective defect in phagocytosis of latex beads and *Escherichia coli*, but not *Klebsiella aerogenes* bacteria. This defect in phagocytosis was caused by a decrease in the adhesion of mutant cells to phagocytosed particles. These results indicate that the Phg1 protein is involved in the adhesion of *Dictyostelium* to various substrates, a crucial event of phagocytosis.

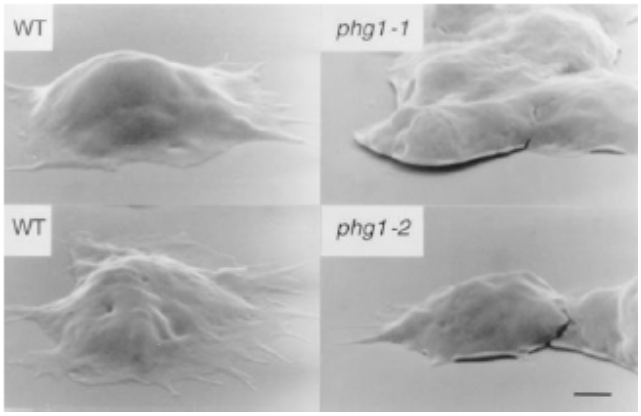

Fig. 1.7 Adhesion of wild-type (WT) and phg1 mutant cells to their substrate. Cells were grown on sterile glass plates for 3 days, fixed, dehydrated, and coated with gold. They were visualized in a scanning electron microscope. Scale bar = 1 µm (Cornillon, 2000).

Upon more prolonged culture in HL5 medium, phg1 mutant cells did adhere to their substrate. However, examination of the cells by scanning electron microscopy revealed distinct differences between adherent wild-type and mutant cells. Whereas wild-type cells adhered tightly to the glass coverslip, phg1 cells did not spread as extensively and local detachment zones could be seen (Fig. 1. 7).

In 2002 Fey reported the finding of a novel adhesion receptor, a protein named SadA localized to the cell surface, with nine putative transmembrane domains and three conserved EGF-like repeats in a predicted extracellular domain (Fey, 2002). Cornillon et al. identified in 2006 a new adhesion molecule in *Dictyostelium.* The SibA protein, (Cornillon, 2008), is a type I transmembrane protein, and its cytosolic, transmembrane and extracellular domains contain features also found in integrin β chains. Genetic inactivation of SibA affects adhesion to phagocytic particles, as well as cell adhesion and spreading on its substrate but it does not visibly alter the organization of the actin cytoskeleton, cellular migration or multicellular development. Still, no homologues of α-integrins were found in the *Dictyostelium* genome.

Table 1.2 The adhesion proteins found in *Dictyostelium*:

Protein	*Higher Eukaryote homologs*
Glycoprotein gp 130	Vertebrate cadherins
Phg1 transmembrane protein	9TM-αH protein
SadA transmembrane protein	9TM-αH protein
Sib(A-E) transmembrane proteins	β integrin homologue (5 isoforms)

1.2.3 The cell Cytoskeletons

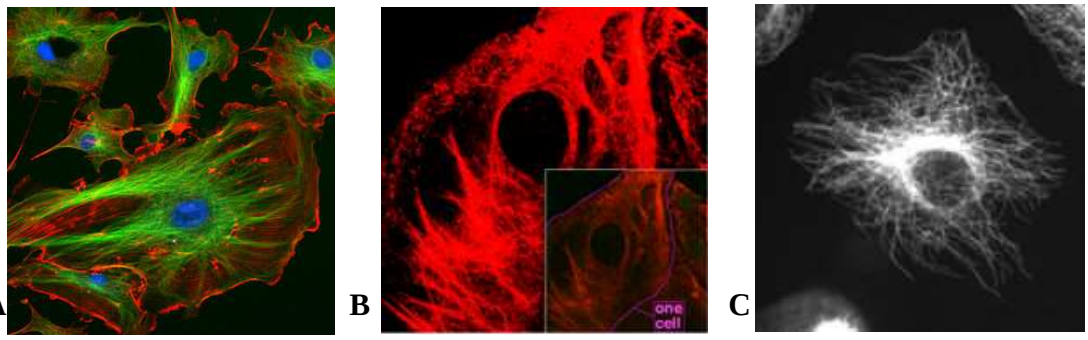

Fig 1.8 The eukaryotic cytoskeleton. **A.** Actin filaments are shown in red, microtubules in green, and the nuclei are in blue. **B.** Microscopy of keratin filaments inside cells. **C.** Microtubules in a fixed cell.

The cytoskeleton is found underlying the cell membrane in the cytoplasm and provides scaffolding for membrane proteins to anchor to (see Fig. 1.8). It exerts mechanical forces that deform the plasma membrane and form protrusions that extend from the cell. Indeed, cytoskeletal elements interact extensively and intimately with the

cell membrane (Doherty, 2008). The cytoskeleton is able to form appendage-like organelles, such as cilia, which are microtubule-based extensions covered by the cell membrane, and filopodia, which are actin-based extensions involved in stabilizing pseudopodia on the substratum (Heid, 2005). These extensions are closed in membrane and project from the surface of the cell in order to sense the external environment and/or make contact with the substrate or other cells. The concept and the term (*cytosquelette*, in French) was first introduced by French embryologist Paul Wintrebert in 1931.

Eukaryotic cells contain three main kinds of cytoskeletal filaments, which are microtubules, intermediate filaments, and microfilaments.

Microtubules

Microtubules are hollow cylinders about 23 nm in diameter (lumen = approximately 15 nm in diameter), most commonly made of 13 protofilaments which, themselves are polymers of alpha and beta tubulin. They are commonly organized by the centrosome and they have a very dynamic behaviour, binding GTP for polymerization: in the cell, the “minus” end is bound to the centrosome and therefore stable most of the time. Tubulin GTP binds to the “plus” end and hydrolysis the GTP into GDP. The microtubule alternates between slowly elongation and rapidly disaggregating phases. The growth phase lasts as long as a “cap” of tubulin GTP is present at the “plus” end.

In several cell types, an intriguing correlation exists between the position of the centrosome and the direction of cell movement: the centrosome is located behind the leading edge, suggesting that it serves as a steering device for directional movement (Ueda, 1997). In *Dictyostelium*, however Ueda et al. demonstrated that the extension of a new pseudopod in a migrating cell precedes centrosome repositioning. The microfilament network therefore dictates the positioning of the microtubules network.

Microtubules play key roles in:

- intracellular transport (associated with dyneins and kinesins, they transport organelles like mitochondria or vesicles).
- the axoneme of cilia and flagella.
- the mitotic spindle.
- synthesis of the cell wall (in plants).

Intermediate filaments

These filaments, around 10 nm in diameter, are more stable (strongly bound, two anti-parallel helices, forming tetramers) than actin filaments. Like actin filaments, they function in the maintenance of cell-shape by bearing tension (microtubules, by contrast, resist compression. It may be useful to think of micro- and intermediate filaments as cables and of microtubules as cellular support beams). Intermediate filaments organize the internal tridimensional structure of the cell, anchoring organelles and serving as structural components of the nuclear lamina and sarcomeres (Blumenthal, 2004). They also participate in some cell-cell and cell-matrix junctions. Different intermediate filaments are:

- made of vimentins, being the common structural support of many cells.
- made of keratin, found in skin cells, hair and nails.
- neurofilaments of neural cells.
- made of lamin, giving structural support to the nuclear envelope.

In *D. Dictyostelium* there are no intermediate filaments.

Actin filaments / Microfilaments

Around 6 nm in diameter, this filament type is composed of two intertwined actin chains (double helix structure) (Bamburg, 1999). Microfilaments are most concentrated just beneath the cell membrane, and are responsible for resisting tension and maintaining cellular shape, forming cytoplasmic protuberances (pseudopodia, filopodia, lamelipodia and microvilli- although these by different mechanisms). They are involved in phagocytosis and in some cell-to-cell or cell-to-matrix associations. They are also important for cytokinesis (formation of the cleavage furrow, specifically for cell division in suspension, (Neujahr, 1997, Zang, 1997)) and, along with myosin, for muscular contraction. Actin/Myosin interactions also help produce cytoplasmic streaming in most cells (Eichinger, 1999).

We are interested in the actin protein because its polymerization drives cell spreading and movement. Microfilaments are very dynamic structures: actin monomer polymerize and depolymerize leading to plasma membrane deformation.

1.2.4 Formation of microfilaments

Actin is one of the most highly conserved protein throughout evolution, being that it interacts with a large number of other proteins. It has 80.2% sequence conservation at the gene level between *Homo sapiens* and *Saccharomyces cerevisiae* (a species of yeast), and 95% conservation of the primary structure of the protein product. It is found in all eukaryotic cells where it may be present at concentrations between 10 and 200 µM. In *Dictyostelium* its plasma concentration as intermediate, is 100 µM (Podolski, 1990).

The actin monomer, known as globular actin (G-actin, 375 amino acids, 42 kDa), consists of two domains which can be further subdivided into two subdomains. ATP or ADP is located in the cleft between the domains with a calcium ion bound (Kabsch, 1990) (Fig 1.9A, black arrow). G-actin subunits assemble into long filamentous polymers called F-actin. Two parallel F-actin strands must rotate 166 degrees in order for them to layer correctly on top of each other (Fig. 1.9B). This gives the appearance of a double helix and, more importantly, gives rise to microfilaments of the cytoskeleton (Eichinger, 1999). Microfilaments measure approximately 7 nm in diameter with a loop of the helix repeating every 37 nm (Bamburg, 1999).

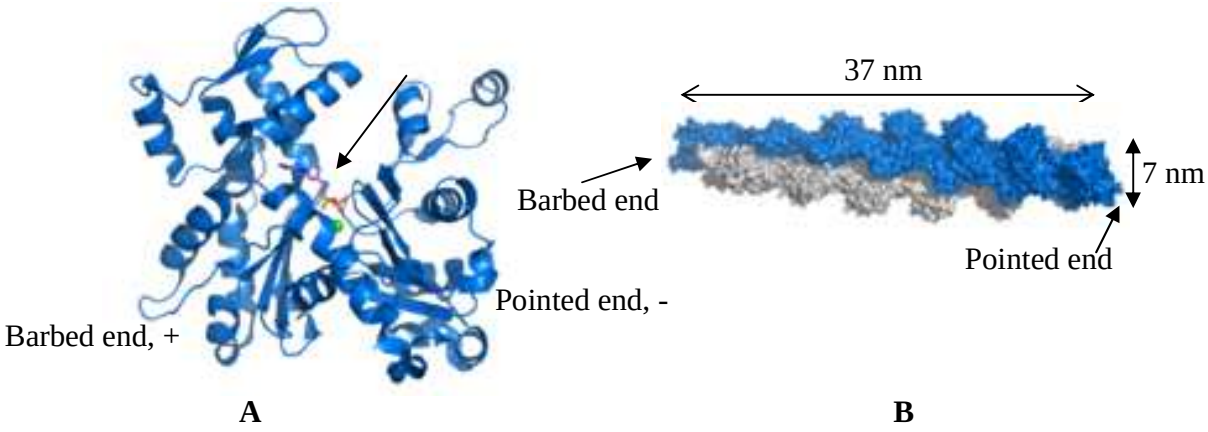

Fig. 1.9 A. Ribbon model of asymetric G-Actin molecule, ATP and the divalent cation are pointed by the black arrow; **B.** F-Actin; surface representation of 13 subunit repeat.

The actin molecule is polarized due to its structural asymmetry. Consequently, upon actin polymerization, every filament exposes its two extremities different protein domains that have different properties. The two extremities are called barbed end (+) and pointed end (-) (Fig. 1.9).

The polymerization of protein can be considered like a bimolecular reaction, where a monomer in solution binds to the extremity of a filament containing *n* actin subunits to form a new filament with *n+1* monomers of G-actins (Fig. 1.10A). Also, the rate constants, k_{on} and k_{off} respectively, are not the same at the two extremities of the filament: at the barbed end, the association and disassociation constants are higher than at the pointed end ($k_{on+} > k_{on-}$ and $k_{off+} > k_{off-}$ respectively; Fig. 1.10B), mainly due to the difference in electrostatic interactions at the filament extremities (Sept, 1999).

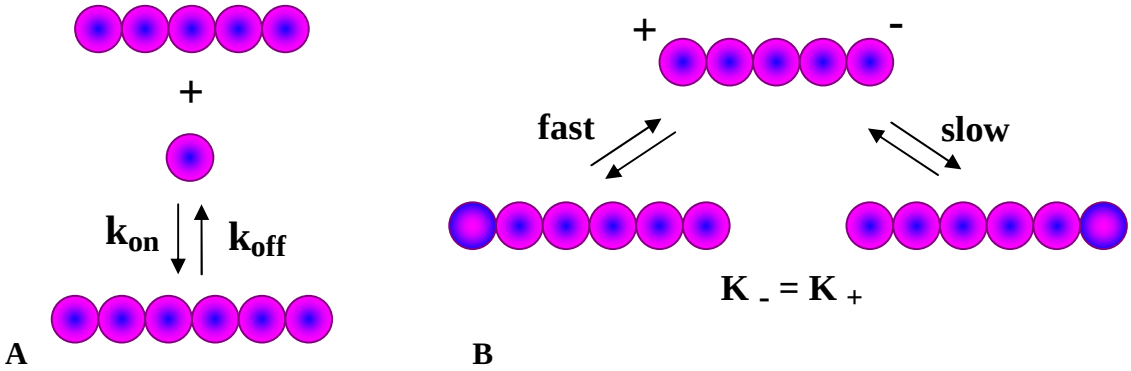

Fig. 1.10 A. Scheme of actin polymerization: k_{on} stands for association constant ($\mu M^{-1} \cdot s^{-1}$) and k_{off} represents the dissociation constant (s^{-1}) **B**. the rate constants (k_{on+}, k_{off+} and k_{on-}, k_{off-} respectively) are different at the two ends of filament: fast kinetics, at the barbed end (+) and slow kinetics, at the pointed end (-).

The general chemical reaction equation can be written as:

$$A_n + A_1 \underset{k_{off}}{\overset{k_{on}}{\Leftrightarrow}} A_{n+1} \qquad \text{Eq. 1.1}$$

where A_1 represents the actin monomer and A_n, A_{n+1} are the filaments with *n* and *n+1* monomers respectively.

The rate of polymer formation is given by:

$$\frac{d[A_{n+1}]}{dt} = \frac{d[A_1]}{dt} = k_{on+} \cdot [A_n][A_1] - k_{off+} \cdot [A_{n+1}] \qquad \text{Eq. 1.2}$$

for the barbed end, and by:

$$\frac{d[A_{n+1}]}{dt} = \frac{d[A_1]}{dt} = k_{on-} \cdot [A_n][A_1] - k_{off-} \cdot [A_{n+1}] \qquad \text{Eq. 1.3}$$

for the pointed end.

At the chemical equilibrium, $\frac{d[A_{n+1}]_{eq}}{dt} = 0$, which implies that:

$$K_+ = \frac{k_{on+}}{k_{off+}} = \frac{[A_{n+1}]_{eq}}{[A_n]_{eq}[A_1]_{eq}} \text{ and } K_- = \frac{k_{on-}}{k_{off-}} = \frac{[A_{n+1}]_{eq}}{[A_n]_{eq}[A_1]_{eq}} \quad \text{Eq. 1.4}$$

It can be noticed that the concentrations ratios from Eq. 1.4 are equal, resulting in the equality of the equilibrium constants ($K_+ = K_-$).

Moreover, in a polymerization reaction, for $n \geq 3$ (up to the nucleation phase), the number of free extremities is approximately the same at any moment (the gain of an extremity site is made on the base on the loss of other one, having also the same kinetics characteristics). Thus, we can appreciate that:

$$[A_n] = [A_{n+1}] = c \quad \text{Eq. 1.5}$$

It results immediately that the rate of polymerization, *r*, becomes:

$$r = \frac{d[A_{n+1}]}{dt} = k_{on} c \cdot [A_1] - k_{off} c = k'_{on} \cdot [A_1] - k'_{off} \quad \text{Eq 1.6}$$

We can find now the actin concentration for which the chemical equilibrium is reached (r = 0):

$$[A_1]_{eq} = \frac{k'_{off}}{k'_{on}} = \frac{k_{off}}{k_{on}} = \frac{1}{K} \quad \text{Eq 1.7}$$

This concentration is called “critical concentration” (C_c). Above this concentration, the filaments (at the barbed or pointed extremities) start to extend and below this concentration, the filaments decrease in length.

The critical concentration varies if the actin monomer is bound to ATP or ADP: 0.12 µM and 2µM respectively. When the monomer concentration lies between these two critical concentrations, net assembly occurs at the barbed end and net disassembly occurs at the pointed end, a process called treadmilling (see fig. 1.11). Thus, at steady state, the barbed end is the favoured site for ATP–actin addition whereas the pointed end is the favoured site for ADP–actin loss, both in vitro and in cells. In cells, actin turnover is enhanced more than 100-fold by actin-binding proteins that sever filaments, enhance subunit disassembly from the pointed end and facilitate ATP-for-ADP nucleotide exchange on free actin subunits (Pollard, 2003).

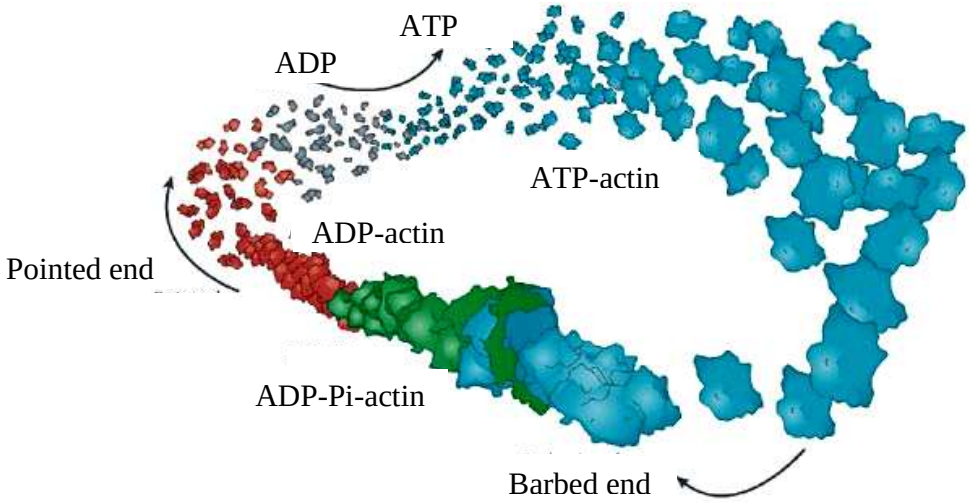

Fig. 1.11 Actin treadmilling model (Chi Pak, 2008)

ATP–actin complexes are preferentially added to the barbed end of actin filaments. Shortly after subunit incorporation, the non-covalently bound ATP is hydrolysed into ADP–P_i; subsequent release of the P_i occurs much more slowly. ATP hydrolysis occurs on average ~1–2 seconds after incorporation, whereas, in purified actin, P_i release occurs on average ~10 minutes after hydrolysis; however, both processes actually occur stochastically for each subunit. Thus, even when the monomer pool consists only of ATP–actin complexes and is given a sufficient amount of time, an actin filament can eventually consist of three types of actin–nucleotide complex: ATP–actin, ADP–P_i–actin and ADP–actin (Chi Pak, 2008).

Actin filament formation can be observed with the help of fluorescent actin monomers. Actin was directly labeled with a fluorescent dye (tetramethylrhodamine-5-maleimide) and was visualized by total internal reflection fluorescence microscopy (Fig. 1.12) (Fujiwara, 2002).

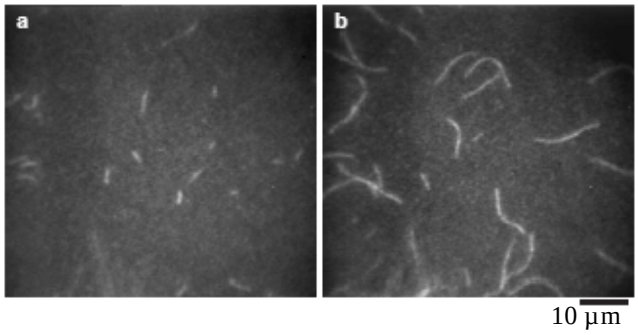

Fig. 1.12 Fluorescence micrographs of actin(Ca) polymerization taken 6 min (**a**) and 34 min (**b**) after the addition of 30 mM potassium chloride, 2 mM magnesium chloride, 4 mM ATP, 20 mM MOPS at pH 7.0, 10 mM DTT. (Fujiwara, 2002)

1.2.5 Actin polymerization leads to cell membrane deformation

The *Dictyostelium* cell is capable to reorganize its cytoskeleton in a few seconds (Eichinger, 1999, Condeelis, 1993). Thus, in vivo, there are regulation systems of actin polymerization. Indeed, actin forms molecular assemblies by interacting with many proteins, in both forms, G-actin and F-actin. These assemblies command cell adhesion, spreading, migration and motility, by providing an efficient pushing force against the plasma membrane. Different stages and their respective proteins are shown in Fig. 1.13.

Signaling pathways converging on WASp/Scar proteins regulate the activity of Arp2/3 complex, which mediates the initiation of new filaments as branches on preexisting filaments (Schafer, 1998; Bretschneider, 2002; Carlier, 2003a; Diez, 2005) (Fig. 1.13; see also Fig. 1.16).

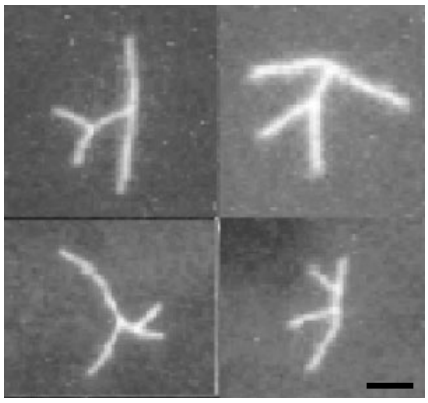

Fig.1.13 Gallery of branched actin filaments polymerized in the presence of N-WASP and Arp2/3 complex. Actin (4 mM) was polymerized in the presence of 100 nM N-WASP and 30 nM Arp2/3 complex. Filaments were polymerized for 3 minutes, then supplemented with 3 mM rhodaminelabeled phalloidin, diluted 500-fold and observed using a fluorescence microscope. Scale bar 5 µm (Carlier, 2003a).

After a brief spurt of growth, the capping protein terminates the elongation of the filaments, this being in favour of a more dense actin cytoskeleton and allows to exert more important forces against the plasma membrane (Eddy, 1996). After filaments have matured by hydrolysis of their bound ATP and dissociation of the γ phosphate, ADF/cofilin proteins promote debranching and depolymerization (Theriot, 1997). Profilin catalyzes the exchange of ADP for ATP, refilling the pool of ATP actin monomers bound to profilin, ready for elongation (Fig. 1.14, Pollard, 2003).

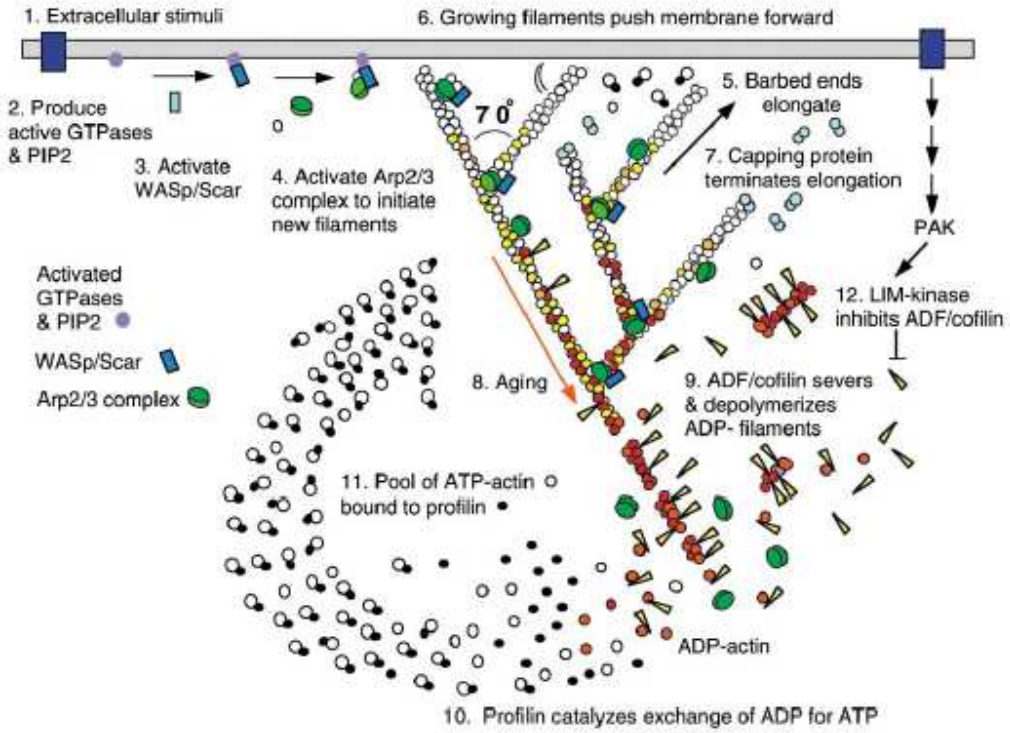

Fig.1.14 Dendritic Nucleation/Array Treadmilling Model for Protrusion of the Leading Edge (1) Extracellular signals activate receptors. (2) The associated signal transduction pathways produce active Rho-family GTPases and PIP2 that (3) activate WASp/Scar proteins. (4) WASp/Scar proteins bring together Arp2/3 complex and an actin monomer on the side of a preexisting filament to form a branch. (5) Rapid growth at the barbed end of the new branch (6) pushes the membrane forward. (7) Capping protein terminates growth within a second or two. (8) Filaments age by hydrolysis of ATP bound to each actin subunit (white subunits turn yellow) followed by dissociation of the _ phosphate (subunits turn red). (9) ADF/cofilin promotes phosphate dissociation, severs ADP-actin filaments and promotes dissociation of ADP-actin from filament ends. (10) Profilin catalyzes the exchange of ADP for ATP (turning the subunits white), returning subunits to (11) the pool of ATP-actin bound to profilin, ready to elongate barbed ends as they become available. (12) Rho-family GTPases also activate PAK and LIM kinase, which phosphorylates ADF/cofilin (Pollard, 2003).

Motile cells extend a leading edge by assembling a branched network of actin filaments that produces physical forces as polymers grow beneath the plasma membrane. A core set of proteins including actin, Arp2/3 complex, profilin, capping protein, and ADF/cofilin can reconstitute the process in vitro, pushing the micrometric beads (Fig. 1.15, Carlier, 2003a). Mathematical models of the constituent reactions predict the rate of motion (Dikinson, 2002).

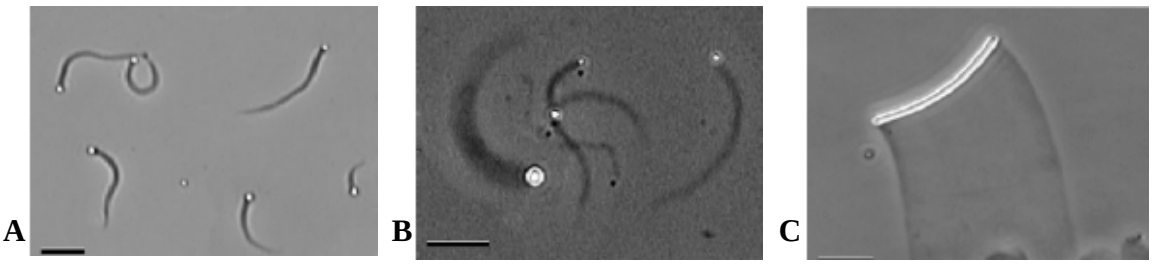

Fig. 1.15 Biomimetic motility assay: Examples of actin-based motility of functionalized particles in the reconstituted motility medium. **A.** N-WASP-coated beads (2 µm in diameter) generate actin tails and undergo propulsion in the medium. **B.** Beads of three different diameters (3, 1, and 0.5 µm) move at the same rate in the medium but display actin tails of different thickness. **C.** A glass rod (1 µm diameter, 30 µm in length) generates a lamellar actin array and moves mimicking lamellipodium extension (Carlier, 2003a).

Marcy et al. (Marcy, 2004) developed a micromanipulation experiment, in which a comet growing from a coated polystyrene bead is held by a micropipette while the bead is attached to a force probe. By pulling the actin tail away from the bead at high speed, they measured the force necessary to detach the tail from the bead (0.25 $nN/\mu m^2$). In addition, many authors present different experimental and theoretical methods for quantification of traction forces exerted by different types of migrating single cells, finding values between 0.1 $nN/\mu m^2$ (for Dictyostelium) and 5.5 $nN/\mu m^2$ (for fibroblastes) (Fukui, 2000; Balaban, 2001; Barentin, 2006).

1.2.6 Morphological structures of *Dictyostelium* actin cytoskeleton

Dynamic actin networks generate forces for numerous types of movements such as lamellipodia protrusion, filopodia protrusion (Fig. 1.16), pseudopod protrusion, uropodia, or the motion of endocytic vesicles (Marcy, 2004). These mechanisms require the barbed ends of actin filaments to be held close to the surface being pushed (Borisy, 2000). These filaments differ in shape, size and functionality.

Pseudopodia are temporary three-dimensional structural projections of eukaryotic cells. Pseudopodia extend by the reversible assembly of actin subunits into microfilaments. The pseudopodium extends until the actin reassembles itself into a network. This is the mechanism by which amoebae moves, as well as some animal cells, such as white blood cells.

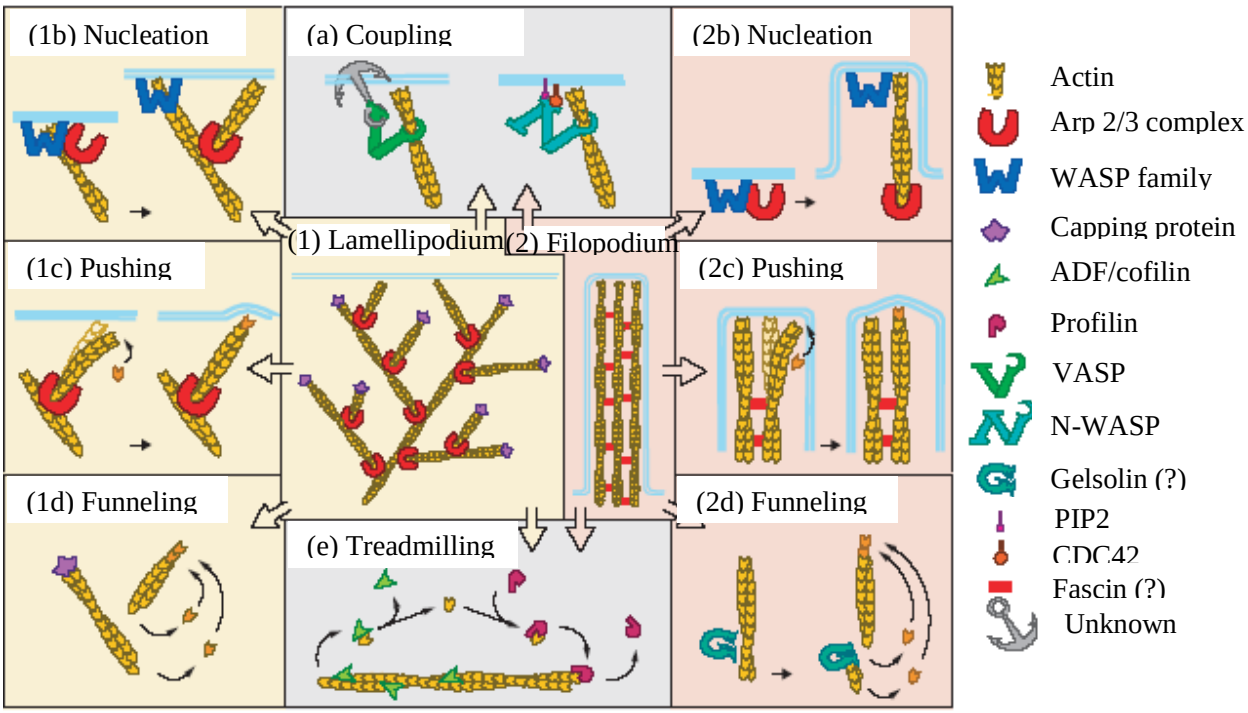

Fig. 1.16 Functional steps for the two major protrusive structures of crawling cells, lamellipodia (1) and filopodia (2). (a) VASP is involved in coupling the actin filament and the membrane, through an as yet unidentified molecule. An additional coupling pathway is provided by N-WASP, which binds PIP2 and is triggered by Cdc42. Members of the WASP family activate the Arp2/3 complex and nucleate formation of actin filaments on pre-existing filaments. **(1b)** In lamellipodia, activation and nucleation are repeated to generate a dendritic array of filaments; **(2b)** in filopodia, activation and nucleation need only occur once. Actin filaments are thought to push against the surface by an elastic Brownian ratchet mechanism **(1c, 2c)**. Nucleation followed by capping of barbed ends in lamellipodia **(1d)** or severing, followed by capping of barbed ends in filopodia **(2d)**, produce an excess of free pointed ends compared to barbed ends, leading to a more rapid growth of remaining barbed ends (known as funneling). The intrinsic low rate of treadmilling of actin filaments is accelerated by the synergistic action of cofilin and profilin **(e)**. (Borisy, 2000).

The functions of pseudopodia include locomotion and the capture of prey. Pseudopodia are critical in sensing prey that can then be engulfed; the engulfing pseudopodia are called phagocytosis pseudopodia. In this way, a well known example of related-behaviour with amoeboid cell is the human white blood cell (leukocytes).

The lamellipodium is a cytoskeletal actin projection on the mobile edge of the cell. It contains a two-dimensional actin mesh which pushes the cell membrane across a substrate. The lamellipodium is created by actin nucleation at the plasma membrane of the cell (Alberts, 2008) and is the primary area of actin incorporation or microfilament

formation in some cells. Lamellipodia are found primarily in very mobile keratocyte in the skin, which are involved in rapid wound repair, crawling at speeds of 10-20 μm/minute over epithelial surfaces. Lamellipodia are a characteristic feature at the front, leading edge, of motile cells.

The uropodium is a rigid membrane projection with related cytoskeletal components at the trailing edge of a cell in the process of migrating or being activated, found on the opposite side of the cell from the lamellipodium.

Filopodia are finger-like extensions of the cell surface that are involved in sensing the environment, in attachment of particles for phagocytosis, in anchorage of cells on a substratum (Heid, 2005), and in the response to chemoattractants (Diez, 2005), or other guidance cues. Filopodia represent an excellent model for actin-driven membrane protrusion of *Dictyostelium* cells (Medalia, 2006).

The implication of different key regulators of cellular activities (e.g. Ras family-small G proteins that have many effectors, Rac, Cdc42-two Rho family GTPases or VASP, WAVE and Arp2/3 complexes) in signaling transduction pathways (mediating downstream signaling) and their connections with cell motility and morphology was widely studied (Dumontier, 2000; Chen, 2000; Han, 2002; Steffen, 2006; Para, 2009). For example, in Fig. 1.17 it is shown that dominant RasG inactivation results in the reduction of filopodia (Chen, 2000).

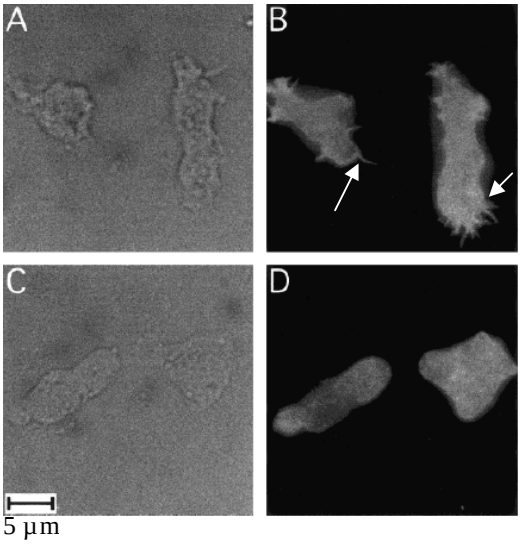

Fig. 1.17 Visualization of filopodia (pointed by white arrows) on wild type cells and RasG(G12T) transformants. F-actin was stained with rhodamine-phalloidin after fixation of vegetative *Dictyostelium* amoebae on a glass surface. **A, B:** wild type KAX-3 cells; **C, D:** RasG(G12T) transformants. Scale bar 5 μm (Chen, 2000)

In their natural environment, *Dictyostelium* cells migrate on or within three-dimensional (3D) complex substrates such as soil particles, fragmented leaves, and debris

of very different physicochemical properties. The cells are able to adhere and to move on humid as well as on dry substrates. Consequently, amoeboid migration must be a very robust process that is resistant to many adverse events. Cell movement is a cycling multistep process that requires the integration of complex biochemical and biophysical cell functions. Using protein micropatterning techniques to control cell environment at the micrometer scale, it has been shown that cell morphology and internal organization is influenced by the geometry of cell-surface contact zones (Jiang, 2005). An elusive question is the molecular identity of the dynamic signaling pathways translating the adhesive environment into a polarized response. As for mammalian cells, these pathways remain also partially known in the case of *Dictyostelium* amoebae. One possibility is that a biochemical signal is synthesized by adhesion receptors upon contact with the surface, which subsequently diffuses throughout the cell. In function of how the receptors are activated and which key regulators are activated (which signal transduction pathway is "used"), different organizations of actin cytoskeleton can be induced (Ridley, 1993). A more sophisticated mechanism is that mechanoreceptors sense mechanical constraints due to cell adhesion to the surface (Thery, 2006a).

Different cells solve this challenge differently, which leads to differences in migration strategies. The hallmarks of amoeboid movement include a simple polarized shape, dynamic pseudopod protrusion and retraction (Russ, 2006), flexible oscillatory shape changes, and rapid low-affinity crawling (Friedl, 2001). These morphological oscillations are not random and they appear to be associated with intrinsic physicochemical oscillations of actin polarization leading to pseudopodal extensions and retractions (Killich, 1993). Excitation waves of F-actin assembly develop and propagate for several micrometers at up to 26 µm/min. Wave propagation and extinction coincide with the initiation and attenuation of pseudopodium extension and cell advance, respectively (Vicker, 2000).

1.2.7 Focal adhesion/contact and adhesion sites in *D. discoideum*

In order to efficiently exert forces on a substrate, the cell has to attach on it, such that actin filaments transmit traction forces to the substrate at cell-substrate adhesion sites.

Cell adhesion is essential for cell migration, tissue organization and differentiation, therefore playing central roles in embryonic development, remodeling and homeostasis of tissue and organs, metastasis, phagocytosis. Cells usually adhere to extracellular matrix molecules, and a few of them (platelets, blood monocytes, osteoclasts, amoebae) also adhere to plain or coated solid materials. Adhesion dependent signals control the actin cytoskeleton assembly and cooperate with other signaling pathways to regulate biological functions such as cell survival, cell proliferation and cell differentiation. Cell migration and invasion are integrated processes requiring the coordinated assembly and disassembly of integrin-mediated adhesions and their coupling to the actin cytoskeleton dynamics (Delon, 2007; Vicente-Manzanares, 2009; Block, 2008).

Cellular adhesive structures consist of transmembrane adhesion molecules linked to the actin cytoskeleton and a signal transduction machinery aiming to assemble and disassemble it. In mammals, **focal adhesions** (FA; Fig. 1.18A) contain adhesion receptors, called integrins, cytoskeletal and signaling molecules in multimolecular complexes of 0.5–2 µm in diameter. Integrins bound to extracellular ligands (fibronectin) become linked to the actin cytoskeleton via several adapter and signaling proteins, such as talin, vinculin, α-actinin (not shown), filamin, focal adhesion kinase (FAK), and paxilin. FAK phosphorylates tyrosine domains of some signaling proteins, its activity being monitored the presence of phospho-tyrosines (Fig. 1.18B). In the mammals, the hallmark of FA is the presence of actin stress fibers parallel with the substratum that connects the FA.

Fully matured focal adhesions are formed at the leading extending edge of the cells and represent relatively stable cell-substrate interactions that persist as long as the cells are attached to the substrate (Friedl, 2001, Bukahrova, 2005).

The **focal contact** is smaller, less developed, and more transient compared to focal adhesions (Burridge, 1996). Focal contacts contain smaller clusters of adhesion receptors and a reduced array of cytoskeletal and signaling elements, which are not linked to stress fibers but rather to a more diffuse cortical F-actin (Burridge, 1996). Focal contacts are thought to represent more dynamic junctions predominantly under the control of Rac and Cdc42 signaling proteins (Nobes, 1999).

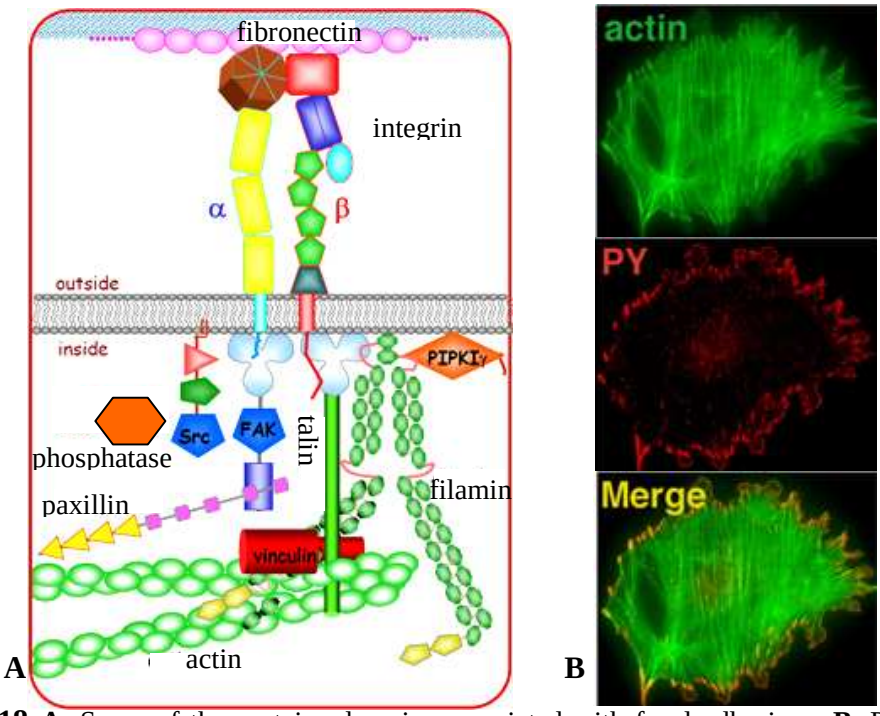

Fig. 1.18 A. Some of the proteins domains associated with focal adhesions. **B**. Porcine aortic endothelial cells, double-labeled for actin (green) and phospho-tyrosine (PY, red). Notice focal complexes at the cell edge and focal adhesions at the ends of actin cables (Geiger, 2001).

Dictyostelium cells are similar to leukocytes, in that they are fast-moving cells with an irregular shape. No structure similar to actin stress fiber has been found in *Dictyostelium*. Nevertheless, in *Dictyostelium*, several plasma membrane proteins (described above) have been identified that mediate adhesion. Some of these proteins are similar to β-integrins (SibA), which mediate interaction of higher eukaryotic cells with extracellular matrix proteins (Cornillon, 2006; Cornillon, 2008). In adition, *D. discoideum* also possesses many proteins known to be part of adhesion structures in higher eukaryotes, such as talinA, talin B (Niewohner, 1997; Tsujioka, 2008), paxillin (Bukahrova, 2005; Duran, 2009), coronin (de Hostos, 1991; Gerisch, 1993), ERMs, FAK, certain myosins (Patel, 2008), phg1, phg2 (Gebbie, 2004), Src-like tyrosine kinase (Moniakis, 2001). They stimulate actin polymerization (not all, some stimulate depolymerization) and link the attachment of actin microfilaments to the plasma membrane.

TalA$^-$ cells show reduced adhesion to the substrate and slightly impaired cytokinesis in the vegetative stage, while the development is normal (Tsujioka, 2008).

Phg2 seems to play a specific role in signaling actin polymerization/depolymerization at places where the amoeba comes into direct contact with a substrate (Gebbie, 2004). Paxillin is a key regulator component of focal adhesion sites, implicated in controlling cell-substrate interactions and cell movement (Bukahrova, 2005).

Two actin-containing structures have been proposed to act as ”feet” in *Dictyostelium* cells (adhesion sites). One of the candidates is the **eupodium** (Fig. 1.19), but this appears only in cells that are under the pressure of the agar sheet (Fukui, 1999). Eupodia are F-actin containing cortical structures similar to vertebrate podosomes (for example, in lymphocytes) or invadopodia found in metastatic cells. Eupodia are rich in actin binding proteins such as α-actinin, myosin I B/D, ABP120, cofilin, coronin, and fimbrin, but not a homologue of talin. There is a precise spatiotemporal coupling between F-actin assembly in eupodia and lamellipodial protrusion. When a lamellipodium advances to invade a tight free space, additional rows of eupodia (0.5 – 1 µm) are sequentially formed at the base of that lamellipodium.

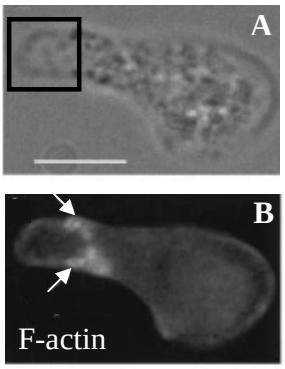

Fig 1.19 Immunofluorescence localization of actin in eupodia. The cells were prepared by the agar-overlay method. The cells migrate toward the left of the field. **A.** Phase-contrast image of a single active cell. The lamellipodium (black square) appears to be invading a space between the glass coverslip and the agarose overlay. **B.** The bright dots at the base of the lamellipodium (arrows) are eupodia. Scale bar, 5 µm.

The other is **actin foci**, which are observed on the ventral membrane of freely migrating cells (Yumura, 1990). When the cells are stained with ConcanavalinA protein which covalently bound the oligosaccharide chains of the glycoproteins, distinct patterns of dots and short fibers, which are referred to as cellular tracks (CTs), are observed behind the cells (Uchida, 1999). Since the dots in CTs contain actin and α-actinin, it is conceivable that they are derived from actin foci.

Actin foci are very dynamic structures that appear and disappear at the surface on the substratum during cell migration (Bretschneider, 2004). The velocity of the cells is inversely proportional to the number of actin foci (Uchida, 2004). Reflection interference

microscopy revealed that the ventral cell membrane was closer to the substratum at sites of actin foci (Uchida, 2004). Furthermore, some actin foci are incorporated into the retraction fibers, ripped off from the cells and eventually shed on the substratum after the cells move away (Uchida, 2004). These authors measured the traction force using a silicone substratum and demonstrated that the traction force was transmitted to the substratum through actin foci. They also found evidence suggesting that changing step is regulated in a coordinated manner during cell migration. Several lines of evidence strongly suggest that actin foci function as the active "feet" of *Dictyostelium* cells.

Figure 1.20A and B show live observations of GFP-actin expressing cells by fluorescence microscopy and the appearance of several fluorescent dots, present on the ventral cell membrane. The diameter of the fluorescent dots ranges from 0.3 to 1.0 µm, with an average diameter of 0.53±0.12 µm (for n = 30 fluorescent dots). Interestingly, the appearance of actin foci was transient (~20 s) and their positions on the substratum were unchanged during this time (Fig. 1.20C).

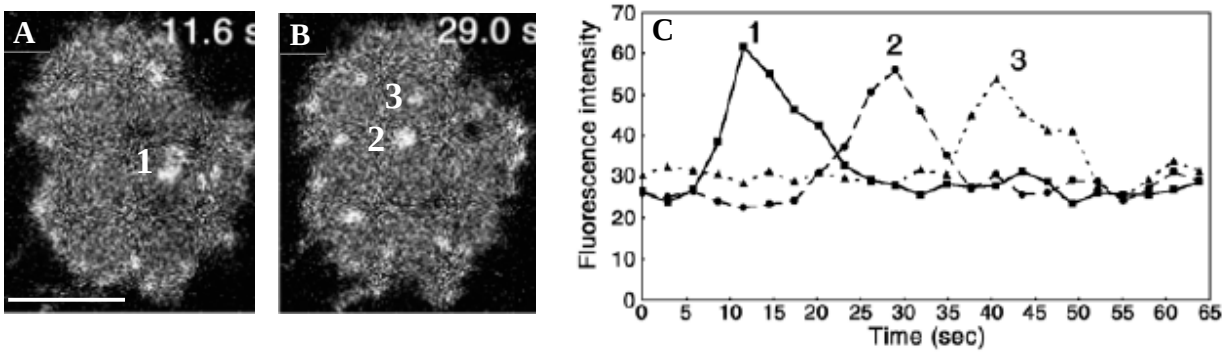

Fig. 1.20 A, B. Dynamics of actin foci in live cells as seen by fluorescence microscopy using actin GFP. The ventral membrane of a quiescent *Dictyostelium* cell was analyzed at various time points, as indicated. **C** Time course of fluorescence intensity of the three actin foci indicated in A and B. (Uchida, 2004)

To investigate whether these actin spots co-localize with the areas of paxilin enrichment, Bukahrova et al. (Bukahrova, 2005) produced a cell expressing both PaxB-GFP and a red fluorescent actin binding domain of ABP120 protein (a protein which appears in actin foci; Bretschneider, 2004). Observation of the actin foci and PaxB foci showed that the actin foci were much more dynamic (with half-life approximately 9 s) and, in general, did not coincide with the paxillin foci (Fig. 1. 21). The PaxB foci originated at the leading edge of the cell and stayed present during the time the surface

was in contact with the substrate (these structures look like authentic focal adhesion sites), while the actin foci could arise anywhere and be disassembled, while the surface was still in contact with the substrate. This indicates that these PaxB and actin foci may serve different functions (Bukahrova, 2005). Actin foci underneath the cell ventral surface could be sites of pseudopodia and may have a roll in cell positioning, force transmitting and stability on the substrate.

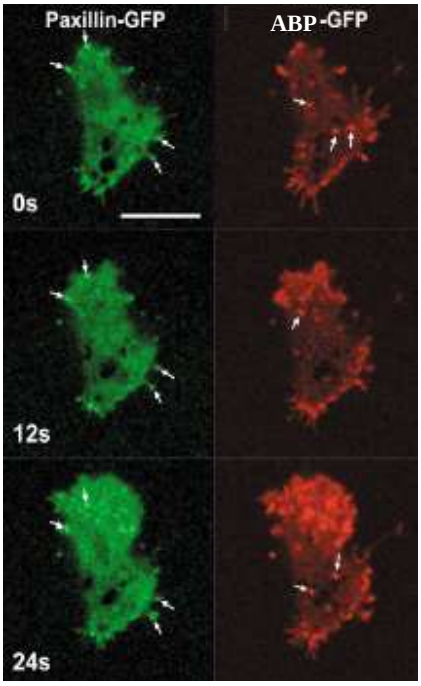

Fig. 1.21 Co-localisation of PaxB-GFP and ABP120-GFP. Confocal time series of vegetative wild-type AX2 cell expressing PaxB-GFP and ABP120-GFP. PaxB-GFP (green) localizes to long live stationary contact sites at the cell/substratum interface as indicated by the arrows that mark the same contact sites at different time points. ABP120-GFP (red) accumulates at very short-lived contact sites as indicated by the arrows. Scale bar, 10 µm.

Moreover, the active structures of dynamic pseudopodium extension and cell advance, respectively, are the short-lived actin rich-spots of short-life with different sizes and shapes (half life of 9 s; Bretschneider, 2004) which appear at the cell edges.

1.2.8 Dictyostelium spreading

An understanding of how adhesion and actin polymerization are coordinated is fundamental to physiological and pathological situations, like wound healing, the infiltration of macrophages into tissues in chronic inflammatory diseases or cancers.

In order to separate protrusion from retraction, Keller et al. (Keller, submitted) studied the temporal and spatial dynamics of *D. discoideum* cell-surface contact area

during spreading and their results support the physical model of spreading proposed by Chamaraux (Chamaraux, 2005). They provided evidence that, despite size, shape and speed variability, cells possess common spreading characteristics. Protrusion activity exhibits quasi-periodic variations, even in the presence of very low retraction activity, with a conserved 11 s period. They also studied the effect of external calcium on the morphology and kinetics of spreading.

The spreading process is presumably initiated by a first contact with a surface (Stossel, 1999). It comprises five steps: (1) In initial actin nucleation, extern signals are integrated by G-proteins and phosphoinositols (PIPs) leading to local actin polymerization. (2) during filament growth, as a result of actin polymerization, a pseudopod is formed and protruded; the development of a pseudopod results from elongation and cross-linking of polymerized actin to a viscous gel and unilateral swelling, prompting the outward pushing of the plasma membrane, extension of one or several leading pseudopods, and acquisition of a polarized cell shape. (3) during attachment, the pseudopods establish an interaction towards the underlying substrate by adhesion mechanisms that, in the case of *Dictyostelium*, remains to be defined on a molecular level. (4) contraction by filament sliding occurs after attachment of the cell to the substrate and elongation of the cell body; this contraction provides the force for translocation, and contractile force is putatively provided by myosin motors and additional mechanisms. (5) the spreading is terminated when retraction and detachment of the cell rear occurs, during which localized release of adhesive bonds at the trailing edge allows the detachment and retraction of the rear end into the advancing cell body.

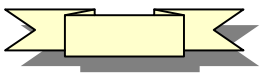

Dictyostelium discoideum are simple eukaryotic cells able to adhere and spread on plain materials (hydrophilic and hydrophobic) of surprisingly variable surface characteristics.

The contact of cells with a solid surface is a complex process and triggers important intracellular signalization pathways, leading to cell spreading, polarization, motility, proliferation and eventually differentiation. The number of proteins involved in

cell adhesion is quite large and involves many molecular interactions (Geiger, 2001). Despite our knowledge of many elements that play a role in adhesion, their temporal hierarchy and spatial organization is only partially understood. It is challenging to identify the successive formation of protein complexes leading to stable cell-surface contacts. Synchronizing cell-surface contact is a prerequisite for the preparation of cell material enriched in protein complexes active at a given time after contact. A biochemical analysis will be profitable when an entire cell population (minimum one million cells) will make the first contact point with a surface at the same time, starting the actin polymerization process in a synchronized way for all cells.

It would therefore be useful to synchronize the onset of cell-surface spreading, to get access to the different phases of this activity. In view of this, we investigated the possibility to modulate electrostatic repulsion between cells and a surface (glass, ITO, etc.) to control the formation of an initial cell-substrate contact. Moreover, electric fields could be used to diminish the repulsion between cells and a conductive surface.

1.3 Cell manipulation using electric fields

1.3.1 Electroactive substrates to control cell adhesion

Cell adhesion to material surfaces and the subsequent cell activities (spreading, focal adhesion, migration and proliferation) firstly depend on the presence and the location of specific extracellular matrix molecules and are highly sensitive to the surface chemistry and its physical environment. This includes the stiffness of the materials, and the topography of the surfaces on which cells adhere, as well as the geometry of chemical patterns on surfaces (Simon, 2006). Adsorption of macromolecules and surface functionalization are therefore essential. On the long term, remodelling of the extracellular matrix, secretion or storage of growth and differentiation factors, proper material stiffness will be determinant. A complete characterization of material properties is thus necessary. Mastering these processes is crucial for the good integration of substituting biomedical materials and for the compatibility between medical implants and

living tissues. It is also important for research in biology, since eukaryote cells are often grown on material surfaces. Furthermore, as the interaction between cells and materials extends over different scales, from nm (typical size of macromolecules), to several µm (cell geometry), micro- and nanotechnology are therefore well suited to engineer material surfaces for biological use, in order to provide cells in precise and well characterized conditions.

Material surfaces can be engineered not only to selectively control cell adhesion in a persistent manner, but also to switch from a non-adhesive to an adhesive state. A range of surfaces have been developed, whose hydrophobicity can be controlled either electrically (Lahann, 2003), electrochemically (Wang, 2003), thermally (Moran, 2006), or photoactively. Surface hydrophobicity is an interesting parameter to modulate cell adhesion because most proteins, including extracellular matrix ones, bind more strongly on hydrophobic surfaces than on hydrophilic ones (which is not the case for *Dictyostelium*, because amoebae adheres on plenty materials either hydrophobic or hydrophilic ones). However, large changes are necessary to significantly modify protein adsorption. Therefore, surface switching often relies on other physico-chemical mechanisms to change cell adhesion. In addition, caution should be exerted when using physical forces since living cells are very sensitive to their environment. Electrowetting for instance, requires large electric voltages to be effective in physiologically relevant solutions, which may trigger electrophysiological responses. In the same way, strong UV illumination is necessary for photo-induced wetting, which is harmful to cells. Consequently, these techniques have not yet been employed to control cell adhesion. Electrochemical and thermal switching are more cell-friendly techniques and several researchers have already demonstrated promising applications.

Thermal switching is based on hydrogels that are film-coated over the surface and exhibit a transition between a collapsed and a swollen structure at a critical solution temperature (LCST). An example of such a thermo-responsive polymer is poly(N-isopropylacrylamide or PNIPAAm, whose LCST is in the range of 32-35°C. This surface can interchange between hydrophobic, above the LCST, and hydrophilic, below the LCST. The LCST of PNIPAAm and its copolymers is at a physiologically relevant temperature, thus allowing the surface to be developed as a novel substrate for cell

culture and recovery without the use of harmful proteolytic enzymes such as trypsin or dispase (Moran, 2006). Cells adhere, spread and grow well on PNIPAAm hydrogels at 37°C, since the dehydrated polymer surface is hydrophobic which allows strong extracellular matrix protein binding. Reducing the temperature below LCST makes the surface hydrophilic and swelling exerts large mechanical forces, which induce detachment of a cell sheet including an intact extracellular matrix (Moran, 2006). This substrate is not adapted for *Dictyostelium* cells, since they have no extracellular matrix and also they do not survive at 37°C.

Electrochemical switching can be achieved in different ways. One possibility is to change the redox state of a molecule grafted to the material surface. The resulting surface voltage change exerts repulsive or attractive forces on adsorbed or covalently bound molecules, which drives a conformational change. Wang et al. (Wang, 2003) tethered bipyridinium molecules through an alkylated linker to an electrode and showed that redox modification of the bipyrinidium group bended the linker towards the surface, exposing the most hydrophobic part of the molecule (Fig. 1. 22). A reversible, but modest, surface energy change accompanies voltage application.

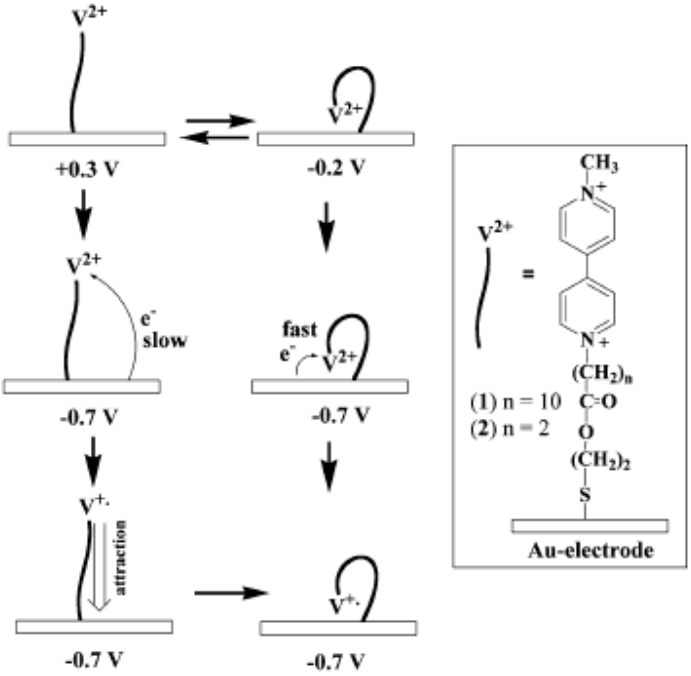

Fig 1. 22 Potential-induced molecular motion and redox-transformation of a bipyridinium monolayer associated with an electrode surface. (Wang, 2003)

Another approach is to release or bind biomolecules from or to the surface. For example, thiol chemistry on gold surfaces can be used for electrochemically bind or release a self-assembled monolayer. Yousaf et al. (Yousaf, 2001) reported the development of an electroactive mask that permits the patterning of two different cell populations to a single substrate. The key element in this method is to be able to turn on selected regions of a substrate. The authors use a self-assembled monolayer (SAM) that presents hydroquinone groups among a background of penta-(ethylene glycol) groups (Fig. 1. 23).

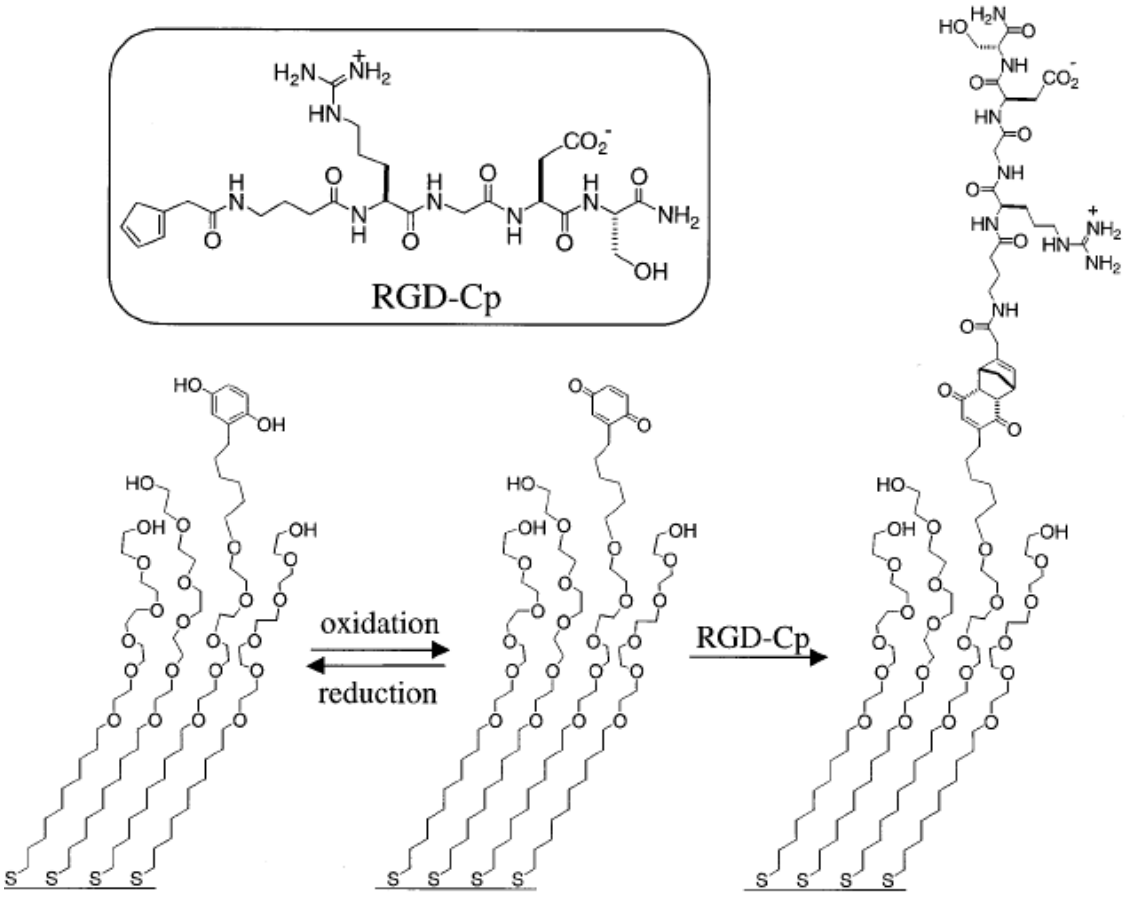

Fig. 1. 23 Molecular strategy for creating substrates that can be electrically switched to permit cell attachment. A monolayer presenting a mixture of hydroquinone groups and penta(ethylene glycol) groups (Left) is converted to a monolayer presenting the corresponding quinone groups (Center) by application of a potential to the underlying gold (500 mV versus Ag/AgCl). Both monolayers are inert to the attachment of cells. Addition of a conjugate of cyclopentadiene and the peptide Gly-Arg-Gly-Asp-Ser-NH2 (RGD-Cp) to the monolayer presenting the quinone group results in the Diels-Alder-mediated immobilization of peptide (Right). 3T3 fibroblasts attach and spread on the resulting surface. Monolayers presenting the hydroquinone group are unaffected by the treatment with RGD-Cp and remain inert to cell attachment (Yousaf, 2001).

The hydroquinone group undergoes oxidation when an electrical potential of 500 mV versus Ag/AgCl is applied to the underlying gold film to give the corresponding benzoquinone. This benzoquinone (but not the hydroquinone) then undergoes a selective and efficient Diels-Alder reaction with cyclopentadiene to form a covalent adduct. They used conjugates of cyclopentadiene and the peptide Gly-Arg-Gly-Asp-Ser-NH2 (RGD-Cp). Because this peptide is a ligand that binds to integrin receptors and mediates cell adhesion, the immobilization of this conjugate gives a surface to which cells can attach efficiently. The penta-(ethylene glycol) groups of the monolayer are critical to this design because they prevent the attachment of cells (they are inert to the nonspecific adsorption of protein) (Yousaf, 2001).

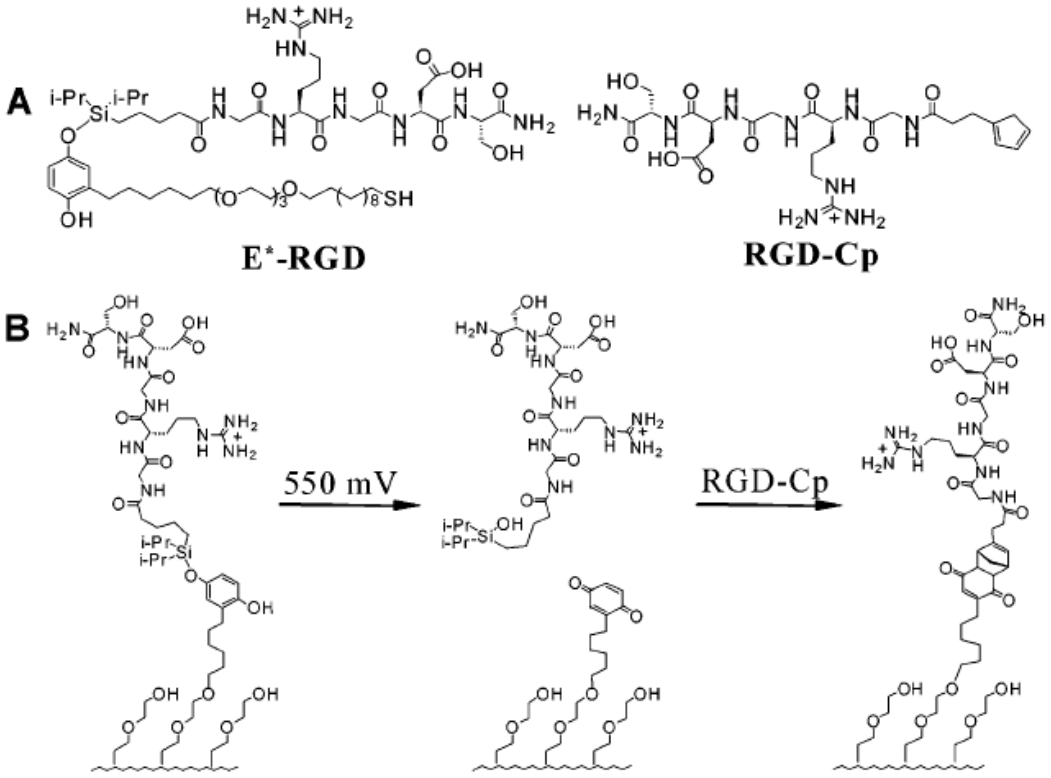

Fig. 1. 24 (A) Structures for the functionalized alkanethiol used to prepare dynamic substrates (E*-RGD) and the cyclopentadiene moiety (RGD-Cp) used to selectively immobilize ligand. (B) A monolayer presenting the *O*-silyl hydroquinone undergoes electrochemical oxidation to give a benzoquinone, with hydrolysis of the silyl ether and selective release of the RGD ligand. The resulting benzoquinone reacts with RGD-Cp by way of a Diels-Alder reaction, which selectively immobilizes the second ligand. The RGD peptide mediates the adhesion of cells (Yeo, 2003).

Yeo et al. (Yeo, 2003) prepared an electroactive self-assembled monolayer presenting an RGD peptide linked to an O-silyl hydroquinone group (E^*-RGD, Fig. 1.24) and allows for selective release of the adhering cells (swiss 3T3 fibroblast).

Applying for 5 minutes an electrical potential (550 mV versus Ag/AgCl) to the substrate oxidized the hydroquinone and released the RGD group, resulting in the detachment of cells attached to the RGD moiety. Subsequent treatment of the surface with diene-tagged RGD peptides (RGD-cp) restores cell adhesion after several hours (Fig. 1. 25).

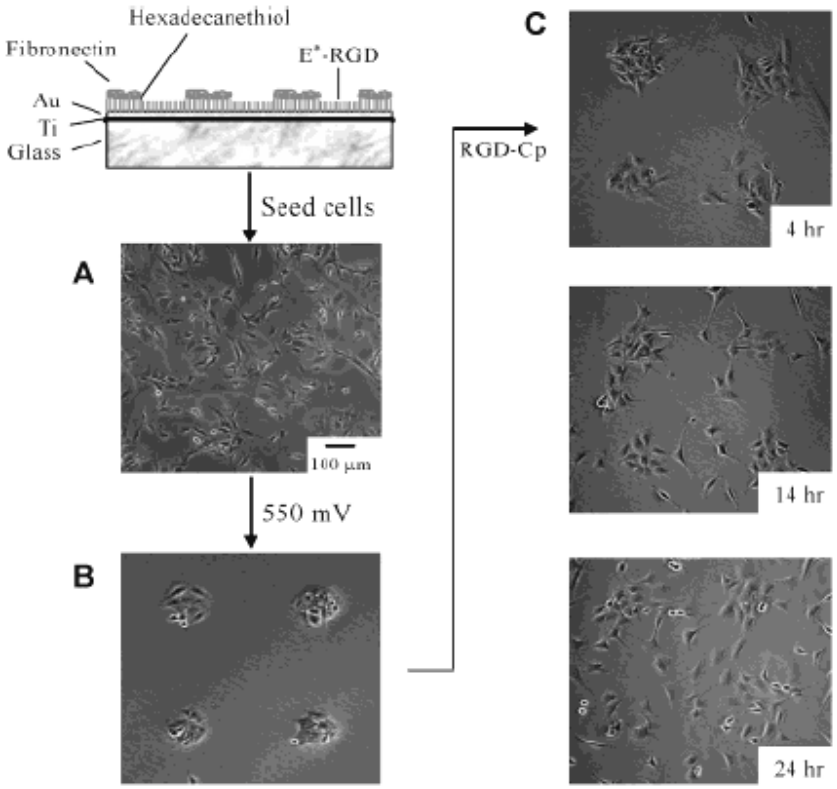

Fig. 1.25 Demonstration of a substrate combining two dynamic properties: (i) the release of RGD ligands and, thus, the release of cells, (ii) the immobilization of RGD ligands and, hence, migration and growth of cells. A monolayer was patterned into circular regions that present fibronectin and surrounded by RGD ligands tethered by way of an electroactive linker (E*-RGD). (A) Swiss 3T3 fibroblast cells adhered and spread evenly over entire substrate. (B) An electrical potential of 550 mV was applied to the substrate for 5 min, and the substrate was incubated for 4 h. Cells were efficiently released only from the E*-RGD regions. (C) Treatment of the monolayer with RGD-Cp resulted in ligand immobilization and initiated cell migration from fibronectin regions onto remaining regions. After 24 h, cells were distributed evenly over the substrate (Yeo, 2003).

Inversely, Tang et al. (Tang, 2006) coated an indium tin oxide microelectrode array with a protein-resistant (poly-lysine)-graft-polyethylene glycol copolymer. Application of a positive electric potential resulted in localized polymer desorption, thanks to the positively charged PLL moiety and freed the ITO surface for subsequent protein binding. It should be noted that this technique is relatively slow, since 24 s are required to fully remove adsorbed molecules from the electrodes. This electrochemical switching is therefore only applicable to cells that spread or move rather slowly.

Mali et al. (Mali, 2006) demonstrated that proteins undergo similar electrochemical transformations: they could be patterned on addressable gold electrodes and selectively released from them.

1.3.2 Influences of electrical field on the cells and cell-size model membrane systems (liposomes)

1.3.2.1 Electrotaxis

There is a long history of the use of electrical stimulation in medicine. For instance, the romans used the discharge from electrical fish to treat a number of pathologies, including gout and sick headache. More recently, we have become aware that many tissues generate their own electrical signals (physiological endogenous electric fields of 42-100 mV/mm (Barker, 1982)) which are present generally in the extracellular spaces, for minutes, hours, even days. It is thought that a host of basic cell behaviours such as cell shape, cell migration, cell division, and cell proliferation may be all controlled by these small electrical signals during normal development (McCaig, 2005). Motile cells could detect gradients in electrical potential and show directional migration (*electrotaxis*) towards the wound centre, when an external (exogen) DC electric field is applied. The applied electric field has strength comparable to the strength of endogenous wound electric fields (Fig. 1.26c). Very short (<200 μs) high voltage stimulations (100-500 V) can also be applied, both methods applying without the occurring of significant electrochemical reactions at the electrodes (Alon, 1987; Franek, 2000).

Following damage in several systems, steady electrical signals re-appear and again seem to regulate a range of coordinated cell activities. In epithelial tissues such as

skin and cornea, there is direct evidence for electrical regulation of the axis of cell division, the rate of cell proliferation and the direction of cell migration (Zhao, 2002a). These events need to be coordinated for successful wound healing to occur. Since there is evidence that these electrical signals may be the earliest to appear at a wound and that they may override coexisting chemical signals (Zhao, 2002b), they could act as a master regulator signal to quick start an integrated array of coordinated cell behaviours (Zhao, 2006, Fig. 1.26a, b).

The mechanisms underlying the generation of these signals and the varying mechanisms by which electrical signals direct nerve guidance and cell (epithelial, cancer, etc.) migration are widely explored. In the case of electronic stimulation of neuronal activity, a displacement current across electrolyte-oxide-semiconductor (EOS) capacitors gives rise to a voltage across the cell membrane that opens ion channels (Fromherz, 2008). How are electric migration cues relayed into cellular responses? Because all cell types and intracellular organelles maintain transmembrane electrical potentials owing to asymmetric ion transport, wounding results in strong and directional ion flow after disruption of epithelial cell layers (Barker, 1982).

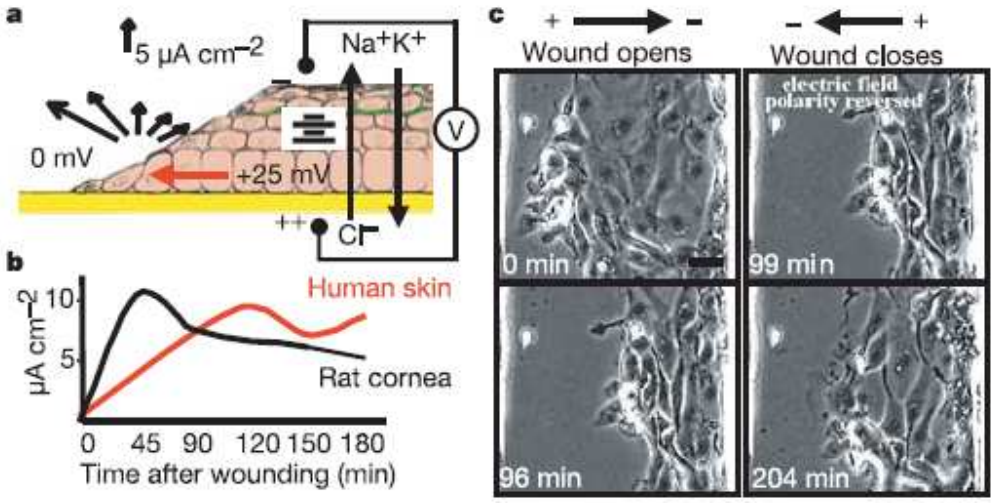

Fig. 1.26 Electrical signals direct cell migration in wound healing and activate selected signalling pathways. a) Wounding induces lateral electric fields directed towards the wound centre (red arrow), by collapsing the local transepithelial potential difference (V). Black arrows represent sizes and directions of currents. b) Directly measured currents increase over time in rat corneal and human skin wounds. c) An electric field (EF) directs migration of corneal epithelial cells in a monolayer model of wound healing (150 mV/mm). Scale bar in c) 20 μm (Zhao, 2006).

To identify possible mediators that couple electric stimuli to intracellular responses, Zhao et al. (Zhao, 2006) tested the role of ion transporters in the electrotactic response. In particular, the Na/H exchanger 1 (NHE1) has been implicated in directional cell migration (Denker, 2002). Testing two different types of NHE1 inhibitors, Zhao et al. found a decrease in the directedness of cell migration in electric fields. These results suggest that directional Na^+/H^+ transport by the NHE1 ion exchanger might relay the electric signal to PI(3)K activation with subsequent directional migration. In addition to Na^+/H^+ exchangers, it is likely that other ion channels such as Cl^- channels are also involved in electrotactic cell migration. Additionally, they found that electric stimulation triggers activation of Src and inositol–phospholipid signalling which polarizes in the direction of cell migration. Notably, genetic disruption of phosphatidylinositol-3-OH kinase-γ (PI(3)Kγ) decreases electric-field-induced signalling and abolishes directed movements of healing epithelium in response to electric signals. Deletion of the tumour suppressor phosphatase and tensin homolog (PTEN) enhances signalling and electrotactic responses. These data identify genes essential for electrical-signal-induced wound healing and show that PI(3)Kγ and PTEN control electrotaxis. Moreover, cathodally directed migration of corneal epithelial cells involved induced asymmetry of membrane lipids and associated EGF receptors, modulation of integrins, membrane surface charge (Rajnicek, 2008) and also asymmetric activation of MAP kinase signaling shown by leading edge asymmetry of dual phosphorylated extracellular signal–regulated kinase (Zhao, 2002a).

D. discoideum shows robust electrotaxis and migrates cathodally in an applied electric field (EF). Electrotaxis of *Dictyostelium* is voltage dependent, directedness increased with increasing field strength (Fig. 1.27) and the threshold voltage inducing directional migration is between 3 and 7 V/cm (300-700 mV/mm) (Zhao, 2002b).

Zhao et al. (Zhao, 2002b) concluded that reception and transduction of the electrotaxis signal are largely independent of G protein–coupled receptor signaling and that the pathways driving chemotaxis and electrotaxis do not use the same signaling elements. However, chemotaxis and electrotaxis intersect downstream of heterotrimeric G proteins to invoke cytoskeletal elements since actin was polymerized at the leading edge of cells during electrotaxis.

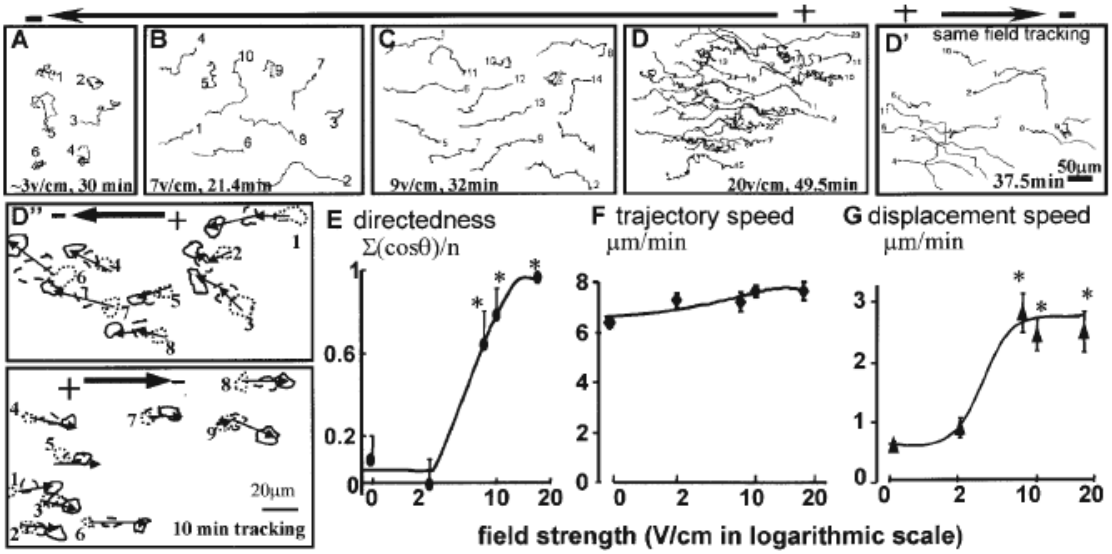

Fig. 1. 27 Wild-type *Dictyostelium* cells migrate cathodally (left) in a direct current (DC) EF as shown by trajectories mapping the cell centers starting from the numbered ends (B, C, and D). Electrotaxis depended on field strength (A–E and G). Reversal of field polarity reversed migration direction (D, D', and D''). D' is the same field tracking of D. D shows cell movements during 10 min field application pointing to the left and 10 min after reversing the field polarity. (E) Voltage dependence of electrotaxis (for directedness). Trajectory speed was similar between no field control and at different voltages (F), but movement in an EF was more persistent in one direction (G) (Zhao, 2002b).

1.3.2.2 Electrical forces (and their effects) for manipulating cells at the microscale

The main electrical forces for manipulating cells at the microscale are electrophoresis (EP) and dielectrophoresis (DEP). Electrophoretic forces arise from the interaction of a cell's charge and an electric field, whereas dielectrophoresis arises from a cell's polarizability. Both forces can be used to create microsystems that separate cell mixtures into its component cell types or act as electrical "handles" to transport cells or place them in specific locations (Voldman, 2006). In addition, two phenomena are able to reversibly modify the cell surface: electroporation and electrodeformation.

Electroporation and electrofusion are electric field–membrane coupled mechanisms (Teissie, 1986) related with EP or DEP, but more violent (usually 600-1600 V/cm for 0.1 ms to 5 ms at 1 Hz or 10-90 KV/cm nanopulses for tens of nanoseconds) (Beebe, 2005; Nuccitelli, 2009). Cell electroporation is routinely used in cell biology for protein, RNA or DNA transfer into the cells and was first described by Neumann almost

three decades ago (Neumann, 1982). Its clinical applications are under development for gene therapy and targeted intracellular drug delivery (especially for drugs with high toxicity), reducing the exposure time, doses of the administrated drug and associated side-effects. Nevertheless, the molecular mechanism supporting the induction of permeabilizing defects in the membrane assemblies remain poorly understood (Teissie, 2005; Kanduser, 2009).

Due to their molecular composition, in uniform or nonuniform fields, the cells and cell-sized vesicles will also experience an electrodeformation force proportional to $|E|^2$, where *E* is the electric field intensity (Riske, 2006). This force is usually negligible, but can be used intentionally to enhance cell electroporation and electrofusion. Riske and Dimova (Riske, 2005) used fast digital imaging to study the deformation and poration of cell-sized giant vesicles subjected to electric pulses (Fig. 1. 28). They revealed for the first time the dynamics of response and relaxation of the membrane at micron-scale level with a time resolution of 30 µs. Above a critical transmembrane potential the lipid bilayer ruptures and macropores (diameter ~2 µm) with pore lifetime of ~10 ms have been formed. The pore lifetime has been interpreted as interplay between the pore edge tension and the membrane viscosity.

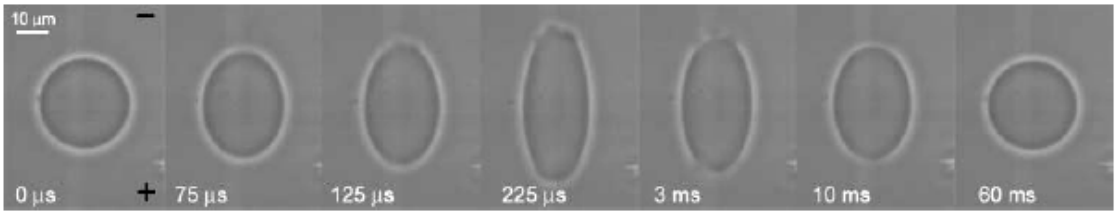

Fig. 1.28 A snapshot sequence of a vesicle subjected to a pulse, E = 2 kV/ cm, t_p = 200 µs. The image acquisition rate was 50 ps. Macropores are first visualized in the third frame (t = 125 µs). The electrode's polarity is indicated with a plus (+) and a minus (-) sign on the first snapshot. (Riske, 2005).

General characteristics of EP and DEP

As we have mentioned above, most cells are covered with negatively charged functional groups at neutral pH (Mehrishi, 2002). Because the cells are charged, they can be acted upon by electric fields. In water, the cells will move at a velocity given by the balance of the Coulomb ($\mathbf{F} = q \cdot \mathbf{E}$, where *q* is the net charge on the object and *E* is the applied electric field) and viscous drag forces, a process known as electrophoresis-EP (Figure 1. 29A, left).

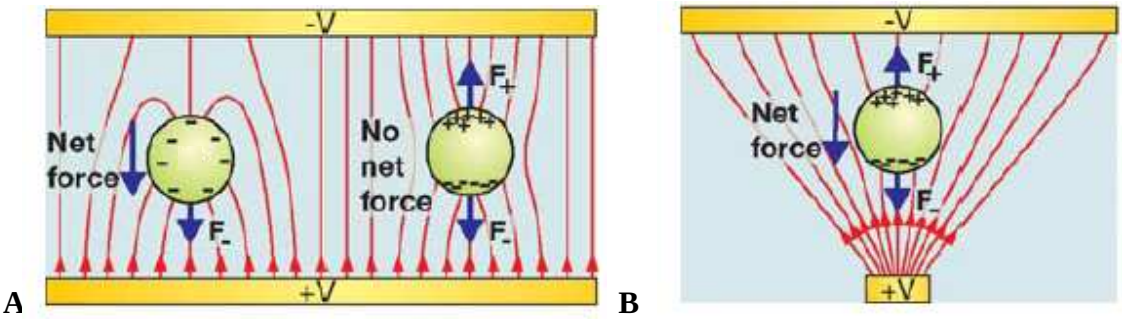

Fig. 1. 29 EP and DEP. **A)**. Charged and neutral particle in a uniform electric field. The charged particle (left) feels an EP force, whereas the dipole induced in the uncharged particle (right) will not result in a net force ($F_- = F_+$). **B)**. A neutral, polarized particle in a non-uniform electric field. The particle will experience a net force toward the electric-field maximum because the field magnitude is different at each end of the particle ($F_- > F_+$).

The electrophoretic mobility (μ) relating electric-field intensity (E) to velocity (v), ($v = E \cdot \mu$) is, to first order, given by $\mu = \varepsilon_m \xi / \eta$, where ε_m is the permittivity of the liquid, η is the liquid viscosity, and ξ is the zeta potential, which is primarily related to the particle's charge density and the ionic strength of the liquid (see Material and Methods). For most biological cells, the EP mobility is ~ 10^{-4} cm^2/Vs, or 1 μm/s in a field of 1 V/cm (Mehrishi, 2002). Any use of EP, therefore, to separate different cell types is therefore dependent on the zeta potential difference between cells.

Dielectrophoresis or DEP (in its simplest form) is due to the interaction of an induced particle's dipole and the spatial gradient of the non-uniform electric field. All particles (charged or not) exhibit dielectrophoretic activity in the presence of electric fields. However, the strength of the force depends strongly on the medium and particle electrical properties (permittivities, conductivities), on the particle shape and size, as well as on the frequency of the electric field. Consequently, fields of a particular frequency can manipulate particles with great selectivity. This has allowed, for example, the separation, the orientation and manipulation of cells (Wang, 1995; Gascoyne, 1997).

To obtain a practical force expression, we need to determine the dipole moment *p*. For cells, the dipole moment is induced by the applied electric field. When cells (and other polarizable particles) are placed in an electric field, a dipole is induced to satisfy the boundary conditions on the electric field. This induced dipole can be created by free charge, by polarization charge (e.g., water), or in general by a combination of the two.

The exact constitution of the dipole will be related to the frequency of the applied field. At low frequencies (down to DC) free-charge dipoles dominate, whereas polarization-charge dipoles dominate at high frequencies. One typically uses AC fields (rather than DC) for DEP because that will damp out EP-induced motion while minimizing physiological impact on the cells and any electrochemical reactions at the electrodes (Voldman, 2006). One general form of its expression is: $\mathbf{F}_{DEP} = \mathbf{p}\nabla\mathbf{E}$, (Washizu, 1992) where *p* is the particle dipole moment. One sees that the gradient of the electric field ($\nabla\mathbf{E}$) must be nonzero for the force to be nonzero, which can be explained with reference to Fig. 1.29. Here we see that if each half of a dipole sits in the same electric field (Fig. 1.29A, right), then the cell will experience equal opposing forces ($F_- = F_+$) and no net force. If, however, each half of the dipole is in a field of different magnitude ($F_- > F_+$, Fig. 1.29B), then the net force will be nonzero, driving the particle up the field gradient. We also note that if the dipole is not oriented along the field, then a nonzero torque will be created, forming the basis of electrorotation (Washizu, 1992).

In this regard, one finds that the imposed fields can exist within the cell membrane or the cytoplasm. At the frequencies used for electrical manipulation—DC to tens of MHz—the most probable route of interaction between the electric fields and the cell is at the membrane (Tsong, 1992). This is, as we have seen, because electric fields already exist at the cell membrane, generating endogenous transmembrane voltages in the tens of millivolts, and these voltages can affect voltage-sensitive proteins (e.g., voltage-gated ion channels (Catteral, 1995)). The imposed transmembrane voltage, which is added onto the endogenous transmembrane voltage, can be approximated at DC and low frequencies, as $1.5|\mathbf{E}|\mathbf{R}$ (where *E* is the electric field intensity and *R* is the radius of the cell). Therefore, at DC a 10 μm cell in a 10 kV/m field will experience a 75 mV imposed transmembrane potential, approximately equal to the endogenous potential (Voldman, 2006). In the context of DEP, some studies have been dedicated to measuring or estimating the induced transmembrane potentials at the cells (Glasser, 1998), but these have been difficult to measure, especially because the intrinsic nonuniformity of the electric field in DEP makes it impossible to assign it a unique value. In most studies, however, researchers have found no measurable effects due to field exposure (Glasser, 1998; Fuhr, 1994; Docoslis, 1999). Thus, DC fields-such as used in EP-will impose the

greatest stress on the cell membrane, whereas use of DEP in conditions under which the transmembrane loads and cell heating are small (KHz-MHz frequencies), is more benign.

1.3.2.3 Cells characterization, separation and handling using EP and DEP

At the microscale, there have been few reports using EP to separate, characterize cells, or for cell handling. This is perhaps due to the fact DC fields could be harmful to certain types of cells, limiting, thus, the fields that one can use. Nevertheless, there are reports that show that one can distinguish subtle phenotypic differences in mammalian cells, such as apoptosis (Guo, 2002) or different bacterial cell types (Armstrong, 1999) using EP. Moreover, the charged cells can move toward an electrode in an EP system. This points to one of the advantages of EP cell handling, which is that one can create electric fields, and thus transport cells, over large distances (up to centimeters). Portinga et al. (Portinga, 2001) described bacterial desorption and adsorption to indium tin oxide (ITO) electrode surface in a parallel plate flow chamber. If a high (≥65 μA) cathodic current was applied by adjusting the potential between -0.4 and -0.5 V, adhering bacteria were stimulated to desorb with desorption probabilities increasing with increasing current density. When a high (1.8 V; 2 mA) positive electrode potential was applied for 5 minutes, bacteria were forced to adhere and then, adhering bacteria could hardly be forced to desorb, indicating strong, irreversible adhesion.

If the field is nonuniform, the particles experience a translational force, known as the dielectrophoretic force (DEP), of a magnitude and polarity dependent on the electrical properties of the particles and their surrounding medium. This force is also a function of the magnitude and frequency of the applied electric field. For a spherical particle of radius R in an imposed electric field E (in V/m) of angular frequency ω, the magnitude of the dielectrophoretic force, F_{DEP} (in N), is given by the expression (Washizu, 1992):

$$F_{DEP} = 2\pi\varepsilon_m R^3 \, \mathrm{Re}\,(K^*)\nabla E^2_{rms} \qquad \text{Eq. 1.8}$$

where K^* is the complex Clausius–Mossotti factor, defined as:

$$K^* = \frac{\varepsilon_p^* - \varepsilon_m^*}{\varepsilon_p^* + 2\varepsilon_m^*} \text{ where } \varepsilon_p{}^* = \varepsilon_p - j\,\frac{\sigma_p}{\omega} \text{ and } \varepsilon_m{}^* = \varepsilon_m - j\,\frac{\sigma_m}{\omega} \qquad \text{Eq. 1.9}$$

The Clausius–Mossotti factor provides a measure of the strength of the effective polarization of a spherical particle as a function of particle and medium permittivity (ε) and conductivity (σ). The subscripts *p* and *m* refer to the particle and medium, respectively. Complex quantities are denoted with asterisks. *Re* stands for 'the real part of' the factor. The term ∇E^2_{rms} defines the average local nonuniform field strength and gradient (in V^2/m^3). If the real part of the Clausius–Mossotti factor is positive, the dielectrophoretic force is positive (pDEP). This means that the particle experiences a translational force directed towards regions of high electric field strength, such as the electrode edge. On the other hand, if the Clausius–Mossotti factor is negative, a negative dielectrophoretic force (nDEP) will direct it away from the high-field regions (Florez-Rodriguez, 2004; Huang, 2002; Haddrell, 2006), leading to the particle levitation. In the case of passive levitation, a negative dielectrophoretic force can balance a net gravitational force pointed in the opposite direction (Fig. 1.30). The net gravitational force, F_g, is determined by the difference between the gravitational force on the particle and the buoyancy force (Florez-Rodriguez, 2004).

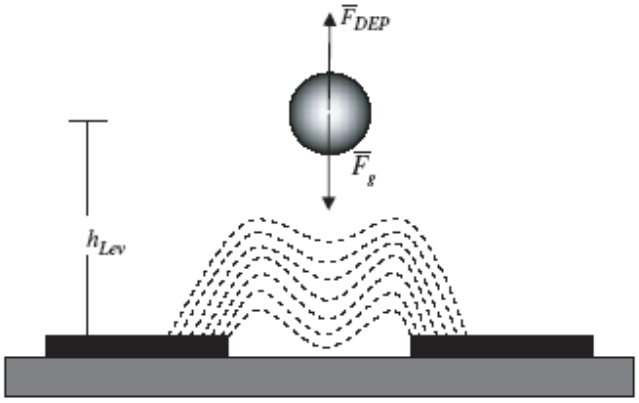

Fig. 1. 30 DEP levitation of particles above microelectrodes. The particles levitate to a height at which the DEP force, F_{DEP}, is equal and opposite to the net gravitational settling force, F_g.

Since both the DEP force and the gravitational force are dependent on R^3, particles with the same dielectric properties and density but different sizes can be expected to levitate to the same height. On the other hand, particles with differing dielectric properties will levitate to different heights in the chamber, irrespective of their size. Levitation has found many applications in particle characterization, separation, manipulation and trapping (Huang, 2002; Oblak, 2007; Vahey, 2008). The use of levitation reduces problems associated with particles adhering to the electrode surface,

steric hindrance and interparticle interactions that occur when the particles are confined to the two-dimensional electrode plane. Also, it prevents exposure to the possibly damagingly high fields and field gradients at the electrode surfaces. To achieve the optimum levitation height or trapping efficacy, it is often desirable to obtain the highest dielectrophoretic force for a given voltage. Experimentally, this is most easily achieved by raising the conductivity of the medium or its permittivity (or both) (Florez-Rodriguez, 2004).

For cells with very different electrical phenotypes, one can find a frequency and solution conductivity where one population of cells experiences pDEP and another nDEP. This allows for an easy separation, where one cell type will be attracted to the electrodes and the other repelled (Markx, 1994) (Fig. 1.31). This approach has been used to characterize, separate or transport live versus dead cells (Li, 2007), different species and cell types from each other (Huang, 2002) and cancer cell lines from dilute whole blood.

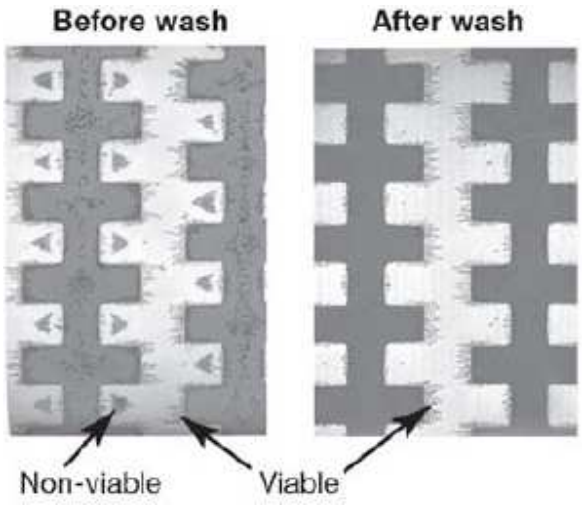

Fig. 1.31 Separation of viable and nonviable yeast. The left panel shows viable (experiencing pDEP) cells collecting on the electrodes and nonviable yeast (experiencing nDEP) collecting in between the electrodes. The nonviable cells can be removed by applying a fluid flow (right).

The primary technique which takes into account the magnitude of DEP, introduced in the late 1990s, is a type of field-flow fractionation-FFF (Vahey, 2008), where a perpendicular force (in this case, the nDEP force) moves cells to different heights in a parabolic flow chamber, where they then experience different drag forces and separate into bands (Fig. 1.32; Yang, 2000). The nDEP forces are balanced by the weight of the cell, resulting in a uniquely defined height.

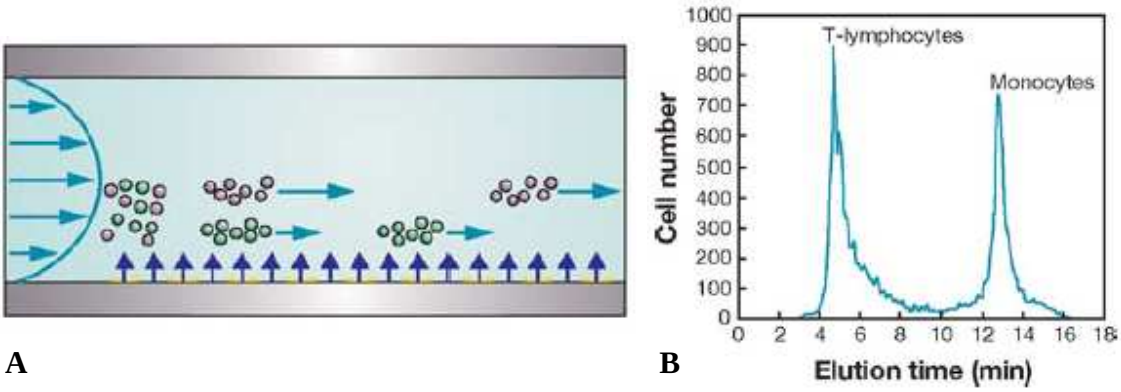

Fig. 1.32 A. Schematic of DEP-FFF (side view), showing that two cell populations, levitated to different heights by a DEP force, separate along the direction of flow in parabolic flow. **B** Separation of a mixture of human T-lymphocytes from monocytes using DEP-FFF. The monocytes are levitated to a lower average height and thus elute later than the T-lymphocytes.

Alternatively, static non-uniform electrical fields can be achieved under a DC electric field by specially designed features, such as obstruction or hurdles using electrically insulating materials. Some interesting applications of DC-DEP for particle separation in microsystems have been reported recently (Kang, 2006; Kang, 2008).

DC-Dielectrophoresis (DC-DEP), the induced motion of the dielectric particles in a spatially non-uniform DC electric field, is applied to separate biological cells by size. The cells experience a nDEP force at the corners of the hurdle where the gradient of local electric-field strength is the strongest. Thus, the moving cells deviate from the streamlines and the degree of deviation is dependent on the cell size. Kang et al. (Kang, 2008) demonstrated by using this method that, combined with the electroosmotic flow, mixed biological cells of a few to tens of micrometers difference in diameter can be continuously separated into different collecting wells (Fig. 1.33).

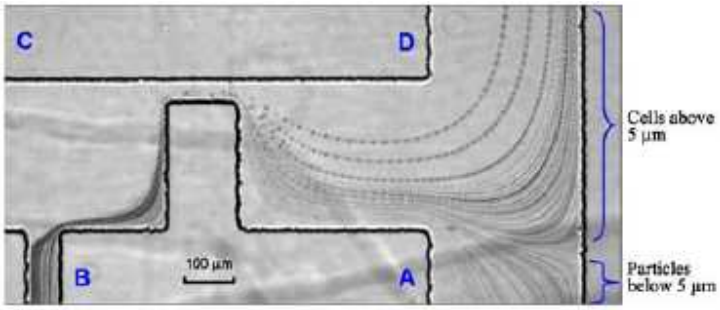

Fig. 1.33 Separation of the white blood cells: 5 µm threshold separation, V_A=102 V, V_B=191 V, V_C=343 V, V_D=0 V

For separating target cells of a specific size, all that is required is to adjust the voltage outputs of the electrodes.

DEP has been used extensively to handle cells, both for positioning and for transporting cells. Cell positioning typically uses stationary traps that may be turned ON or OFF in time. It is used either to create long term (more than several hours) patterns of cells on a substrate or for short term (minutes to hour) observation of cells in specific locations. Both pDEP and nDEP and many different geometries can be used for these purposes. In general, pDEP traps are easier to create than nDEP traps because it is easier to hold onto a particle by attracting it than repelling it. For example, Taff et al. (Taff, 2005) used the ring-dot geometry consisting of an outer ring electrode and an inner round "dot" electrode on a separate metal layer (Fig. 1. 34).

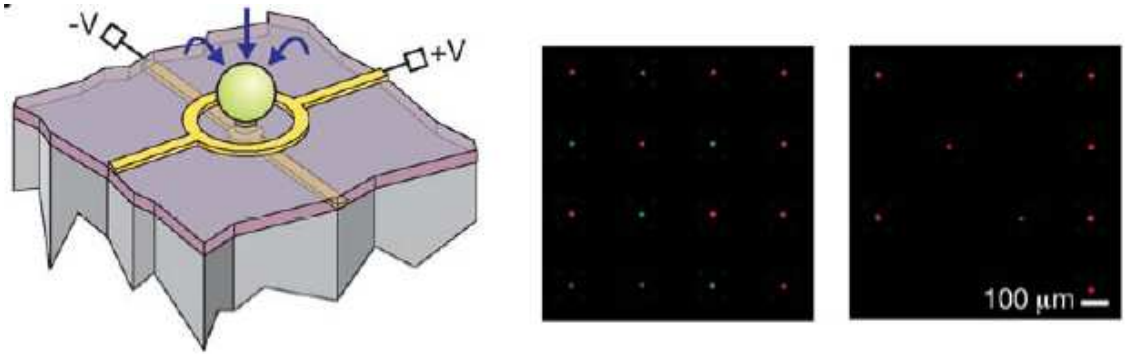

Fig. 1.34 Schematic (left) of ring-dot geometry, along with two images (right) showing addressable removal of green-labeled human HL-60 cells from a 4×4 trap array.

Cells are attracted via pDEP to the field maximum at the dot. Using this geometry they developed a scalable addressable trapping array for observing many single cells and then sorting out desired cells.

Electrical approaches to manipulating cells at the microscale have already shown great promise. This is primarily due to the favorable scaling of electrical forces with system size and the ease of fabricating microscale electrodes. Looking ahead, an upcoming goal for EP and DEP-based separations will be the demonstration of systems with specificity sufficient to enable separation of a few cells. Luckily, engineers continue to innovate in both DEP and EP separation and handling. It is however not possible to control thousands of cells simultaneously.

1.4 Objectives

In order to synchronize the onset of cell-surface spreading, we first investigated the possibility to modulate electrostatic repulsion between cells and a glass surface to control the formation of an initial cell-substrate contact.

We studied the formation of cell-surface contact as a function of ionic strength, then we show that it is possible to synchronize cell spreading either by changing the ion concentration around the cells or by electrochemical means.

We show in subchapter 3.1 that *Dictyostelium* cells spread using a periodic protrusion activity. Moreover, the actin polymerization activity, which drives membrane protrusions, is also oscillatory with almost the same period.

In the next subchapter, we will analyze the effect of an applied potential on the cells that are deposited on a conductive material. Using different conductive materials (ITO, Ti, Pt and Au) we tried to detach the adhering cells in 17 mM and 1.7 mM buffer solutions or to impair their contact with the surface by imposing a negative potential (current) at the material surface while they are sedimenting. Even the highest supportable potentials of materials and cells, did not allow to reach our aims.

In order to synchronize cell spreading, a new approach was taken into consideration and analyzed in the subchapter 3.3: to keep the living cells in suspension at a certain distance from the surface, despite the apparent gravity, using electrostatic properties of the cells and surfaces when we vary the ionic strength. Thus, by decreasing the ionic strength we can prevent cell adhesion using electrostatic repelling forces. We also use LimE$^{\Delta coil}$-GFP to monitor actin polymerisation activity. These experiments reveal that fluctuating actin polymerization occurs even in the absence of cell spreading.

In the last two subchapters, we analyze two different methods of adherence stimulation: using an experimental diffusion setup (subchapter 3.4) and an electrochemical method (subchapter 3.5).

Since *D. discoideum* adhesion is sensitive to ionic strength, we envisioned controlling this parameter in order to synchronize cell-surface contact. In subchapter 3.4 we show that by increasing the ionic strength we could induce cell adhesion and spreading. However, major drawbacks of this method are the unphysiological conditions

characterized by a high osmotic pressure reached in the chamber where the cells were levitating before concentrated solution diffused.

Using LimE$^{\Delta coil}$-GFP to monitor actin polymerisation activity, we finally show in subchapter 3.5 that synchronized cell spreading can be induced by a short electrical pulse (0.1 s) triggering a transient surface contact. As a consequence, the pulse-induced contact with the surface, triggers regular quasi-periodic actin polymerization, that is in phase in all the cells.

Chapter II. Materials and methods

2.1 Materials

2.1.1 Buffers and chemicals

Sörensen Buffer (SB) containing 2 mM Na_2HPO_4 (analytical grade) and 14.68 mM KH_2PO_4 (analytical grade) at pH 6.13 was used as a reference medium for the experiments. The theoretical osmolarity of this buffer is 36 mOsm and was experimentally measured with a Löser cryoscopy osmometer. The value of 34±3 mOsm was obtained.

Lowering buffer concentration was compensated for by adding osmotically equivalent amounts of D(+) sucrose. Solutions at a lower ionic concentration (phosphate sucrose buffers) were thus obtained by mixing appropriate volumes of SB and a 36 mM sucrose solution. Isotonic $CaCl_2$ solutions were prepared in the same way, using sucrose to maintain osmotic pressure.

Potassium hexacyanoferrate ($K_3Fe(CN)_6$), potassium nitrate, ferric chloride, anhydrous calcium chloride, hexahydrated magnesium chloride, sodium chloride, potassium chloride, cesium chloride, lithium perchlorate ($LiClO_4$), MES (2-(N-morpholino) ethanesulfonic acid, pKa = 6.09) and HEPES (4-(2 hydroxyetyl)-1-piperazineethane sulfonic acid, pKa = 7.67) and cysteine were analytical grade. The conductivity of hygroscopic ionic salt solutions was measured to ascertain their concentration. Aminopropyltriethoxysilane (APTES) and Latrunculin A were from SIGMA-ALDRICH (Saint Quentin Fallavier, France).

The solution conductivities were measured with an Analytical Radiometer, CDM 210, MeterLab apparatus.

2.1.2 *D. discoideum* culture and handling

D. discoideum AX2 cells were grown in agitated suspensions (180 rpm) in HL5 medium (FORMEDIUM, Norfolk, UK): peptone 14.3 $g.L^{-1}$, yeast extract 7.15 $g.L^{-1}$, maltose 18 $g.L^{-1}$, Na_2HPO_4,$12H_2O$ 1.28 $g.L^{-1}$, KH_2PO_4 0.48 $g.L^{-1}$, dihydrostreptomycin

sulfate 0.25 $g.L^{-1}$) at pH = 6. AX2 cells expressing a $LimE^{\Delta coil}$-GFP fusion protein (vector B12) (Diez, 2005) were grown in axenic medium supplemented with 20 µg/mL G418 (Sigma) in shaking suspensions. The plasmid was kindly provided by G. Gerisch.

D. discoideum cells were recovered by centrifugation (EPPENDORF 5415R, Hamburg, Germany) at 1000 x g, for 3 min at 4°C, washed once in SB and resuspended at 10^6 $cells.mL^{-1}$ in diluted buffer before use.

When used, latrunculin A was added in the culture medium at 3 µM for 5 min before centrifugation and washes. Cells were used immediately after the treatment.

The zeta potential of *D. discoideum* cells and of surface-carboxylated fluorescent polystyrene beads (diameter 1 µm) was measured using a ZETASIZER 1000 (Malvern Instruments, Malvern, UK) and was found to be - 17±3 mV and -56±5mV in SB respectively.

2.1.3 Preparation of surfaces

Borosilicate glass cover slips for microscopy were used after cleaning with ionic detergent, rinsing with ethanol and deionized water.

Gold and platinum surfaces were obtained by vacuum deposition of 5 nm titanium on borosilicate glass and then 3 nm of gold or platinum, respectively.

Silanization of glass cover slips was performed as follows:

- Cleaning with ionic detergent, rinsing with ethanol and deionized water.
- Immersing in 14.5 M NaOH for 5 min and washing with deionized water.
- Immersing in a 1% APTES solution in 5 mM acetic acid for 20 minutes under agitation and washing with deionized water.
- Curing at 100°C for 15 minutes.

Silanized glass cover slips stored for some time in contact with air were decarbonated by a 0.1 M KOH solution.

2.1.4 Experimental chambers

Plastic frame that constitutes the chamber of a Labtek (Nalge Nunc Int. US) (volume = 0.7 cm^3, surface = 0.5 cm^2) were used to construct experimental chambers on different substrates (single-chamber setup). For diffusion experiments, a double chamber

setup was built, consisting of a thin lower chamber separated from the upper chamber by a polycarbonate membrane (MILLIPORE TMTP01300, Molsheim, France) 20 microns thick and 5 microns pore diameter, 10% porosity (see fig. 2.1A and B). The height of the lower chamber, *e*, was built using several layers of double adhesive tape (260 microns thick PVC ribbon covered with polyacrylic glue, 3M; e = 260n, where *n* is the number of double adhesive tape layers), cut out at the required dimensions.

These experimental setups are schematized in Fig. 2.2.

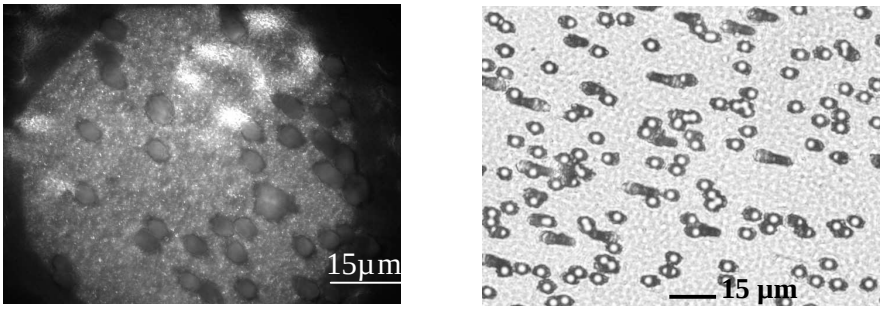

Fig. 2.1 Polycarbonate membrane images (**A**) RICM and (**B**) Phase Contrast. The 5-micron holes of the membrane can be seen.

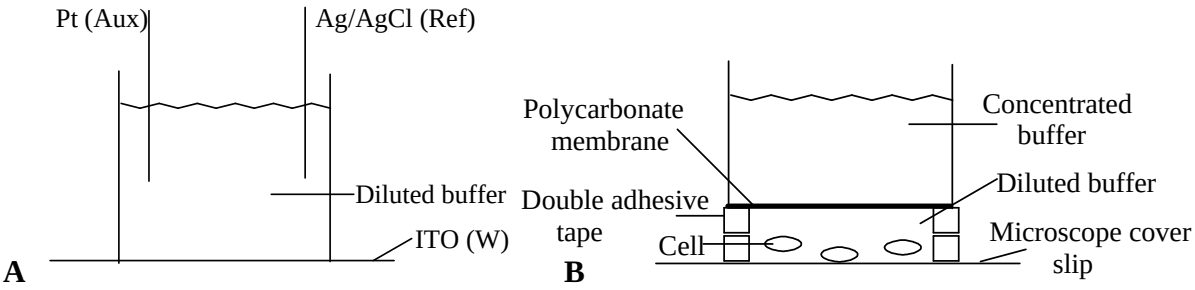

Fig. 2.2 (**A**) Single chamber and (**B**) double chamber setups. In (**A**) a three electrode experimental setup is shown: the platinum wire was the counter electrode (Aux), the ITO coated surface was used as the working one (W) and the reference was a Ag/AgCl pseudoelectrode (Ref.).

2.1.5 Electrochemical experiments

Transparent conducting surfaces were thin glass slides (0.145 and 0.175 mm thick) covered by Indium Tin Oxide (ITO, thickness 80 nm, resistance 20 ohms.cm) from PGO (Präzisions Glas & Optik Gmbh, Iserlohn, Germany). ITO belongs to the class of

transparent conductive materials with interesting optical and electrical proprieties (Laux, 1998).

For electrochemical experiments on gold or ITO coated surfaces, platinum and silver wires were attached in the upper chamber. The latter one was previously immersed in a ferric chloride aqueous solution, and used as a pseudo-reference electrode of Ag/AgCl type and named *Ref.* in the following. The platinum wire was the counter electrode and the ITO coated surface was used as the working one. We used a potentiostat (RADIOMETER DEA 332 Digital Electrochemical Analyzer controlled by VOLTALAB software, Villeurbanne, France) to carry out chronoamperometric and voltamperometric experiments.

In order to calibrate the electrochemical response of the ITO electrode with respect to local hexacyanoferrate concentrations, a 0.0 V/Ref. potential pulse (0.5 s) was applied, using the single chamber setup and the current response was measured as a function of known hexacyanoferrate concentrations.

In order to monitor the ionic diffusion kinetics in a double chamber setup, the lower chamber was first filled by a 0.5 M KNO_3 solution. 17 mM potassium hexacyanoferrate in 0.5 M KNO_3 was poured over the membrane. The concentration ratio between KNO_3 and $Fe(CN)_6^{3-}$ was 30 to avoid ionic migration of the hexacyanoferrate. At given times, a 0.0 V/Ref. potential pulse was applied for 0.5 s to the 50 nm gold surface and the current responses recorded to estimate the corresponding hexacyanoferrate concentration at the gold surface, using the calibration curve.

The diffusion coefficient, *D*, of $Fe(CN)_6^{3-}$ was determined by chronoamperometry (10 s) on a Pt flat disk surface using the Cottrell equation (Bard, 1980):

$$I(t) = nFSC_0 D^{0.5} (\pi t)^{-0.5} \qquad \text{Eq. 2.1}$$

where *n* is the number of exchanged electrons by the redox group (in this case n = 1), *F* the Faraday constant, *S* the Pt surface area and C_0 the initial concentration of $K_3Fe(CN)_6$.

By plotting *I* as a function of $t^{-0.5}$, we obtained a diffusion coefficient comprised between 0.9 and 1.05 10^{-5} cm^2 s^{-1} for $Fe(CN)_6^{3-}$ which corresponds to published value (Robinson, 1970).

Electrochemically induced cell adhesion was carried out in a one-chamber setup (Fig. 2.2A) fitted with the reference and counter electrodes using an ITO-coated surface as working electrode. Cells were introduced in 0.17 mM phosphate sucrose buffer. After sedimentation, a potential pulse was applied for a certain time. In the case when we applied 2.5 V/Ref. for 2 s, the integrated electrical charge was 0.1 mC, corresponding to the production of 1 nmole of protons (according to Faraday's law), if all the current corresponds to water oxidation.

Potential pulses were generated with a TTi 10 MHz pulse generator (THURBLY THANDAR INSTRUMENTS, Huntington, UK) using a square-shaped 5 V pulse for given pulse durations. This voltage was applied between the ITO surface and the platinum counter electrode and is equal to the measured voltage between the working electrode and the counter electrode in the three-electrode setup.

2.1.6 Mathematical simulation of ion diffusion in the double chamber setup

In order to compare the experimental evolution of concentration at the surface in the double chamber setup (Fig. 2.2B) with a rather simple mass transport description, we solved Fick's second law considering planar diffusion (Equation 2.2). MATLAB (The Math Works, Natick, MA) software was used to numerically solve equation 2.2 for D = 10^{-5} cm^2 s^{-1} and e = 520 μm, considering a constant 17 mM concentration at the top of the lower chamber (the upper chamber can be considered as an infinite reservoir) and no flux condition at the glass surface.

$$\frac{\partial C(x,t)}{\partial t} = D\frac{\partial^2 C(x,t)}{\partial x^2} \qquad \text{Eq. 2.2}$$

with the boundary conditions: C(0, t) = 17 mM and $\left.\frac{\partial C(x,t)}{\partial x}\right|_{x=e} = 0$

The formula for the calculation of the diffusion coefficient for strong electrolytes (D_s), for example $A_{\nu_1}^{z_1} B_{\nu_2}^{z_2}$, is given by the well known Nernst relation (Robert, C. W., 1987):

$$D_s = \frac{RT}{F^2} \cdot \frac{(\nu_1 + \nu_2) \cdot (\lambda_1^0 \cdot \lambda_2^0)}{\nu_1 \cdot z_1 \cdot (\lambda_1^0 + \lambda_2^0)} = 2.66 \cdot 10^{-7} \cdot \frac{(\nu_1 + \nu_2) \cdot (\lambda_1^0 \cdot \lambda_2^0)}{\nu_1 \cdot z_1 \cdot (\lambda_1^0 + \lambda_2^0)}$$ at T = 298 K; Eq. 2.3

One denotes z_i and ν_i the ionic charge and its coefficient, respectively; λ_i^0 (in $cm^2 \cdot S/mol$) is the equivalent ionic conductivity at infinite dilution at 298 K.

For example, $D_{CaCl_2} = 1.33 \cdot 10^{-5} cm^2/s$, $D_{KH_2PO_4} = 1.21 \cdot 10^{-5}\ cm^2/s$

The diffusion coefficient of a single ion can be calculated regardless of the counter ion:

$$D_{ion} = \frac{RT}{F^2} \cdot \frac{\lambda^0}{z} = 2.66 \cdot 10^{-7} \cdot \frac{\lambda^0}{z} \qquad D_{Fe(CN)_6^{3-}} = 0.98 \cdot 10^{-5} cm^2/s$$ Eq. 2.4

This value is in perfect agreement with the experimental value (see Materials and Methods) and with the literature (Bernard M., 1996).

For a mixture of salts, it is very difficult to calculate the average diffusion coefficient. For simplicity, the main contribution is attributed to the predominant salt, even though, in reality, there is a pair wise redistribution of negative and positive ions among the diffusing salts. In SB (Sörensen buffer or phosphate buffer), KH_2PO_4 is the predominant salt (14.68 mM).

2.1.7 Mathematical simulation of the pH in solution at the conductive surface

Concentration of the protons formed during an electrical pulse application is calculated using Comsol Multiphysics Modeling and Simulation software (EULA, COMSOL AB). Comsol is a finite element analysis and solver software package for various physics and engineering applications, especially coupled phenomena or multiphysics. The Chemical Engineering Module incorporates application models for the field of transport phenomena including ionic transport and multi component diffusion. The proton concentration in the ITO surface vicinity (the experimental setup is shown in Fig. 2.2A) is calculated, taking into account water electrolysis (the intensity of the current, the pulse application time) and, in the same time, its diffusion (the proton diffusion coefficient is $D_{H+} = 10^{-4}\ cm^2\ s^{-1}$) (Eq. 2.5). The proton migration is not considered, since the electrolyte concentration is higher than the proton concentration. Thus, we considered that the major contribution to the migration transport derives from electrolyte ions.

When the proton production is stopped, one considers only its diffusion in the bulk solution, increasing the pH close to the surface.

$$\frac{\partial C_{H+}(x,t)}{\partial t} = D_{H+}\frac{\partial^2 C_{H+}(x,t)}{\partial x^2} \text{ and } C_{H+}(0,t_s) = \frac{I \cdot t_s}{F \cdot S \cdot \Delta x} \qquad \text{Eq.2.5}$$

with boundary condition: $C_{H+}(\infty, t) = 0$. Where *F* is the Faraday constant, *S* the ITO surface area, *I* is the applied or measured intensity, t_s is the time of current application.

For an intensity of $4*10^{-5}$ A applied during 50 s, the concentration profile versus time is:

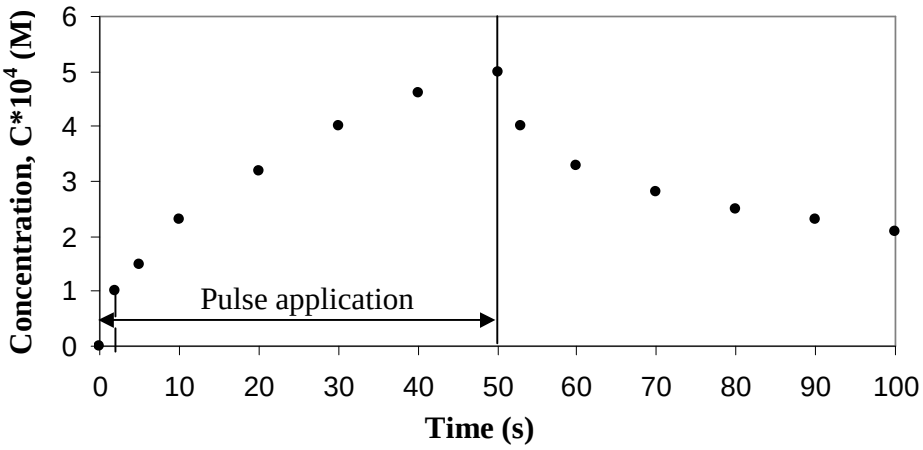

Fig 2.3 Theoretical proton concentration profile at the surface during and after a 50 s pulse

After applying the same current for 2 s, the pH is decreasing to 4 (see Fig. 2.3). For shorter current pulse, the pH increase is almost linear with the pulse duration. For a longer time application, the cell activity could be affected. In addition, the surface acidification was confirmed with a pH-sensitive dye.

2.1.8 Optical observation of cell spreading

To monitor the presence and spreading of *D. discoideum* cells, we used an inverted microscope (OLYMPUS IX71, Rungis, France, Fig. 2.4A) illuminated with a halogen lamp (transmitted light) and a mercury lamp (reflected light). Cells were imaged with an oil-immersed objective (60X magnification, 1.25 numerical aperture) by phase contrast (PC) and Reflection Interference Contrast Microscopy (RICM). For RICM, a green filter selected the 546 nm Hg emission peak and a semi-reflecting plate was set at

45° of the optical axis to illuminate the sample. Still images and movies (15 frames per s) were acquired by means of an Olympus DP30 CCD camera (Photonic Science, UK). For a better presentation in this thesis, some images were treated by transposing individual cells on a more clear background.

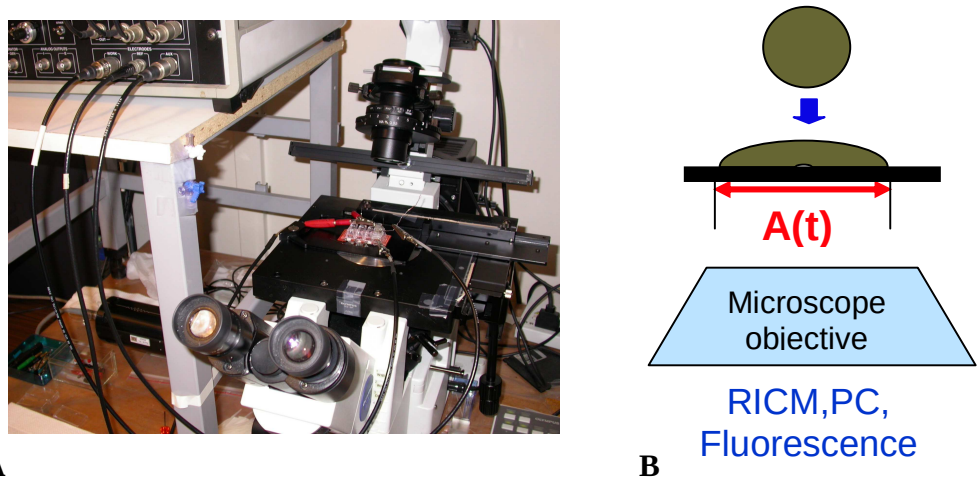

A **B**

Fig. 2.4 (**A**) photo in the laboratory of the experimental setup and (**B**) an explicative scheme for the observation of cell spreading by RICM, Phase Contrast (PC) or fluorescence.

RICM allows the analysis of living as well as fixed cells attached to a plain surface using reflection-type microscopes. The resulting image is determined by the relative reflectivity (RI) at different areas of the cell, and by interferences of the light reflected at different boundaries (Fig. 2.5, Bereiter-Han, 1979).

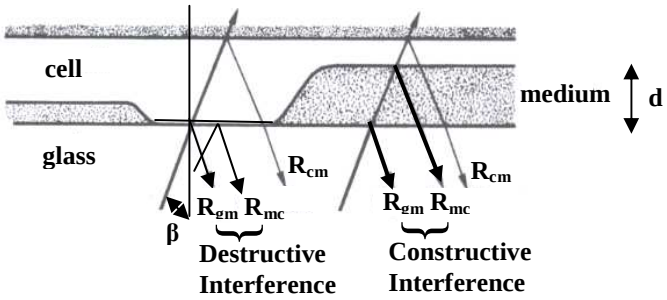

Fig 2.5 Schematic representation of the main reflecting interfaces in a cell preparation on a glass surface. The black arrows indicate the incident light beams and the reflected light beams with the relative intensity **R**. Suffixes indicate the optical media forming the interface (g, glass; c, cell; m, medium). The phase of $\mathbf{R_{gm}}$ is shifted for λ/2 at the reflecting surface. $\mathbf{R_{cm}}$ is normally not visible in thick cells. *β* is the angle of incidence of the illuminating beam and *d* stands for the geometrical distance between cell membrane and glass surface.

RICM is used to view cells in culture adhering to a plane glass surface. Extremely thin layers of protein or cytoplasm can be detected on a glass surface. Assuming that the

cytoplasm is optically homogeneous, three optical interfaces may occur (Fig. 2.5): glass/culture medium (gm), medium/cell (mc) or cell/medium (cm) (two thin layers on top of the glass). For Dictyostelium discoideum, which is a thick cell (average of 10 µm in diameter), R_{cm} is insignificant.

Light beams reflected from the various interfaces interfere with each other. The resulting intensities depend on the differences in optical path lengths (Δ) and RI at the boundaries. The optical path difference (Δ) between two reflected wave fronts is related to the geometrical distance (d), the refractive index (n) and the angle of incidence of the illuminating beam (for normal incidence, β = 0 and cosβ = 1) by the following equation:

$$\Delta = 2nd / \cos\beta \qquad \text{Eq. 2.6}$$

In the case of light reflection at an optically denser medium, the interference of the reflected light beams can occur. The calculated value of the intensity of the interfered light beam ($I_{interference}$) corresponds to the product of the amplitude ($E_{interference}$ or E) and its conjugated complex value ($E^*_{interference}$). Considering only two reflected wave fronts (R_{gm} and R_{mc}) one obtains:

$$E_{interfernce} = E_{gm} + E_{mc} = \sqrt{I_0} R_{gm} e^{i\frac{\lambda}{2}} + \sqrt{I_0} R_{mc} e^{i\Delta}, \qquad \text{Eq. 2.7}$$

where I_0 is the intensity of the incident light beam. The phase of R_{gm} is shifted for $\lambda/2$ at the reflecting glass surface.

$$I_{interference} = E \cdot E^* = I_0[R_{gm}^2 + R_{mc}^2 + 2R_{gm}R_{mc}\cos(\Delta - \frac{\lambda}{2})] \qquad \text{Eq. 2.8}$$

It results that one obtains a maximum intensity, relative to the incident light intensity (constructive interference), if:

$$\cos(\Delta - \frac{\lambda}{2}) = \cos(\frac{2nd}{\cos\beta} - \frac{\lambda}{2}) = 1 \quad \Leftrightarrow \quad \frac{2nd}{\cos\beta} - \frac{\lambda}{2} = 2p\pi \cdot \frac{\lambda}{2\pi}$$
$$\Rightarrow \quad d = \frac{\lambda}{4} \cdot \frac{(2p+1)\cdot\cos\beta}{n} \qquad \text{Eq.2.9}$$

where $p \in N$.

When $\cos(\Delta - \frac{\lambda}{2}) = -1$ (destructive interference), it results:

$$d = \frac{\lambda}{4} \cdot \frac{(2p)\cos\beta}{n} \qquad \text{Eq.2.10}$$

In our experiments wavelength of the incident beam light is λ = 546 nm, the medium refractive index is considered n = 1.33 and the angle of incidence, β, is very close to 0 degrees. Regarding the equations 2.9 and 2.10, we obtain first maximum interference intensity (constructive interference) for $d \approx 100$ nm and the first minimum interference intensity (destructive interference) for $d = 0$ (putting $p = 0$).

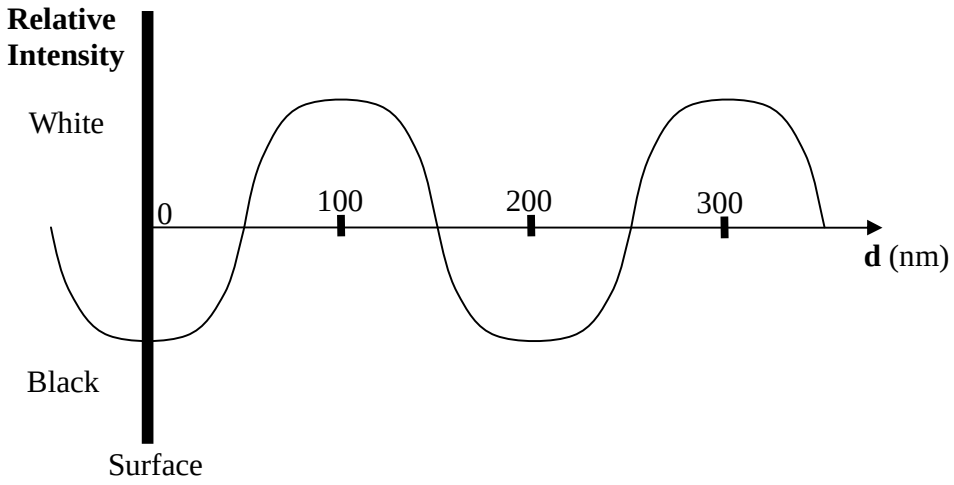

Fig 2.6 Schematic representation of interference contrast intensity relative to the background versus the geometrical distance between cell membrane and surface (d).

Thus, in areas where the cells are intimately attached with the glass, we can distinguish zones of close contact of the cells to the glass, which appear dark gray. Additionally, focal contacts are almost black (destructive interference, d = 0). The bright or white zones correspond to a maximum interference intensity (constructive interference, $d \approx 100 \cdot (2p+1)$ nm) (Fig. 2.6). Similar maximum interference intensities were obtained when transparent surfaces were thin glass slides (0.145 and 0.175 mm thick) covered by Indium Tin Oxide (ITO, thickness 80 nm).

Also, for a thin cell, at an angle of incidence of 30 degrees and with orange light (λ = 589 nm), cytoplasm with a refractive index of 1.4, a geometrical difference d of 100 nm is sufficient for maximum interference contrast (from maximum brightness to a dark contrast or viceversa, see also the Fig. 2.7). The brightness does not change considerably by changing either the wavelength or the angle of illumination but change sharply with d and n. RICM allows following very small changes and differences in distance between cell and surface (Bereiter-Han, 1998).

The refractive medium for SB and diluted buffer was measured with an Abbé refractometer: n = 1.333 for SB and n = 1.334 for diluted buffer solution containing sucrose.

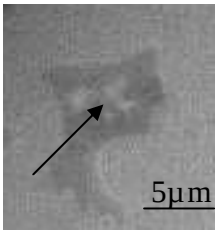

Fig 2.7 RICM image of a Dictyostelium discoideum cell spread on a glass; the bright zone indicates a membrane part that is at least at 100 nm distance from the substrate.

A *D. discoideum* cell was considered as attached when a dark contact area larger than 4 μm^2 lasted for more than 10 s and enlarged with time. Cells were considered fully spread when 90% of the maximum contact area was reached.

2.1.9 Analysis of cell spreading kinetics

Using the Image Pro Plus software (IPP, MediaCybernetics, Bethesda, MD, USA), RICM images were sub-sampled at 1 image per 1.2 seconds, the background was subtracted and flattened and the noise filtered. This generates a black and white movie showing the changes in contact area with time, where cell-surface contact areas appear white (pixel value 255) over a dark background (pixel value 0). White areas are quantified and plotted as a function of time, giving the spreading kinetics. Individual spreading kinetics are adjusted by the equation derived by Chamaraux *et al.* (Chamaroux, 2005):

$$A(t) = A_{max} \tanh(\alpha t) \qquad \text{Eq. 2.11}$$

where A_{max} is the maximum cell-surface contact area, α the inverse of the characteristic spreading time and the initial contact time is set at t = 0. In this model, the initial spreading slope is αA_{max}.

2.1.10 Analysis of LimE-GFP fluorescence

Epifluorescence images were obtained using an appropriate filter set to match Green Fluorescent Protein (GFP) characteristic excitation and emission spectra (λex =

481 nm, λem = 507 nm). GFP fluorescence was selected with a BGW cube (Olympus) and supplementary BG18 and BG28 excitation and emission filters (Melles Griot).

Green fluorescent protein (GFP) was first purified from *Aequorea victoria* in 1992 (Shimomura, 1962). GFP is a compact and globular protein composed of 238 amino acids (27 kDa) and has dimensions of 2.4 per 4.2 nm (Ormö, 1996). 30 years after its isolation, Douglas Prasher had the idea to use GFP like target in order to monitor the production and localization of a protein of interest. The gene of GFP was cloned in 1992 (Prasher, 1992). The first successful genetic expression of GFP in E. coli was realized in 1994 (Chalfie, 1994). The cells exhibit bright green fluorescence when exposed to blue light. The protein gets its fluorescent properties by an autocatalytic mechanism of fluorophore formation (Chalfie, 1994).

In our study we used a fluorescent version of the LimE protein (a GFP fusion construct with a fragment of LimE, $LimE^{\Delta coil}$-GFP (Schneider, 2003) which, will be noted simplest LimE-GFP) to visualize and measure the actin dynamics in *Dictyostelium*.

In our experiments, to quantify fluorescence variation with time, a threshold is set to identify actin polymerization active zones inside the cell. The threshold *T* is defined by the following formula: T = B+ 2(C-B) where *B* corresponds to background fluorescence outside the cell and *C* corresponds to the cytoplasmic fluorescence. An active zone is made of pixels in which significant fluorescence events occur over more than 3 consecutive frames and attain a minimum of 4 pixels (~1μm^2). The signal recorded is obtained by integrating the fluorescence over all the active zone. The time at which local fluorescence attains a maximum (peak values) was determined. Image Pro Plus software was used to quantify fluorescence.

2.2 Electrical phenomenon at the interface

2.2.1 Brief description of the electrical double layer

An electrode at which no charge transfer can occur across the metal-solution interface, regardless of the potential imposed by an outside source of voltage, is called an ideal polarizable electrode (IPE, for example, a mercury electrode in contact with a

deaerated KCl solution). Since charge cannot cross the IPE interface when the potential across it is changed, the behavior of the electrode-solution interface is analogous to that of a capacitor. In addition, a surface of an oxide material may be charged by dissociation of surface groups (for example, the silanol groups of glass surface) or by adsorption of charged ions or molecules from surrounding solution.

The solution side of the double layer is thought to be made up of several "layers". The one closest to the surface of the material (electrode or oxide material), the inner layer, contains solvent molecules and sometimes other species (ions or molecules) that are said to be specifically adsorbed (see Fig. 2.8). This inner layer is also called the compact, Helmholtz or Stern layer. The locus of the electrical centers of the specifically adsorbed ions is called the inner Helmholtz plane (IHP), which is at a distance x_1. The total charge density from specifically adsorbed ions in this inner layer is σ^i ($\mu C/cm^2$). Solvated ions can approach the solid material (M) only to a distance x_2. The locus of centers of these nearest solvated ions is called the outer Helmholtz plane (OHP).

The interaction of the solvated ions with the charged metal (or ionized surface groups) involves only long-range electrostatic forces, so that their interaction is essentially independent of the chemical properties of the ions. These ions are said to be nonspecifically adsorbed.

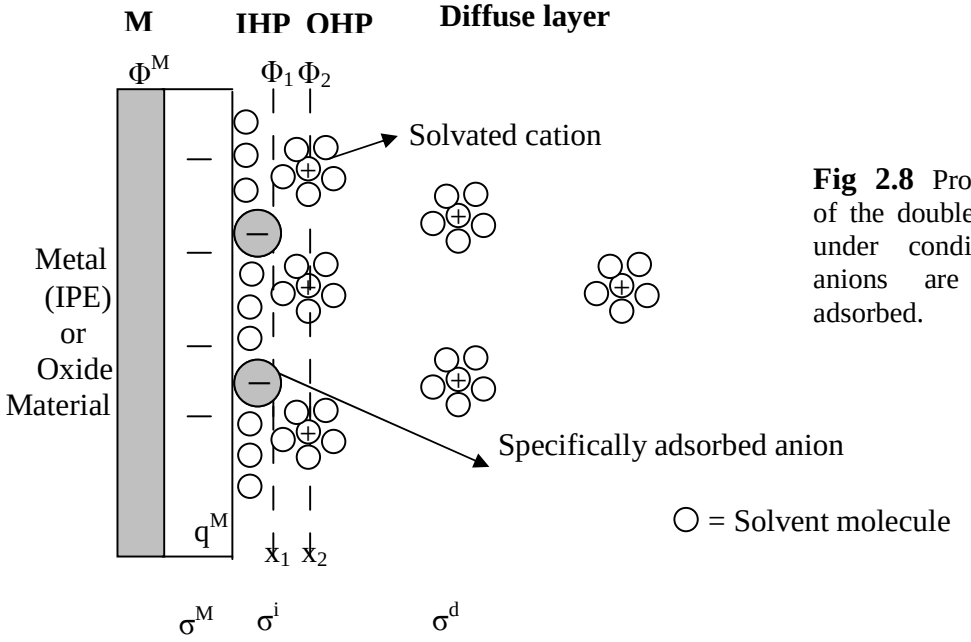

Fig 2.8 Proposed model of the double-layer region under conditions where anions are specifically adsorbed.

Because of thermal agitation in the solution, the nonspecifically adsorbed ions are distributed in a three-dimensional region called the diffuse layer, which extends from the OHP into the bulk of the solution (Bard, 1980). The excess charge density in the diffuse layer is σ^d, hence the total excess charge density on the solution side of the double layer, σ^S, is given by:

$$\sigma^S = \sigma^i + \sigma^d = -\sigma^M \qquad \text{Eq. 2.12}$$

The thickness of the diffuse layer depends on the total ionic concentration in the solution. For example for concentrations greater than 10^{-2} M (the Debye distance for a 1:1 electrolyte at 10^{-2} M is ~3 nm), the thickness is less than 10 nm.

2.2.2 The Gouy-Chapman Theory

Gouy and Chapman independently proposed the idea of a diffuse layer and offered a statistical mechanical approach to describe it. They considered the solution as being subdivided into laminae, parallel to the electrode, of thickness *dx*, starting from the electrode surface (x = 0). All these laminae are in thermal equilibrium with each other. However, the ions of every species *i* are not at the same energy in the various laminae, because the electrostatic potential Φ varies (its magnitude decreases from the electrode surface through the bulk solution). The laminae can be regarded as energy states with equivalent degeneracies; hence, the concentrations of species in two laminae have a ratio determined by a Boltzmann factor. If the reference is taken at the laminae far from the electrode, when every ion is at its bulk concentration n_i^0, then the population in any other laminae is:

$$n_i = n_i^0 \exp\left(\frac{-z_i e\Phi}{kT}\right) \qquad \text{and the charge density is } \rho(x) = \sum_i n_i z_i e \qquad \text{Eq. 2.13}$$

where Φ is measured with respect to the bulk solution. The other quantities are the electron charge, *e*, the Boltzmann constant, *k*, the absolute temperature, *T*, the (signed) charge, z_i of an ion *i* and ρ(x), the total charge per unit in any lamina.

From electrostatics, we know that ρ(x) is related to the potential at distance *x* by the Poisson equation:

$$\rho(x) = -\varepsilon\varepsilon_0 \frac{d^2\Phi}{dx^2} \qquad \text{Eq. 2.14}$$

which yields the Poisson-Boltzmann equation:

$$\frac{d^2\Phi}{dx^2} = -\frac{e}{\varepsilon\varepsilon_0}\sum_i n_i^0 z_i \exp\left(\frac{-z_i e\Phi}{kT}\right) \qquad \text{Eq. 2.15}$$

Equation 2.15 is treated by:

$$\frac{d^2\Phi}{dx^2} = \frac{1}{2}\frac{d}{d\Phi}\left(\frac{d\Phi}{dx}\right)^2 \qquad \text{Eq. 2.16}$$

$$\text{hence, } d\left(\frac{d\Phi}{dx}\right)^2 = -\frac{2e}{\varepsilon\varepsilon_0}\sum_i n_i^0 z_i \exp\left(\frac{-z_i e\Phi}{kT}\right)d\Phi \qquad \text{Eq. 2.17}$$

$$\text{Integration gives: } \left(\frac{d\Phi}{dx}\right)^2 = \frac{2kT}{\varepsilon\varepsilon_0}\sum_i n_i^0 \exp\left(\frac{-z_i e\Phi}{kT}\right) + C \qquad \text{Eq. 2.18}$$

and the constant *C* is evaluated by recognizing that at distance far from the electrode $\Phi = 0$ and $d\Phi/dx = 0$. Thus,

$$\left(\frac{d\Phi}{dx}\right)^2 = \frac{2kT}{\varepsilon\varepsilon_0}\sum_i\left[n_i^0 \exp\left(\frac{-z_i e\Phi}{kT}\right) - 1\right] \qquad \text{Eq. 2.19}$$

For a symmetrical electrolyte (z:z electrolyte) we obtain the following differential equation:

$$\frac{d\Phi}{dx} = -\left(\frac{8kTn^0}{\varepsilon\varepsilon_0}\right)^{1/2} \sinh\left(\frac{ze\Phi}{2kT}\right) \qquad \text{Eq. 2.20}$$

The equation 2.20 can be rearranged and integrated in the following manner:

$$\int_{\Phi_0}^{\Phi} \frac{d\Phi}{\sinh(ze\Phi/2kT)} = -\left(\frac{8kTn^0}{\varepsilon\varepsilon_0}\right)^{1/2}\int_0^x dx \qquad \text{Eq. 2.21}$$

where Φ_0 is the potential at x = 0 relative to the electrode surface. In the other words, Φ_0 is the potential drop across the diffuse layer. The result is:

$$\frac{2kT}{ze}\ln\left[\frac{\tanh(ze\Phi/4kT)}{\tanh(ze\Phi_0/4kT)}\right] = -\left(\frac{8kTn^0}{\varepsilon\varepsilon_0}\right)^{1/2} x \qquad \text{Eq. 2.22}$$

We obtain the potential profile in the diffuse layer:

$$\tanh(ze\Phi / 4kT) = \tanh(ze\Phi_0 / 4kT)\, e^{-\kappa x} \qquad \text{Eq. 2.23}$$

$$\kappa = \left(\frac{2n^0 z^2 e^2}{\varepsilon\varepsilon_0 kT} \right)^{1/2} \text{; for } \varepsilon = 78.49 \text{ at } 25^oC \ \kappa = 3.29 \cdot 10^7 \ z \ C^{1/2}, \qquad \text{Eq. 2.24}$$

where *C* is the bulk z:z electrolyte concentration (M) and κ is given in cm^{-1}. 1/κ is the so-called Debye distance and is of the order of 3 nm for 10^{-2} M 1:1 electrolyte at 25ºC. For a 1:1 electrolyte, the Debye distance as a function of electrolyte concentration, is:

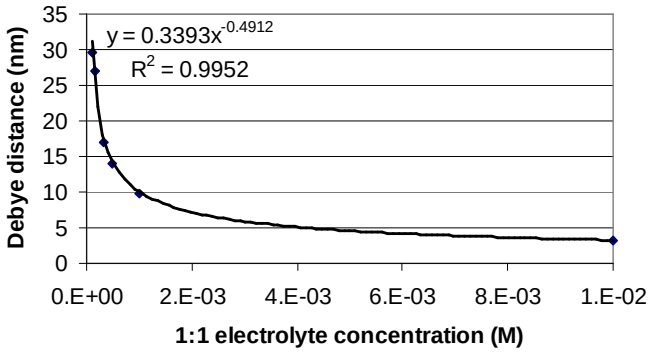

Fig. 2.9 Debye distance as a function of 1:1 electrolyte concentration.

In fact, the form is exponential in the limit of small Φ_0. If $\Phi_0 < 50/z$ mV at 25ºC, then we can approximate that: $\Phi = \Phi_0 e^{-\kappa x}$ Eq. 2.25

Suppose we now imagine a Gaussian surface in the shape of a box placed in our system (Fig. 2.10) with one end at the interface, the sides perpendicular to this end and extend far enough into the solution where the field strength dΦ/dx is essentially zero.

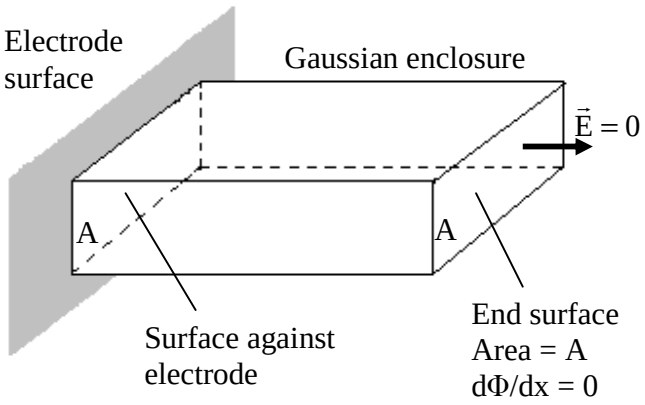

Fig. 2.10 A Gaussian box enclosing the charge in the diffuse layer contacting an area, A, of the electrode surface

The box therefore contains all the charge in the diffuse layer contacting the portion of the electrode surface adjacent to the end (charge conservation). From the Gauss law, this charge is:

$$q = \varepsilon\varepsilon_0 \oint_{surface} \vec{E} \cdot \vec{dS} = \varepsilon\varepsilon_0 \left(\frac{d\Phi}{dx} \right)_{x=0} \int_{surface}^{end} dS \qquad \text{Eq. 2.26}$$

Substituting from eq. 2.20 and recognizing that q/A is the solution phase charge density σ^S, we obtain the relation between charge density (σ^M) and Φ_0:

$$\sigma^M = -\sigma^S = (8kT\varepsilon\varepsilon_0 n^0)^{1/2} \sinh\left(\frac{ze\Phi_0}{2kT} \right) \approx 11.7 \cdot C^{1/2} \cdot \sinh(19.5z\Phi_0), \quad \text{Eq. 2.27}$$

where *C* is in mol/L and σ^M in $\mu C/cm^2$.

2.2.3 Tacking into account the finite size of electrolyte ions: the Stern modifications

The partial success of the Gouy-Chapman theory suggests that it has elements of truth, but also, indicates major defects. One of those defects is related to the finite size of the ions in an electrolyte.

For example, there is an unlimited differential capacitance with Φ_0 in the Gouy-Chapman model because the ions are considered as point charges that can closely approach the surface. Therefore, at high polarization, the effective separation distance between the metallic and solution phase charge zones decreases continuously towards zero. This view is not realistic. The ions have a finite size and cannot approach the surface any closer than the ionic radius. If they remain solvated, the thickness of the primary solution sheath would be added to that radius. Still another increment might be necessary to account for a layer of solvent on the electrode surface. In other words, we can envision a plane of closest approach for the centers of the ions at some distance x_2.

The Poisson-Boltzmann equation, and its solutions, still apply at distance $x \geq x_2$:

$$\tanh(ze\Phi / 4kT) = \tanh(ze\Phi_2 / 4kT)\, e^{-\kappa(x - x_2)} \qquad \text{Eq. 2.28}$$

The plane at distance x_2 from the surface electrode is an important concept and is called the outer Helmholtz plane (OHP, see Fig. 2.11 and 2.8). Between the electrode (x = 0) and OHP, there is no charge transport, therefore the potential Φ decreases linearly. The slope is given by Eq. 2.20, tacking $x = x_2$:

$$\left(\frac{d\Phi}{dx}\right)_{x=x_2} = -\left(\frac{8kTn^0}{\varepsilon\varepsilon_0}\right)^{1/2} \sinh\left(\frac{ze\Phi_2}{2kT}\right) \Rightarrow \Phi_0 = \Phi_2 - \left(\frac{d\Phi}{dx}\right)_{x=x_2} x_2 \quad \text{Eq.2.29}$$

resulting the total potential drop across the double layer (Φ_0).

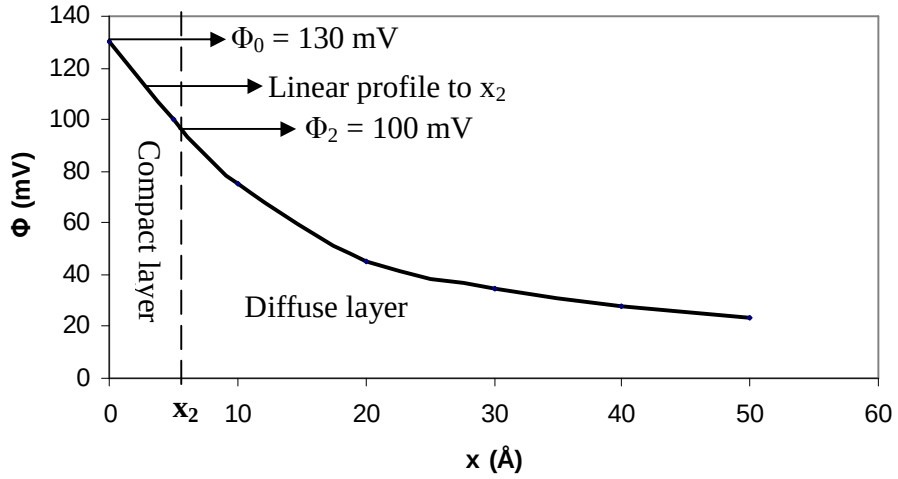

Fig 2.11 Potential profile through the solution side of the double layer, according to the Gouy-Chapman-Stern theory (GCS theory). Calculated from eq. 2.22 for 10^{-2} M 1:1 electrolyte in water at 25ºC (Bard, 1980).

From the streaming potential measurements, the shear plane, corresponding to the zeta potential, is very close to the OHP. Therefore, we can approximate the surface density charge (considering also the specifically adsorbed ions in the inner layer, if they exist) function of the zeta potential (ζ):

$$\sigma^M + \sigma^i = (8kT\varepsilon\varepsilon_0 n^0)^{1/2} \sinh\left(\frac{ze\Phi_2}{2kT}\right) = (8kT\varepsilon\varepsilon_0 n^0)^{1/2} \sinh\left(\frac{ze\zeta}{2kT}\right) \quad \text{Eq. 2.30}$$

$$\approx 11.7 \cdot C^{1/2} \cdot \sinh(19.5z\zeta)$$

2.2.4 Zeta potential measurements of surfaces

Zeta potentials were measured with a SurPass Anton Paar Electrokinetic Analyzer with the help of a SurPASS clamping cell (Fig. 2.12A). Polymethyl Methacrylate (PMMA-$(C_5O_2H_8)_n$) is the reference material in this method.

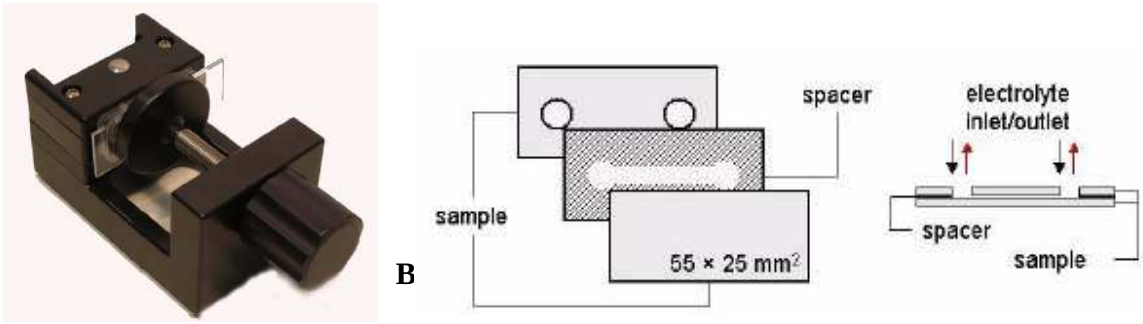

Fig. 2.12 A. SurPASS Clamping Cell with sample (glass slide) mounted; **B.** Schematic drawing of the sample stack in the SurPASS Clamping Cell (height: h; length: l and width: L)

A streaming current and streaming potential are an electric current and potential appearing when an electrolyte is driven by a pressure gradient ($P_1>P_2$; $\Delta P = P_2 - P_1<0$) through a channel or porous plug with charged walls (Fig. 2.12B). Adjacent to the channel walls, the charge-neutrality of the liquid is violated due to the presence of an electrical double layer: a thin layer of counterions is attracted by the charged surface. The transport of these counterions along with the pressure-driven fluid flow gives rise to a net charge transport: the streaming current (Fig. 2.13).

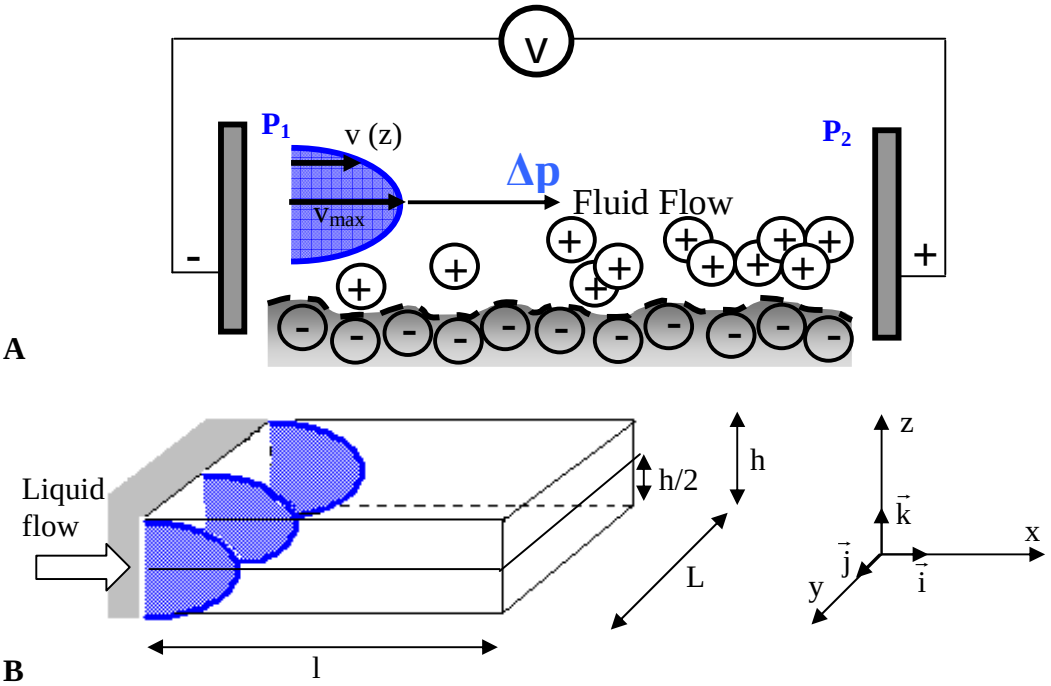

Fig. 2.13 A. Mechanism of streaming potential arising ($P_1>P_2$). **B**. Stationary flow in a clamping cell with dimensions: height (h), length (l) and width (L); h << L and h << l.

In order to find the streaming current and the streaming potential that arise when an electrolyte is driven by a pressure gradient through a space delimitated by two parallel planar surfaces, we employed the Navier-Stokes equation for the incompressible liquids and the Gouy-Chapman-Stern theory.

$$\rho\frac{\partial\vec{v}}{\partial t}+\rho\vec{v}\cdot\vec{\nabla}\vec{v}=-\vec{\nabla}P+\eta\Delta\vec{v} \qquad \text{Eq. 2.31}$$

where *v* stands for local speed of the fluid, ρ is the liquid density, η represents the dynamic viscosity of the liquid and P is the pressure.

One considers that the liquid flowing occurs in a stationary regime ($\frac{\partial\vec{v}}{\partial t}=0$) and only along the *x* axis between the two planar surfaces, in the other words the vector $\vec{v}$ is parallel with *x* axis: $\vec{v}(\vec{r})=v(z)\cdot\vec{i}$ (the height, *h* is very small in comparison with length and width). Thus, the divergence of speed vector variation is not zero only along *z* axis. It results the scalar product:

$$\nabla\vec{v}=\frac{\partial}{\partial x}\vec{i}\cdot v(z)\vec{i}+\frac{\partial}{\partial y}\vec{j}\cdot v(z)\vec{i}+\frac{\partial}{\partial z}\vec{i}\cdot v(z)\vec{k}=\frac{\partial v(z)}{\partial x}=0 \qquad \text{Eq. 2.32}$$

The Navier-Stokes equation becomes:

$$\eta\frac{\partial^2 v}{\partial z^2}=\frac{dP}{dx} \qquad \text{Eq. 2.33}$$

Tacking as reference the lower planar surface and considering that in vicinity of the walls the local speed of the liquid is null (v(0) = v(h) = 0, and for z = h/2 one has the maximum speed, v_{max}, (see Fig. 2.13), the speed has the following profile:

$$v(z)=k\cdot z(h-z) \qquad \text{Eq. 2.34}$$

where *k* is a constant which is found relaying the speed with the rate of fluid flow (*D*), which can be very easily experimentally determined:

$$D=\iint_{surface}\vec{v}\cdot d\vec{S}=\iint_{surface}v(z)\cdot dz\cdot dy=2kL\int_0^{h/2}z(h-z)=\frac{kLh^3}{6}$$
$$\Rightarrow\quad k=\frac{6D}{Lh^3}\quad\text{and}\quad v(z)=\frac{6D}{Lh^3}z(h-z) \qquad \text{Eq. 2.35}$$

Replacing the expression of *v* in Eq. 2. 33, one obtains:

$$-\frac{12\eta D}{Lh^3}\cdot dx = dP \Rightarrow -\frac{12\eta D}{Lh^3}\cdot \int_0^l dx = \int_{P_1}^{P_2} dP \Leftrightarrow -\frac{12\eta D\cdot l}{Lh^3} = \Delta P$$
$$\Rightarrow D = -\frac{\Delta P\cdot Lh^3}{12\eta\cdot l} \qquad \text{Eq. 2.36}$$

Replacing the expression of *D* from eq. 2.36 in Eq. 2.36 we get the local speed function of pressure difference:

$$v(z) = \frac{-\Delta P}{2\eta l}\cdot z(h-z) = \frac{|\Delta P|}{2\eta l}\cdot z(h-z) \qquad \text{Eq. 2.37}$$

Adjacent to the channel walls, the charge-neutrality of the liquid is violated due to the presence of an electrical double layer (see Gouy-Chapman-Stern theory): a thin layer of counterions is attracted by the charged surface. The transport of these counterions along with the pressure-driven fluid flow gives rise to a net charge transport, the streaming current (we note I_{str} equivalent of ions transported in time, for one surface):

$$I_{str} = \int_0^L \int_{z_2}^h \rho(z)\cdot v(z)\cdot dzdy = \frac{-\Delta P\cdot L}{2\eta l}\int_{z_2}^h \rho(z)\cdot z(h-z)dz \qquad \text{Eq. 2.38}$$

where z_2 is the outer Helmholtz plane coordinate and $\rho(z)$ is the charge density at distance z_2 from the surface. Considering that the thin layer of counterions is much smaller than the height of the chamber, we can approximate that $h\text{-}z \cong h$. It results:

$$I_{str} = \frac{-\Delta P\cdot Lh}{2\eta l}\int_{z_2}^h \rho(z)\cdot z\cdot dz \qquad \text{Eq. 2.39}$$

Tacking in account the Equation 2.14, we have:

$$I_{str} = \frac{-\Delta P\cdot Lh}{2\eta l}\int_{z_2}^h -\varepsilon\varepsilon_0\frac{d^2\Phi}{dz^2}\cdot z\cdot dz = \frac{\Delta P\cdot Lh}{2\eta l}\varepsilon\varepsilon_0\left(z\cdot\frac{d\Phi}{dz}\Big|_{z_2}^h - \int_{z_2}^h \frac{d\Phi}{dz}dz\right)$$
$$I_{str} = \frac{\Delta P\cdot Lh}{2\eta l}\varepsilon\varepsilon_0\left(h\cdot\left(\frac{d\Phi}{dz}\right)_{z=h} - z_2\cdot\left(\frac{d\Phi}{dz}\right)_{z=z_2} - \Phi(h) + \Phi(z_2)\right) \qquad \text{Eq. 2.40}$$

Knowing that $\Phi(h) = (d\Phi/dz)_{z=h} = 0$ and that the potential drop across the compact layer multiplied with its width, is negligible, we get:

$$I_{str} = \frac{\Delta P\cdot Lh}{2\eta l}\varepsilon\varepsilon_0\Phi(z_2) = \frac{\Delta P\cdot Lh}{2\eta l}\varepsilon\varepsilon_0\zeta \qquad \text{Eq. 2.41}$$

The tension that has to be applied for streaming current annulment, (the positive electrode-fig. 2.13-is placed against the fluid flow), considering that both surfaces are sources of counterions, is:

$$U_{str} = 2I_{str} \cdot R = 2 \cdot \frac{\Delta P \cdot Lh}{2\eta l} \varepsilon\varepsilon_0 \zeta \cdot \frac{l}{Lh \cdot K_L} = \frac{\varepsilon\varepsilon_0 \zeta}{\eta K_L} \cdot \Delta P \qquad \text{Eq. 2.42}$$

where U_{str} is streaming potential at zero net current conditions (V), R is the resistance of the bulk liquid (Ω), K_L is specific conductivity of the bulk liquid ($S \cdot m^{-1}$), ΔP is the pressure difference (Pa) and ζ stands as zeta potential (V).

Equation 2.42 (Helmoltz-Smoluchowski equation (Delgado, 2005)) is the basis of the experimental determination of zeta potential (see subchapter **2.2.7**).

2.2.5 Surface charge density and point of zero charge

When a solid is immersed in a polar solvent or an electrolyte solution, a surface charge develops through one or more of the following mechanisms:

1. Preferential adsorption of ions
2. Dissociation of surface charged species
3. Isomorphic substitution of ions
4. Accumulation or depletion of electrons near the surface
5. Physical adsorption of charged species onto the surface.

For a given solid surface in a given liquid medium, a fixed surface electrical charge density or electrode potential, *E*, will be established, which is given by the Nernst equation:

$$E = E_o + (R_g T/n_i F) \ln a_i \qquad \text{Eq. 2.43}$$

where E_o is the standard electrode potential at 1 M concentration of ions *i*, a_i is the chemical activity of specie i, n_i is the valence state of ions, R_g is the gas constant, *T* is the temperature, and *F* is the Faraday constant. Equation 2.43 clearly indicates that the surface potential of a solid varies with the concentration of the ions in the surrounding solution, and can be either positive or negative. The focus of the discussion here will be on non-conductive materials or dielectrics, more specifically on oxides.

The surface charge in oxides is mainly derived from preferential dissolution or deposition of ions, usually, by a chemical equilibrium. Ions physically adsorbed on the

solid surface determine the surface charge, and thus are referred to as charge determining ions, also known as co-ions.

The equilibrium determined by the proton concentration is as follows:

$$R-OH \Leftrightarrow R-O^{-}+H^{+} \qquad R-OH+H^{+} \Leftrightarrow R-HOH^{+} \qquad \text{Eq.2.44}$$

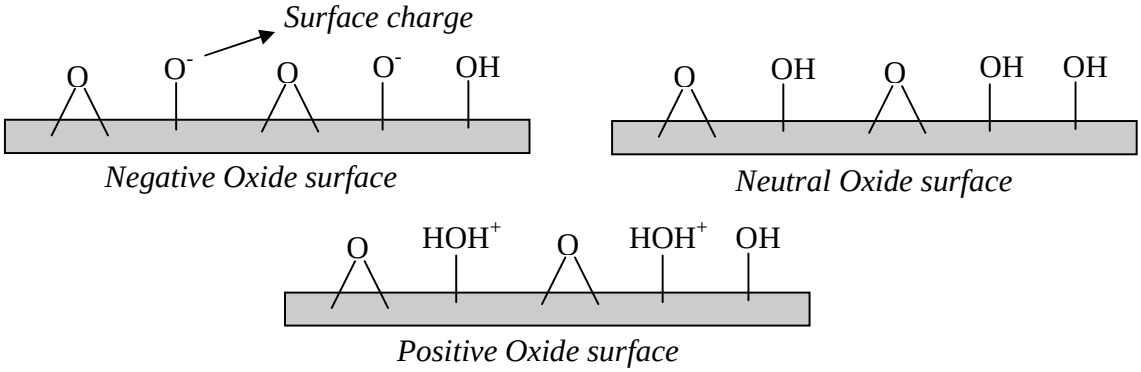

Fig. 2.14 Schematic distribution of the chemical surface groups on an oxide surface and charge surface group formation as a function of the pH.

In the oxide systems, the ions that determine charge are protons and hydroxyl groups and their concentrations are described by pH (pH = - log $[H^+]$; in water, $[H^+]\cdot[OH^-] = 10^{-14}$). They can bind to the surface groups $R\text{-}O^-$ and R-OH (forming R-OH and $R\text{-}HOH^+$) or respectively extract a H^+ from the surface group R-OH (forming an $R\text{-}O^-$ group at the surface) – see Fig. 2.14. As the concentration of charge determining ions varies, the surface charge density changes from positive to negative or vice versa (Parks, 1965; Hunter, 1981). The concentration of charge determining ions corresponding to a neutral or zero-charged surface is defined as a point of zero charge (p.z.c.) or zero-point charge (z.p.c.).

Table 2.1 gives a list of some p.z.c. values of selected oxides (Pierre, 1998). At pH > p.z.c., the oxide surface is negatively charged, since the hydroxyl group, OH^-, is the electrical determining ion. At pH < p.z.c., H^+ is the charge determining ion and the surface is positively charged. The surface charge density or surface potential, *E* in volts, can then be simply related to the *pH* and the Nernst equation (equation 2.43) can be written as (Pierre, 1998):

$$E = 2.303\, R_g T\, [(\text{p.z.c.}) - \text{pH}] / F \qquad \text{Eq. 2.45}$$

At room temperature, the above equation can be further simplified:

$E \approx 0.06\ [(p.z.c.) - pH]$ Eq. 2.46

Table 2.1 A list of p.z.c. of some common oxides in water

Solid	WO_3	V_2O_5	δMnO_2	βMnO_2	SiO_2	SiO_2 (quartz)	TiO_2	TiO_2 (calcined)
p.z.c.	0.5	1-2	1.5	7.3	**2.5**	**3.7**	6	3.2
Solid	Al-O-Si	ZrO_2	SnO_2	FeOOH	Fe_2O_3	Cr_2O_3	ZnO	Al_2O_3
p.z.c.	6	6.7	4.5	6.7	8.6	8.4	8	9

It can be noticed that for SiO_2 (silica is the main constituent of the glass), immerged in SB (pH = 6), the oxide surface is negatively charged. The same situation is met in the case of ITO (p.z.c. are included in the interval [3; 4.7] (Tobias, 2002)).

2.2.6 Water electrolysis

In a properly designed electrochemical cell, hydrogen will appear at the cathode (the negatively charged electrode, where electrons are pumped into the water), and oxygen will appear at the anode (the positively charged electrode). Assuming ideal faradaic efficiency, the generated moles of hydrogen is twice the moles of oxygen, and both are proportional to the total electrical charge that was exchanged through the solution. However, in many cells competing side reactions dominate, resulting in different products and non ideal faradaic efficiency.

Electrolysis of pure water requires a great deal of energy in the form of overpotential to overcome various activation barriers. Without this energy excess, the electrolysis of pure water occurs very slowly or not at all. This is in part due to the limited self-ionization of water. Pure water has an electrical conductivity about million times lower than 100 mM seawater. Many electrolytic cells do not behave as ectrocatalysts. The efficiency of electrolysis is increased through the addition of an electrolyte (such as a salt, an acid or a base) and the use of electrocatalysts.

In water at the negatively charged cathode, a reduction reaction takes place, with electrons from the cathode being given to hydrogen cations to form hydrogen gas (the half reaction balanced with acid):

Cathode (reduction): $2H^+(aq) + 2e^- \rightarrow H_2(g)$ $E_{red}^0 = 0$ V

At the positively charged anode, an oxidation reaction occurs, generating oxygen gas and giving electrons to the cathode to complete the circuit:

Anode (oxidation): $2H_2O(l) \rightarrow O_2(g) + 4H^+(aq) + 4e^-$ $E_{ox}^0 = -1.23$ V

The same half reactions can also be written with base as listed below.

Cathode (reduction): $2H_2O(l) + 2e^- \rightarrow H_2(g) + 2OH^-(aq)$ $E_{red}^0 = -0.83$ V

Anode (oxidation): $4OH^-(aq) \rightarrow O_2(g) + 2H_2O(l) + 4e^-$ $E_{ox}^0 = -0.4$ V

Combining either half reaction pair yields the same overall decomposition of water into oxygen and hydrogen:

Overall reaction: $2H_2O(l) \rightarrow 2H_2(g) + O_2(g)$

The number of hydrogen molecules produced is thus twice the number of oxygen molecules. Assuming equal temperature and pressure for both gases, the produced hydrogen gas has therefore twice the volume of the produced oxygen gas. The number of electrons pushed through the water is twice the number of generated hydrogen molecules and four times the number of generated oxygen molecules.

Decomposition of pure water into hydrogen and oxygen at standard temperature and pressure is not favorable in thermodynamical terms. Thus, the standard potential of the water electrolysis cell is -1.23 V at 25 °C at pH 0 (H^+ = 1.0 M). It is also -1.23 V at 25 °C at pH 7 ($H^+ = 1.0 \times 10^{-7}$ M) based on the Nernst equation.

The negative voltage indicates the Gibbs free energy for electrolysis of water is greater than zero for these reactions. This can be found using the $\Delta G = -n F E$ equation from chemical kinetics, where *n* is the moles of electrons and *F* is the Faraday constant. The reaction cannot occur without adding necessary energy, usually supplied by an external electrical power source.

2.2.7 Electric proprieties of ITO material

Apart from its conductive property, indium-tin oxide (ITO) has many other advantages such as high optical transmittance in the visible and near-IR region, a robust chemically and mechanically nature, it can be easily patterned and has excellent adhesion property to many substrates (Moore, 2006).

Before testing the behavior of the living cells on the ITO surface in buffer solutions (17 or 1.7 mM), an electrochemical characterization of this substrate, was

required, (we employed 3 electrodes setup – Fig. 2.15A). We used cyclic voltammetry measurements for the characterization of ITO surfaces (Fig. 2.15B, in 1.7 mM phosphate sucrose buffer solution) with a scanning speed of 50 mV/s.

We obtained 3 potential (current) domains: below – 0.1 V/Ag,AgCl, the current (faradaic current) increases exponentially because of water reduction forming negative hydroxyl ions OH^-; between -0.1 and +0.8 V/Ag,AgCl, the current remains approximately constant and very low (0.5 µA, capacitive current); at more than 0.8 V/Ag,AgCl, the current increases exponentially because of water oxidation, resulting in the formation of positive H_3O^+ ions (faradaic current, Fig. 2.15B).

The quantity of produced charged ions (protons coordinated to a water molecule - H_3O^+ or hydroxyl ions, OH^- respectively) is directly proportional to the current intensity and to the duration of the current delivery (faradaic current); for ITO, the capacitive current, due to material polarization, is much less important than the faradaic one (see Fig. 2.15B).

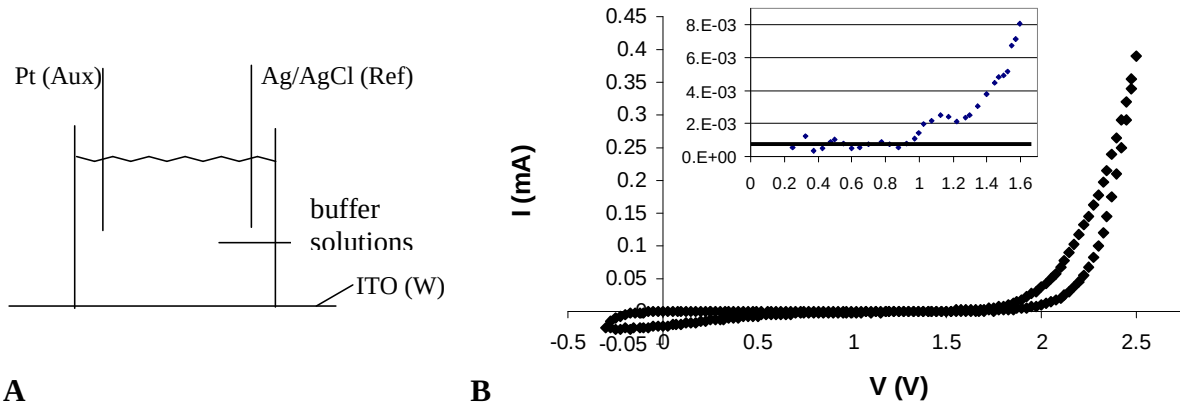

Fig. 2.15 A. Experimental setups for electrochemical characterization of ITO-glass surface as working electrode (W). **B**. Cyclic voltammetric curve obtained in 1.7 mM phosphate sucrose buffer solution (v = 50 mV/s); the insert presents the magnified [0.2 V-1.6V] window. The thick black line from the inset delimitate the capacitive current.

However, ITO is reduced and suffers an important deterioration when the negative potential falls below -1.5 V/Ag,AgCl for 30 s, (- 1.5 mC).

Since, during pulse application, the protons or hydroxyl ions accumulate at the surface, we measured the zeta potential of an ITO surface in 10 mM KCl at different pH (Fig. 2.16).

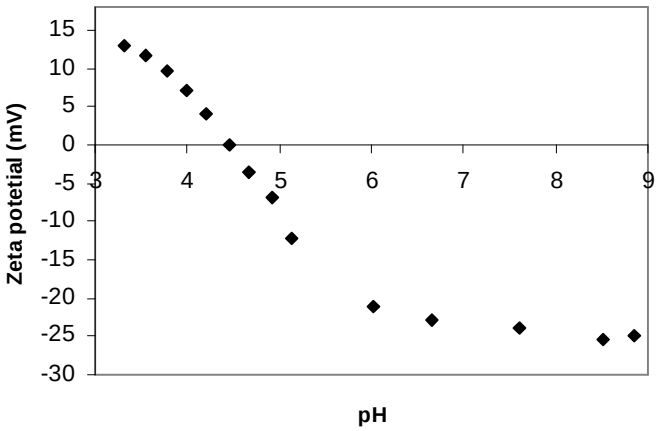

Fig. 2.16 ITO surface zeta potential versus pH of the electrolyte (10 mM KCl). It can be noticed that the p.z.c = 4.45.

At the surface of an oxide material, charged species depend on the pH. When the latter varies, the surface charge density changes from positive to negative or vice versa. The pH corresponding to a neutral or zero-charged surface is defined as the point of zero charge (p.z.c.). It can be found immediately that the p.z.c. of ITO surface is 4.45 (Fig. 2.16). This experimental value fits with the reported values in literature in the interval [3; 4.7] (Tobias, 2002).

2.2.8 Interactions between two charged particles: DLVO theory. Applications to the situation: one charged particle and a charged surface

The total energy interaction between two particles (Φ), which are electrostatically stabile, is the combination of van der Waals attraction (Φ_A) and electrostatic repulsion (Φ_R):

$$\Phi = \Phi_A + \Phi_R \qquad \text{Eq. 2.47}$$

Interactions between particles are complex. One of the interactions between particles is directly associated with the surface charge and the electric potential adjacent to the interface. The electrostatic repulsion between two particles arises from the electric surface charges, which are attenuated to a varied extent by the double layers. When two particles are far apart, the double layers do not overlap and electrostatic repulsion between two particles is zero. However, when two particles approach each other, the double layers overlap and a repulsive force develops. An electrostatic repulsion between

two spherical particles of the different radius (r_1 and r_2) and the same surface charge, is given by (Hiemenz, 1997):

$$\Phi_R = 4 \pi \varepsilon_r \varepsilon_o (r_1 r_2 / r_1 + r_2) \Phi_0^2 \exp(-\kappa S) \quad \text{Eq. 2.48}$$

where Φ_0 is the surface potential, κ is given by Eq. 2.24 and S is the particles separation distance (see Fig. 2. 17).

In approximation Debye-Hückel (small surface potentials, $\Phi_0 < 50/z$ mV at 25ºC), for a spherical particle of radius r near a flat surface ($r_{surface} = \infty$), the electrostatic repulsion is given by:

$$\Phi_R = 4 \pi \varepsilon_r \varepsilon_o r \Phi_0^{surface} \Phi_0^{particle} \exp(-\kappa S) \quad \text{Eq. 2.49}$$

with the same symbolisms like above.

When particles are small, typically micrometric or less, and are dispersed in a solvent, van der Waals attraction force and Brownian motion play important roles, whereas the influence of gravity becomes negligible. Van der Waals force is a weak force and becomes significant only at a very short distance (Å). Brownian motion ensures the particles colliding with each other at all times. The combination of van der Waals attraction force and Brownian motion would result in the formation of agglomeration of the particles.

Van der Waals interaction between two particles is the sum of the molecular interaction in the surrounding medium such as solvent. Integration of all the van der Waals interactions between two molecules over two spherical particles of radius, r, separated by a distance, S, gives the total interaction energy or attraction potential (Hiemenz, 1997).

$$\Phi_A = - A/6 \{2r^2/(S^2+4rS) + 2r^2/(S^2+4rS+4r^2) + \ln[(S^2+4rS)/(S^2+4rS+4r^2)]\} \quad \text{Eq. 2.50}$$

where the negative sign represents the attraction nature of the interaction between two particles, and A is a constant termed *the Hamaker constant*, which has a magnitude in the order of 10^{-19} to 10^{-20} J, and depends on the polarization properties of the molecules in the two particles and on the medium which separates them.

Equation 2.50 can be simplified under various boundary conditions. For example, when the separation distance between two equal sized spherical particles are significantly smaller than the particle radius, i.e., $S/r << 1$, a simple expression of the van der Waals interaction energy is obtained:

$\Phi_A = -A\ r/12\ S$ Eq. 2.51

In the case of two spheres with different radius (r_1 and r_2) one obtains:

$\Phi_A = -A\ r_1r_2/((r_1+r_2)\ 6\ S)$ Eq. 2.52

The van der Waals interaction energy between two particles is different from that between two flat surfaces. Furthermore, it should be noted that the interaction between two atoms ($\Phi_A \propto S^{-6}$) are significantly different from that between two particles.

The van der Waals interaction energy (Φ_A) and attraction force (F) for a sphere with a radius *r* near a planar surface ($r_{surface} = \infty$), as shown in Figure 2.17A, is given by:

$\Phi_A = -A_{123}\ r/6S$ and $F = A_{123}\ r/6S^2$ Eq. 2.53

where A_{123} is the Hamaker constant for substances "l" (sphere) and "2" (glass) in presence of medium "3" (for example, water) and *S* is the separation distance between spherical particle and surface (Israelachvili, 1992). The attraction force dependence on distance for a cell of radius $r = 5\cdot10^{-6}$ m and density $\rho = 1.0665$ g/cm^3 (like *Dictyostelium* amoebae; Fukui, 2000) near a glass surface ($A_{123} \cong 10^{-20}$ J), in aqueous solution, is drawn in Figure 2.17B.

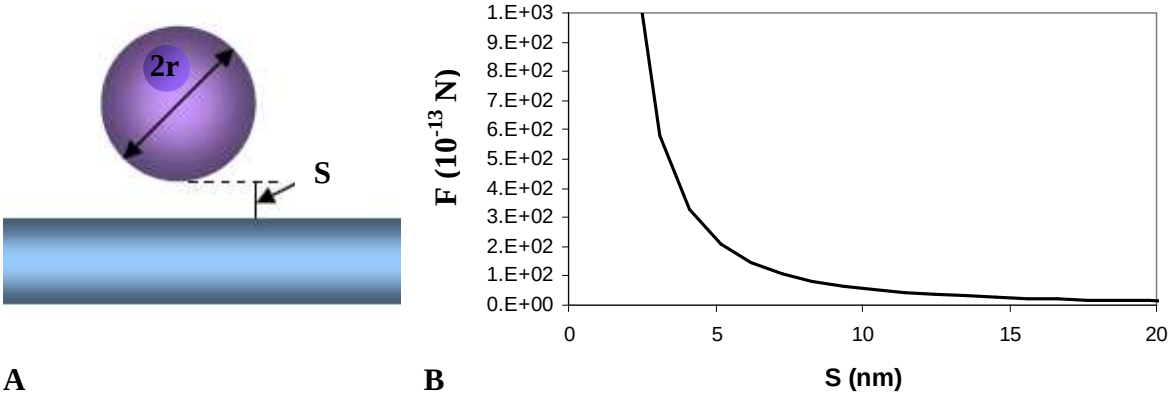

Fig. 2.17 A. Schematics of a particle near a flat surface. **B**. Attraction force (F) estimation for a cell ($r = 5\ 10^{-6}$ m) near a glass surface in aqueous solution versus distance separation (S).

For a distance *S* = 100 nm, the attraction force between a *Dictyostelium* cell and a glass surface is $5.3\cdot10^{-14}$ N, which is negligible comparatively with the apparent gravity ($3\cdot10^{-13}$ N).

Although the nature of the attraction energy between two particles is the same as that between two molecules, integration of all the interaction between molecules from

two particles and from medium results in a very different dependence of the force on the distance between particles. The attraction force between two particles decays very slowly and extends over distances of nanometers. As a result, a barrier potential must be developed to prevent agglomeration. Two methods are widely applied to prevent agglomeration of particles: electrostatic repulsion and steric exclusion.

The electrostatic stabilization of particles in a suspension is successfully described by the DLVO theory, named after Derjaguin, Landau, Verwey, and Overbeek (Overbeek, 1984). The interaction between two particles in a suspension is considered as the combination of the van der Waals attraction potential and the electric repulsion potential. There are some important assumptions in the DLVO theory:

- Infinite flat solid surface, uniform surface charge density and no re-distribution of surface charge, i.e., the surface electric potential remains constant.
- No change of concentration profiles of both counter-ions and surface charge determining ions, i.e., the electric potential remains unchanged and solvent exerts influences via dielectric constant only, i.e., no chemical reactions between the particles and solvent.

It is very clear that some of the assumptions are far from the real picture of two particles dispersed in a suspension. For example, the surface of particles is not infinitely flat, and the surface charge density is most likely to change when two charged particles get very close to each other. However, in spite of the assumptions, the DLVO theory works very well in explaining the interactions between two approaching particles, which are electrically charged, and thus is widely accepted in the research community of colloidal science.

At a distance far from the solid surface, both the van der Waals attraction potential and the electrostatic repulsion potential tend to zero. Near the surface is a deep minimum in the potential energy produced by van der Waals attraction. A maximum is located a little further away from the surface, as the electric repulsion potential dominates the van der Waals attraction potential (Hiemenz, 1997) (Fig. 2.18).

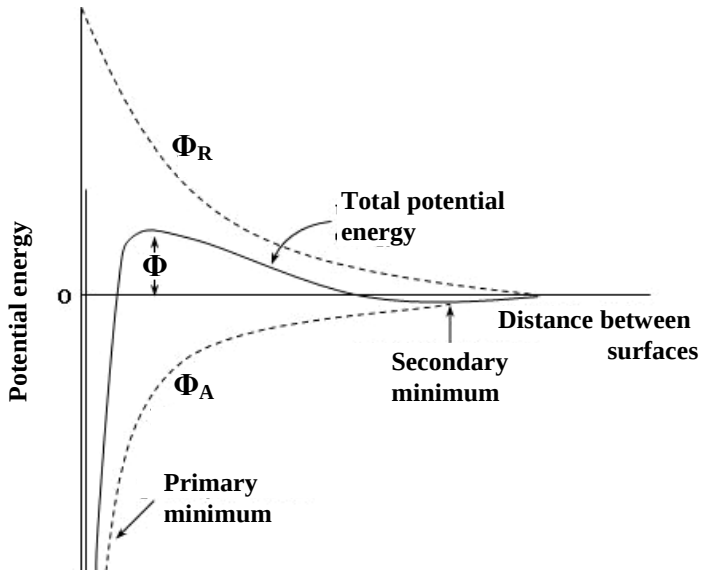

Fig. 2.18 van der Waals attraction potential (Φ_A), electric repulsion potential (Φ_R), and the combination of the two opposite potentials (continuous line, Φ) as a function of distance from the surface of a spherical particle

The maximum is also known as repulsive barrier. If the barrier is greater than ~10 kT, where *k* is the Boltzmann constant, the collisions of two particles produced by Brownian motion will not overcome the barrier and agglomeration will not occur. Since the electric potential is dependent on the concentration and valence state of counter-ions and the van der Waals attraction potential is almost independent of the concentration and valence state of counter-ions, the overall potential is strongly influenced by the concentration and valence state of counter-ions.

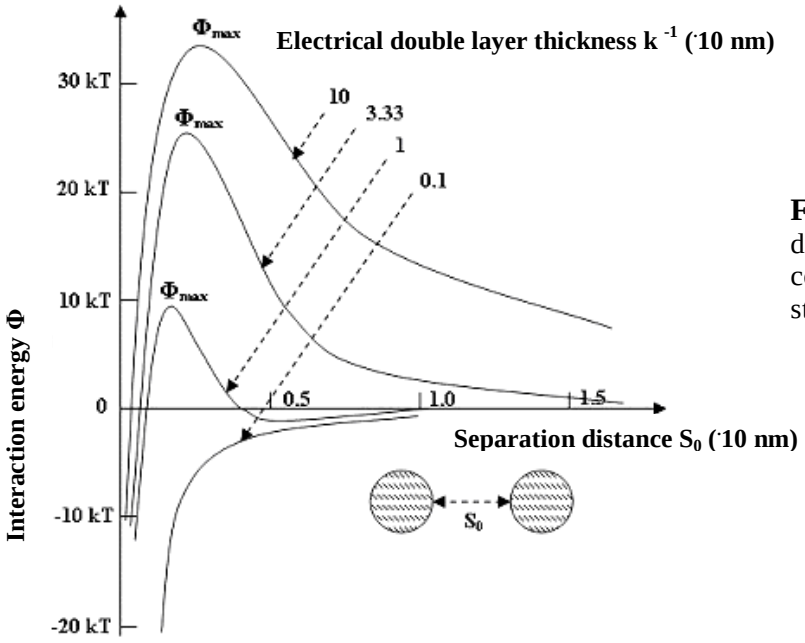

Fig. 2.19 Interaction energy dependence of the concentration and valence state of counter-ions.

An increase in concentration and valence state of counter-ions results in a faster decay of the electric potential as schematically illustrated in Fig 2.19 (Overbeek, 1984). As a result, the repulsive barrier is reduced and its position is pushed towards the particle surface. The secondary minimum observed in Fig.2.18 is not necessary to exist in all situations, and it is present only when the concentration of counter-ions is high enough. If a secondary minimum is established, particles likely associate with each other and form a colloid fluid, which is known as flocculation.

2.2.9 Model of cell attachment to charged surfaces as a function of ionic concentration

This kinetic model is based upon the observation that cell spreading is an irreversible process. When cells are able to reach the surface, so that a small visible contact is formed (about 4 μm^2), this contact extends and the cell spreads. The number of cells spreading as a function of time is thus given by a first order equation:

$$dN/dt = k(N_0 - N) \qquad \text{Eq 2.54}$$

The number of cells spreading at a given salt concentration is determined after τ =10 minutes, which is much longer than the sedimentation time of the cells (about 1 minute). The fraction of cells attached to the surface is thus linked to *k*, the rate of formation of cell-surface contact for a cell levitating at about 100 nm over the surface.

$$N(\tau)/N_0 = 1 - \exp(-k\tau) \qquad \text{Eq 2.55}$$

We assume that the rate of formation of cell-surface contact is thermally activated (Decave, 2003; Garrivier, 2002; Bell, 1984):

$$k = k_0 \exp\left(-\Delta G^* / k_B T\right) \qquad \text{Eq 2.56}$$

where k_0 is an intrinsic collision frequency between the cell membrane and the surface, ΔG^* is the energy of the activation barrier to overcome to form a stable cell-surface contact, and $k_B T$, the Boltzman thermal energy term. The potential energy of this interaction is maximal at a cell-surface distance *d* and the difference between this value and the minimum at longer distances constitutes the activation barrier.

ΔG^* is given by the DLVO theory (Atkins, 2006) and depends on the ionic concentration. It can be written as the sum of a term representing the electrostatic repulsion, ΔG_E, a term representing the activation energy at large ionic concentrations, ΔG^*_0, when electrostatic repulsion is negligible and a term representing van der Waals attraction potential, Φ_A, which also could be neglected for distances grater than 2.5 nm nanometers (Evans, 1995; see also fig. 2.19). For simplicity, we assume that the cell is round (radius r) and the surface is planar, and that both have identical surface potential Φ_0.

$$\Delta G^* \approx \Delta G_E = 4\pi\varepsilon_0\varepsilon_r r\Phi_0^2 e^{-\kappa d} \approx U_0 e^{-\kappa d} \qquad \text{Eq 2.57}$$

where ε_0 and ε_r are the vacuum and relative dielectric constants and κ^{-1} the Debye length. U_0/e is the electrostatic energy at the Debye length. The Debye length is inversely proportional to the square root of the ionic strength, the latter being proportional to the salt concentration:

$$\kappa d = bdC^{0.5} \qquad \text{Eq 2.58}$$

where *C* is the salt concentration. For monovalent salts, b = 0.31 $nm^{-1}M^{-0.5}$ and for divalent ones b = 0.54 $nm^{-1}M^{-0.5}$, with d in nm. From equations 2.24-2.28, it follows that the fraction of cells attached to the surface after 10 minutes is given by:

$$N/N_0 = 1 - \exp(-a\exp(-ce^{-bdC^{0.5}})) \qquad \text{Eq 2.59}$$

where $a = k_0\tau \exp(-\Delta G^*_0/k_BT)$ and $c = U_0/k_BT$.

The association rate of firm cell-surface contact formation k depends on the salt concentration as:

$$k = a/\tau \exp\left(-ce^{-bdC^{0.5}}\right) \qquad \text{Eq 2.60}$$

The curve relating k to C is sigmoidal. For $C < C_1 = \left[(bd)^{-1}\ln(c^{-1}\ln 10)\right]^2$, the association rate is less than 10% of its maximum. For $C_1 < C < C_2 = \left[(bd)^{-1}\ln(c^{-1}\ln 2)\right]^2$, the association rate increases almost linearly with C, and for $C > C_2$, it tends to a maximum value.

Chapter III Results

3.1 Unsynchronized adhesions

3.1.1 Dynamics of cell-substrate contact areas during spreading and motility

Recall of thesis work of S. Keller

Before a cell adheres on a surface, it has to make a first contact point with the substrate. A few seconds after, a significant cell adhesion area is visible and cells start to extend pseudopods in one or several directions. A succession of pseudopods follows, resulting in an anisotropic increase in cell-substrate contact area. After about one minute, the cell starts retracting part of its contact area. At this point, pseudopods still extend but their growth rate decreases to match the retraction activity. Once a balance between *gain (area increased)* and *loss (retracted area)* areas is reached, spreading is over and cells start to move on the surface in a given direction (Fig 3.1).

Globally, *Dictyostelium* cells spread fast (1-2 min), in an anisotropic manner. A representative example of cell spreading on a glass surface in SB (Sörensen buffer – see Materials and Methods), is shown in Fig. 3.1.

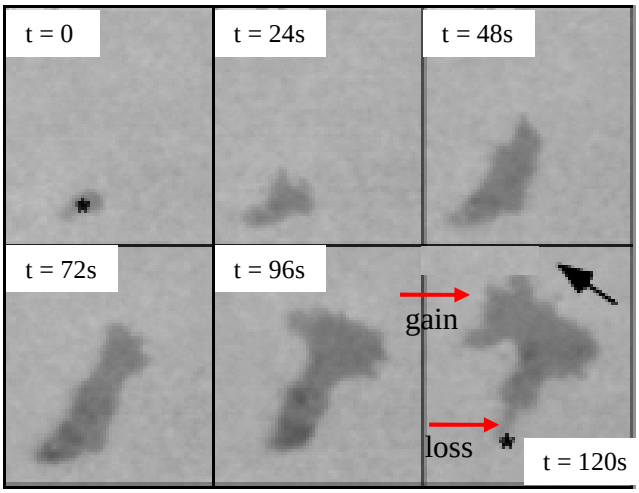

Fig. 3.1 RICM images of a *Dictyostelium* cell spreading on a glass surface in the presence of 500 µM $CaCl_2$. After full spreading, the cell starts moving in the direction indicated by the black arrow (t = 120s). The asterisk in the first and last frames indicates the initial contact point. The red arrows indicate the loss and the gain areas.

Cells were allowed to sediment on a glass surface in SB and cell-substrate contact areas were visualized by Reflection Interference Contrast Microscopy (RICM, see Materials and Methods). Cells had various forms, elongated or more rounded, spread rapidly or slowly, and reached different maximal area (example shown for 3 cells, Fig 3.2). However, for all cells one can distinguish two steps in spreading kinetics (total contact area as a function of time): a quasi-linear increase in contact area was followed by a plateau phase.

For each individual cell, recording time started when the cell made contact with the substrate, corresponding to a visible area of about 2 μm^2. For the cell of Figure 3.1, after the initial contact, cell-substrate contact area mainly increased in a single direction for about 60 sec, then a new spreading direction appears at 90° from the first one. At the same moment, the cell started retracting its initial contact area. Maximum cell-substrate contact area was reached at 100 sec (generally the average is 110 μm^2) and from that time, cell-substrate contact dynamics resulted in net cell movement.

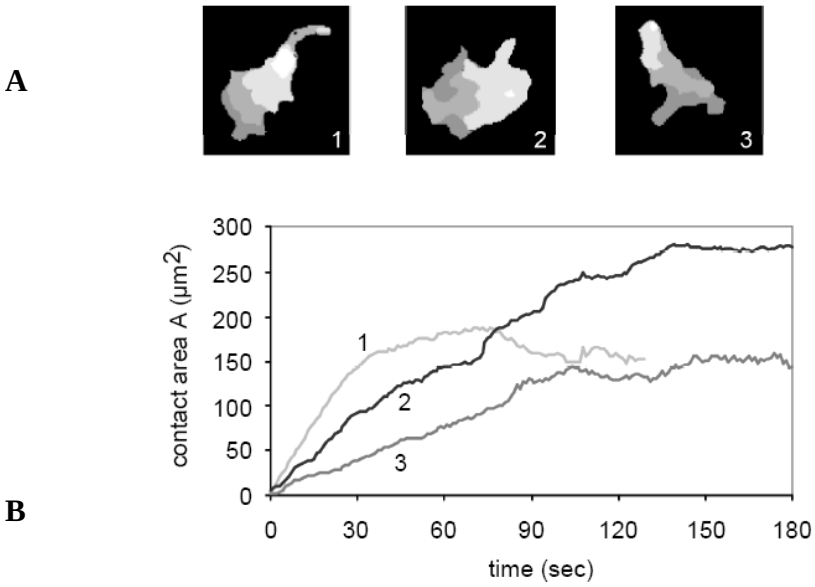

Fig. 3.2 Illustrative examples of *Dictyostelium* form variability during spreading
A: Composite picture showing in increasing greyscale, the area gained by the cells during 24 s at time intervals of 3 seconds. B: Spreading kinetics of the three cells shown in A: total contact area as a function of time.

Cells need actin polymerization for spreading

Chamaraux derived a very general expression, describing cell spreading (Chamareaux, 2005) (Eq.3.1):

$A(t) = A_{max} \tanh(\alpha t)$, where α is a characteristic spreading time constant Eq. 3.1

The hypothesis underlying this model is the control of cell spreading by actin polymerization, following two antagonist processes: i) stimulation of actin polymerization through a cell-substrate contact-induced signaling. ii) initiation of actin depolymerization by membrane tension, which increases with the contact area.

Cell spreading requires actin cytoskeleton remodeling. This is clearly shown by adding latrunculin A (3µM), a drug that promotes actin filament depolymerization. This drug strongly decreases the initial spreading of *D. discoideum* cells and makes that contact surface round (Fig.3.3).

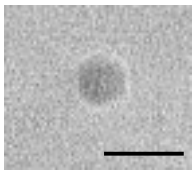

Fig. 3.3 RICM image of contact area of a cell in SB +3 µM Lantraculine on glass; the bar scale is 2 µm

Equation 3.1 contains two parameters: A_{max} (μm^2), the maximum area observed between the cell and the substrate, and α (s^{-1}), the characteristic spreading time. This equation was used to fit the spreading kinetics shown in Fig. 3.4 (A_{max} = 201 ± 6 μm^2; α = 0.0115 ± 0.0007 s^{-1}). The global shape of the spreading kinetics is in good agreement with the model's prediction. However, in details, experimental data sometimes vary significantly from the model curve, exhibiting alternatively faster and slower spreading events. In order to characterize better the details of the kinetics, cell-substrate area variations was decomposed *into gain and loss zones* (Fache, 2005).

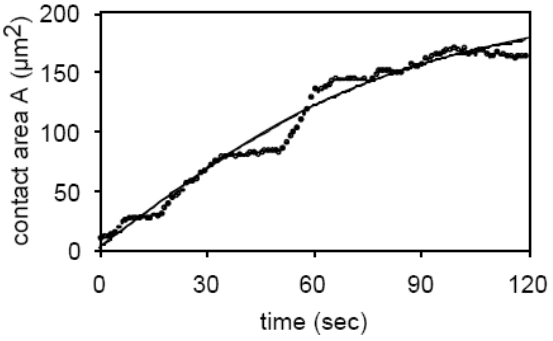

Fig. 3.4 Spreading kinetics of the cell shown in Fig. 3.1: total contact area as a function of time (black points). The solid line is a fit of the experimental data with Eq. 3.1.

Protrusion and retraction zones were defined as the area gained or lost over a 3 seconds time interval. Fig. 3.5A shows the areas gained during 20 seconds intervals for the considered cell. Protrusive and retractile activities (μm^2/sec) for the cell shown in Fig. 3.1 were plotted as a function of time in Fig.3.5B.

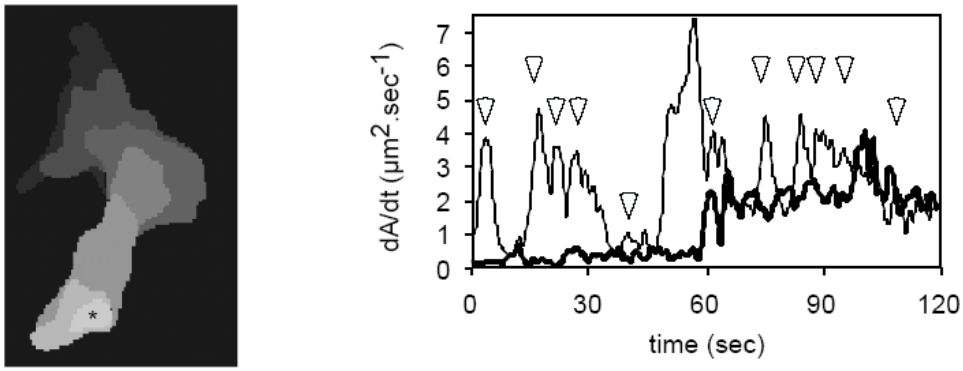

A **B**

Fig. 3.5 A. Composite picture showing in increasing greyscale the area gained by the cell shown in Fig 1, during successive time intervals for 24 s. The initial contact area appears in white.
B. Dynamics of cell-surface contact areas during spreading of the cell: gained area (thin line) and lost area (thick line) as a function of time. Arrowheads point to significant protrusion peaks.

As the cell reached the substrate, only protrusion activity was detectable, and retractions started only at 55 seconds. The end of spreading and the transition from spreading to motility corresponds to the moment when protrusion and retraction curves first cross. From the above figure, it is obvious that protrusive activity was not steady, but exhibited large peaks.

Plotting the time occurrence of successive significant protrusion peaks reveals that they appear regularly. For the cell under study, the mean period Δt was about 11.5 seconds (Fig. 3.6).

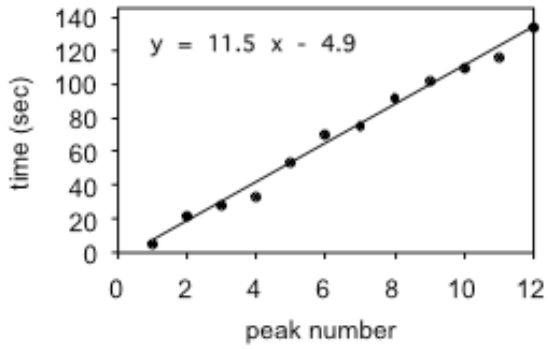

Fig. 3.6 Time occurrence of successive peaks in the kinetics of gained area shown in Fig. 3.5. The distribution can be linearly fitted, defining an average period of 11.5 s.

Keller studied a set of 15 cells spreading on a glass surface. For a given cell, a characteristic period *T* was determined by averaging Δt. This period does not significantly vary from cell to cell (<T> = 10.68±1.9 s), which shows that most variation indeed originates from intrinsic fluctuation of cell activity.

Furthermore, oscillations in protrusion activity are clearly visible. Quantitatively, the first maximum in the protrusion curve does not appear randomly, but occurs at 6.24 ± 2.64 seconds after cell-substrate contact. The uncertainty in the position of the first peak is due to the lack of precision in the determination of the initial time of contact with the substrate, since it corresponds to very small areas. Therefore, the contact with the substrate could trigger the first protrusion peak.

The uncertainty in the onset of spreading generates phase differences between cells that mask their common behavior. In order to phase cell contributions together, one can shift individual cell protrusion kinetics along time so that the first maximum occurrs at 6 seconds upon cell-substrate contact. This phasing procedure clearly increased the size of the oscillations seen on average protrusion kinetics (Fig. 3.7), supporting the existence of a common 10.8 seconds period.

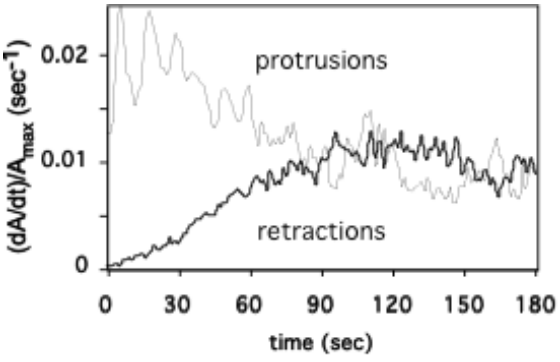

Fig. 3.7 Average of normalized gain and loss kinetics after alignment of kinetics on the first peak of gain activity (set at 6 s). The statistical error is 0.0022 s^{-1}. The averaged time interval between the 6 first peaks is 10.8 ± 2.0 s for 15 cells.

Oscillating protrusion activity is molecularly driven by actin polymerization. We therefore extended the work of S. Keller by monitoring the kinetics of actin polymerization near the surface that accompanies spreading.

3.1.2 Cyclic actin polymerisation activity during cell adhesion in SB

In order to verify the oscillating character of actin polymerization, epifluorescence microscopy was employed. LimE-GFP cells were used for fluorescent tracking of actin polymerization in SB. Here, we used a fluorescent version of Lim protein (a GFP fusion construct with a fragment of LimE, LimE-GFP) to display and to measure the actin dynamics in Dictyostelium.

In time course of the cell spreading LimE – GFP fluorescence appeared and disappeared locally (Fig. 3.8). We named these short-lived localized activities *fluorescence events*. They indicated a local actin polymerization followed by a depolymerization.

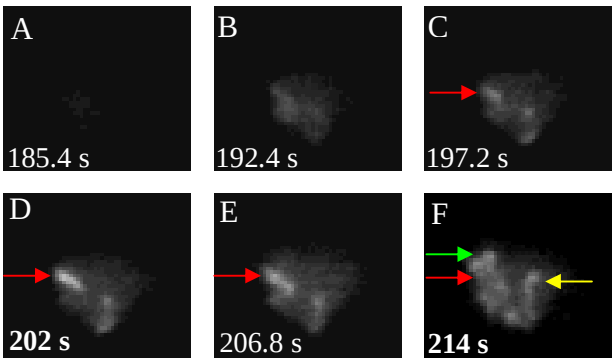

Fig. 3.8 Examples of LimE$^{\Delta coil}$-GFP fluorescence events during a *Dictyostelium* cell spreading on a glass surface. A and B, chronological images during cell sedimentation, one can observe the cell approaching to the surface; C, the red arrow point a zone with an increased fluorescence; in the same place the fluorescence will reach a maximum (D) and will decreases (E) until its total evanescence (F); in the same time in the other zones, an increase of fluorescence activities take place (F, green and yellow arrows). The intensity of fluorescent zones which are not pointed out by arrows were under the threshold established by us or were not localized at the cell edges (see Materials and Methods).

Focusing at glass surface, the first observed fluorescent event (Fig. 3.8 and Fig. 3.9 – at t = 202 s) indicated that the cell adhesion has already occurred. We do not know with exactitude when and where at the surface, the first contact point had taken place and if it coincides in time with the maxima of fluorescence event or in space with the event localization. Nevertheless, successive fluorescent events less or more regularly spaced in time were observed, indicating oscillating actin activity.

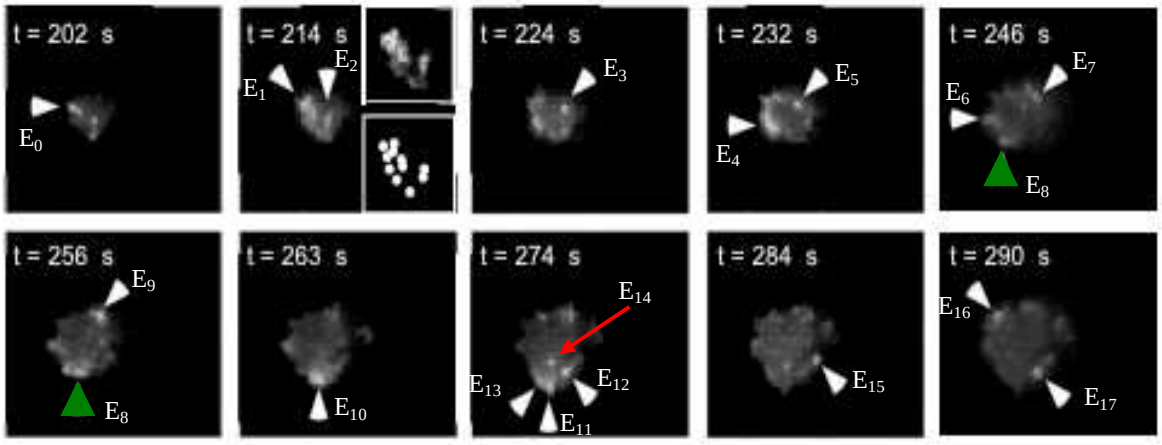

Fig. 3.9 LimE$^{\Delta coil}$-GFP fluorescence images of a *Dictyostelium* cell spreading on a glass surface. Arrows point to regions of significant actin polymerization (Event-E_i). At t = 214s, upper inset: brightness and contrast are changed to enhance the visibility of actin foci; lower inset: the position of individual actin foci is denoted by spots. The fluorescent zones which are not pointed by arrows are under the established intensity threshold or do not occur at the cell edges – e.g. red arrow (see Materials and Methods).

We employed the following technique for identifying the actin polymerization events: every fluorescent zone was quantified individually and they were plotted in the same graph using different colors, which allowed identifying individual events (Fig. 3.10). There are events that occur frequently at the same time. The events (E_i) are identifiable to the maxima of fluorescence observed in the images of Fig. 3.9.

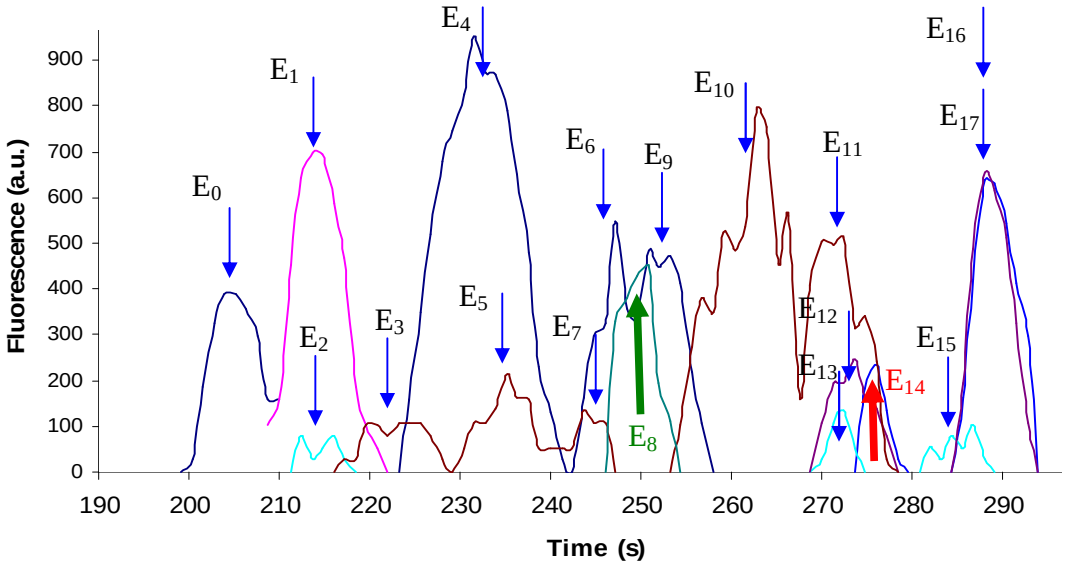

Fig. 3.10 Individual fluorescence in regions of significant fluorescence reinforcement (E_i), for the cell shown in Fig. 3.9. For sake of clarity, recordings corresponding to different regions are coloured differently. Green arrow correspond to an event seen in two images taken at 246s and 256 s shown in Fig. 3.9, and red arrow points an event which not occurs at the cell edge.

The first event (E_0) corresponds to the first fluorescence maxima when the cell began to contact the surface under gravity. The fluorescence activity is later reinforced approximately in the same zone, inducing the presence of two successive actin polymerization events only spaced in time.

Individual events often – but not always - match changes in cell protrusion direction. This is especially obvious for cells extending successive protrusions in different directions. Since actin polymerization maxima that are located in different areas of the cells appear simultaneously (see Fig 3.9 and 3.10, for example, E_1-E_2), one can infers that the actin cytoskeleton is organized globally.

It can be noticed that an oscillating process of actin polymerization occurs. This pulsatory process suggests that the first contact point with the substrate triggers actin polymerization that could deform the cell membrane and lead to the formation of successive contact points.

The time of occurrence of the maxima of the peaks appearing in Fig. 3.10 (without those pointed by the red arrow) was plotted against the corresponding peak number, considering the first event (Event0) as the origin. Thus, for the studied cell, we obtain the following representation of fluorescent maxima events number versus time (Fig. 3.11):

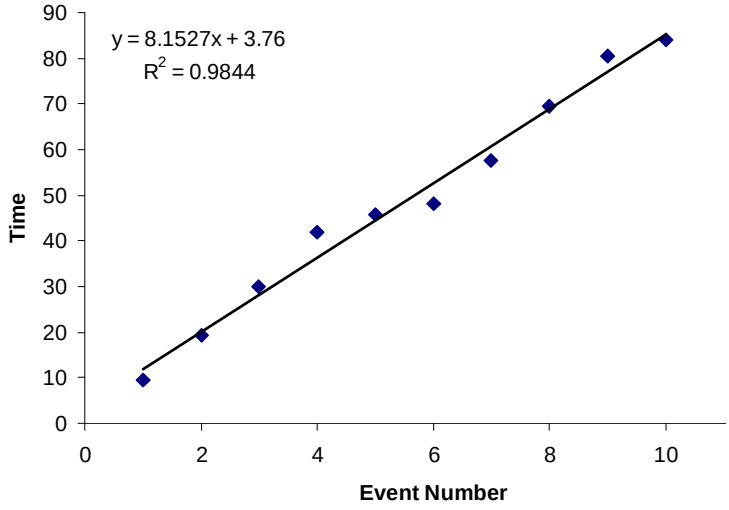

Fig. 3.11 Time occurrence of successive peaks during cell adhesion in SB; the distribution was linearly fitted, defining an average period of 8 s

We also can define an average period of maxima apparition.

From a group of *18* studied cells, *14* cells (78%) exhibit 6 or more, fluorescent event peaks within 65 s after the apparition of the first peak and *4* cells had less than 6

peaks after the apparition of the first peak. For the cells that had 6 or more fluorescent event peaks, the time interval between the maxima was 4-11 seconds (Fig. 3.12A). The probability of an event apparition after the first event (E_0), is another important parameter. Every probability was calculated by counting the cells that having a maximum in a given one-second interval, divided by the total number of analyzed cells (*14* cells) (Fig. 3.12B).

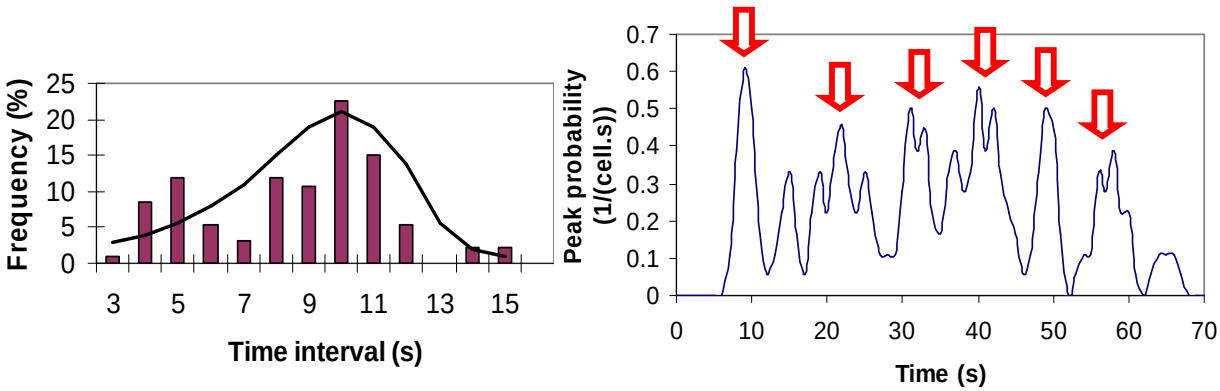

A **B**

Fig. 3.12 (**A**) Histogram of time intervals between adjacent peaks of LimE$^{\Delta coil}$-GFP fluorescence reinforcement. For all cells, the first peak is set to t = 0 s. The solid line represents the best fit of the experimental data with a normal distribution. (**B**) Frequency of appearance of LimE$^{\Delta coil}$-GFP fluorescence peaks, after the first peak, for 14 individual cells as a function of time. The data were expressed as probability of appearance of a peak per cell and per second.

Analysis of Fig. 3.12B shows that the probability for the second polymerization event to appear, for all the cells, between 10th and 11th seconds after the apparition of the first event (E_0), was approximately 0.6 $s^{-1}cell^{-1}$. If we integrate over a 3 seconds window, 72% of the cells would have the second peak between 8 and 11 seconds after the first one. Moreover, the probability that the cells have three peaks of activity at 9.5±1 s, 22±1 s and 31±1 s is higher than 0.2.

3.1.3 Cells that contact the surface under the action of gravity are not synchronized

In this experiment, the cells were not synchronized because they undertook the action of gravity, thus they were making the first contact points with the substrate at different times (Fig. 3.13). Moreover, the time of first contact with the surface (t_0) was not precisely known.

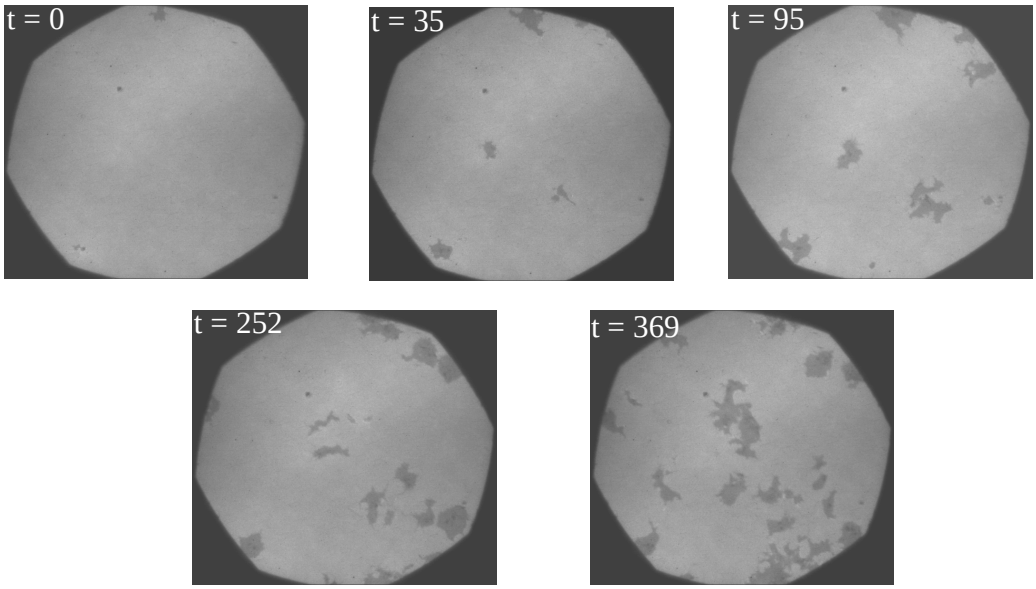

Fig. 3.13 Sequence of RICM images with the AX_2 cells sedimentation on glass surface under the action of gravity.

We denote here the *asynchrony* as the time difference between the moments at which the first and the last cell arriving on the surface started spreading. For the experiment shown in Fig. 3.13 asynchrony was 369 s.

A biochemical analysis would be profitable if an entire cell population (minimum of one million cells) would make the first contact point with a surface at the same time, starting the actin polymerization process in a synchronized way.

Conclusions:

We have shown in this subchapter that *Dictyostelium* cells spread using a periodic protrusion activity. Moreover, the actin polymerization, which drives membrane protrusions, is also oscillatory with almost the same period.

In the next subchapter, we will analyze the effect of an applied potential on the cells deposited on a conductive material, aiming to synchronize their spreading on the surface.

3.2 Electric field influence on adherent cells

3.2.1 Influence of the electric field on the cells deposited on the ITO material

Introduction

It is well known that *Dictyostelium discoideum* adheres to all kinds of treated or non-treated materials or substrates, in different buffers and in a wide range of buffer concentrations. We first used indium tin oxide (ITO, see Material and Methods) covered glass to test cell adherence in standard conditions and without the use of external current source. Thus, in 17 mM SB (SB - Sörensen buffer, see Material and Methods) and 1.7 mM phosphate sucrose buffer, cells falling under the action of gravity (G) adhere in identical way on both glass surface and ITO substrate (Fig. 3.14).

At the ionic strength of I = 24 mM and even less, I = 2.4 mM, the electrostatic repulsive force (**F_e**) between the negative groups of the cell membrane and the negative charges of ITO oxides (Fig.3.15), appearing on the surface in contact with the buffer solution, is not sufficient to inhibit cell surface contact and spreading. Moreover, there is an attractive potential that can be taken into consideration (Evans, 1995), especially for small distances from the surfaces (less than 2.5 nm)-see DLVO theory (Overbeek, 1984).

The apparent gravity force (**Ga = G - Fa**) on a *D. discoideum* cell can be estimated from its volume (500 fL), its density (1.0665 g/cm^3) (Fukui, 2000) and taking into account the Archimedes force (**Fa**), to be 0.3 pN ($Ga = \Delta\rho \cdot g \cdot V = 0.066 \cdot 1000 \cdot 10 \cdot 500 \cdot 10^{18} = 0.3 \cdot 10^{-12}$ N).

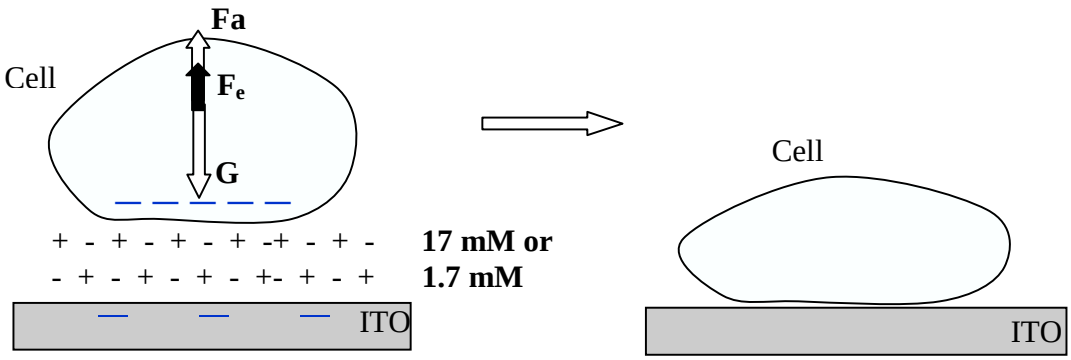

Fig 3.14 Schematic way of cell spreading; the electrostatic repulsion don't prevent the cell adhesion; **Fa** - Archimedes force, **F_e** - electrostatic repulsive force, **G** – gravity.

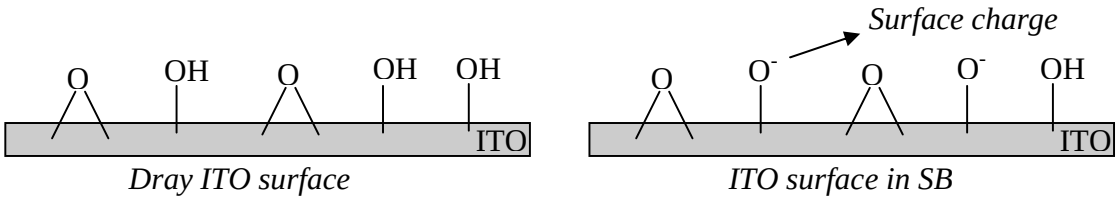

A **B**

Fig. 3.15 (**A**) Schematic distribution of the chemical surface groups on a dry ITO surface; (**B**) charge surface groups formation after the surface immersion in electrolyte

Thus, if cells adhesion has to be prevented, a repulsive force of at least 0.3 pN must be applied.

Influence of positive potentials

In order to determine the influence of an imposed positive potential (current) on the cell activity, in 17 mM buffer solution (SB), we first employed the setup with 3 electrodes (see Materials and Methods). *Dictyostelium discoideum* cells were introduced in the electrochemical chamber (see Fig. 3.16A) in SB and after the cells had adhered to the surface, a potential was applied at the ITO surface. In all experiments, involving SB solution, we did not observed any effects on the cells activity, even for the highest potentials applied at the ITO surface.

It is very well known (see Materials and Methods) that the ionic screening effect is decreasing with the decrease of the ionic strength (Debye radius is inversely proportional to the ionic strength). In view of these, we diluted ten times the buffer solution obtaining a 1.7 mM phosphate sucrose buffer solution (see Materials and Methods).

All the results presented here were obtained for 1.7 mM phosphate sucrose buffer.

The first important result was the observation that when a minimal potential of +1.5 V/Ag, AgCl (I = 10^{-3} mA for 20 s) was applied, the cell membrane became black (Fig. 3.16B, black arrow) as observed by RICM (see Material and Methods). Given RICM interferential laws we attributed this phenomenon to a close contact between cell membrane and the ITO surface, which could suggest an attraction phenomenon.

Moreover, during the potential application and even after, the contact surface decreased and became round. Moreover, the frequency and the number of protrusions were drastically diminished or even stopped for a definite period (*impairment or delay of dynamic activity*, see also Table 3.1). *Recovery time* is defined like the period between the end of the electrical pulse and the moment when the cells revival their initial dynamic activity. The dynamic activity impairment is shown by RICM images for a 1V potential pulse during 60 s (Fig. 3.16C) and by Phase Contrast (PC) images after 60 s for a 2V pulse application (60 s) (Fig. 3.16E).

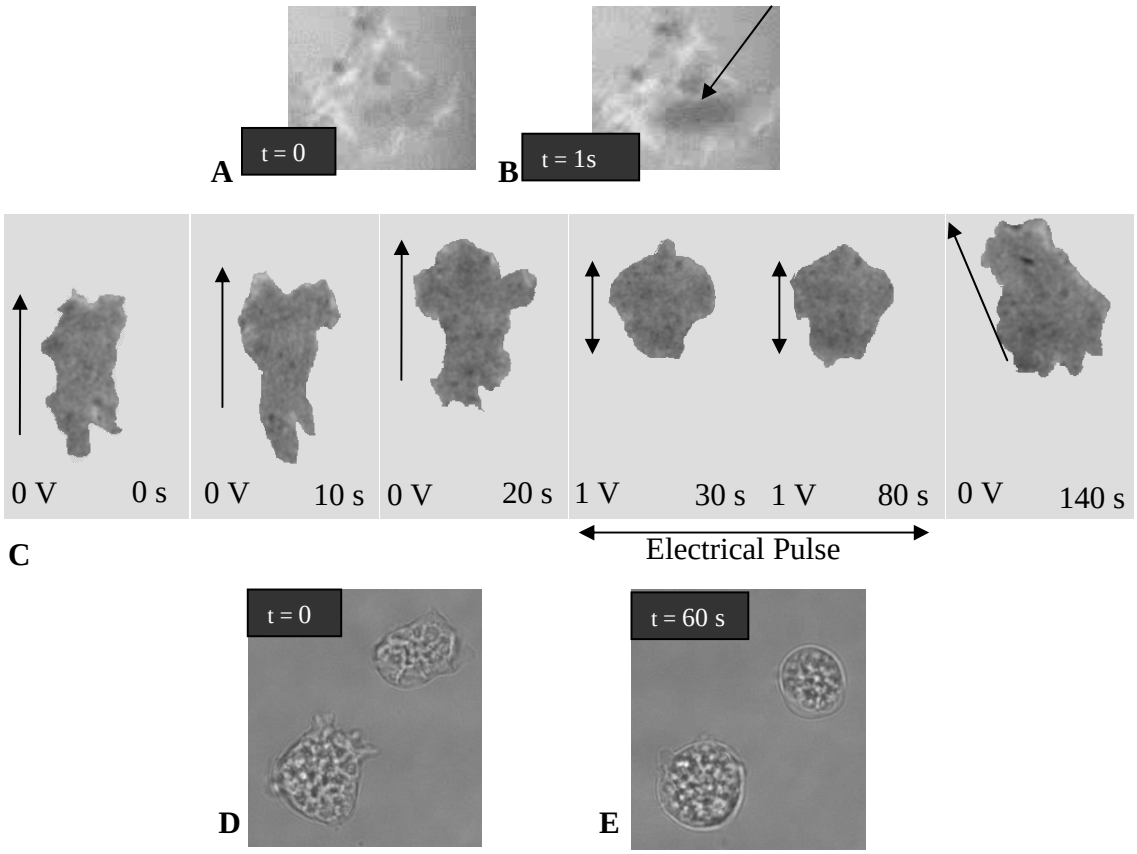

Fig. 3.16 Successive images (A, B) showing the close contact between the membrane and the surface; (C) RICM images of a cell showing the delay in cellular activity when 1V potential pulse during 60 s is applied (the arrows indicate the moving sense; double arrow indicate a stagnation); (D) and (E): successive phase contrast (PC) images before and after 60 s for a 2V pulse application (60 s).

We summarize the results of the experiments in two tables. The first one (Table 3.1) shows the cellular responses as a function of electrochemical parameters when a positive potential was imposed, in 1.7 mM phosphate sucrose buffer.

Table 3.1. Cellular response as a function of positive potentials at the ITO substrate

	1	2	3	4	5
	Imposed	Measured	Calculated	Observations	
	Potential (V/Ag, AgCl) and time of application (s)	*Current average intensity (mA)*	*Minimal pH value*	*Attractive electrostatic effect Attraction Max:+++*	*Cellular dynamics and motility*
1	+2.5 (2 s)	$+4*10^{-1}$	*3.1*	+ + +	*no delay of activity*
2	+2 (60 s)	$+3*10^{-2}$	*3.4*	+ +	*activity stopped, cells remain glued on the surface*
3	+1.5 (20 s)	$+5*10^{-3}$	*4.4*	+	*delay of activity, recovery after 150 s*
4	+1 (60 s)	$+1.5*10^{-3}$	*4.7*	no effect	*delay of activity, recovery after 60 s*
5	+1 (30 s)	$+1.5*10^{-3}$	*4.85*	no effect	*delay of activity, recovery after 17 s*
6	+0.8 (120 s)	$+5*10^{-4}$	*5*	no effect	*limit of delay of activity*

The minimal pH value reached during the potential pulse was calculated by Comsol simulation taking into account the diffusion of the generated protons ($D = 10^{-4}$ cm/s^2) but not considering the proton or hydroxyl migration in the created electric field (their concentration is lower than that of the salts composing the buffer). After application of the potential, the proton production is stopped and the system homogenizes by diffusion.

It can be observed that minimum value of the potential for which an effect on the cell's activity can be observed (Line 5) corresponds to pH = 4.85, which is close to the p.z.c of ITO surface.

If we compare lines 2-6, we observe that recovery time of cellular activity increases with the decrease of the minimum pH value. For short duration time of potential pulse (line 1), we notice that even for lower pH (so higher protons concentration), no sign of cellular dynamics impairment was observed. One can deduce that a longer exposure to an acidic pH affects cell activity more importantly (the activity can be stopped definitively, see line 2).

If we compare now column 1 and 4 one can notice that the membrane attraction to the surface increases with the value of the imposed potential. Regarding the calculated pH values, we can notice that the attraction force increase correlates with an increase of the maximal concentration of produced positive ions (protons). Thus, we suggest two factors who could contribute to this phenomenon: 1) The negative charges of ITO surface (pH depending, see fig. 2.16) and cell membrane are neutralized by the produced protons during the application of the positive potential; the repulsive force being diminished the cells could contact the surface. 2) The second factor takes into account the electrophoresis transport of charged microparticles (cells), the cells moving in the created electric field with much lower speed (1 μm/s in a 1V/m electric field for a cell of 10 μm in diameter (Gingell, 1976)) than lighter and more mobile negative charged ions (migration).

In conclusion, the cells seem to be attracted on the surface if the pH value is lower than 4.7 and seem to tolerate short (1 to 5 s) positive potentials.

The role of calcium in cell dynamic activity

The Ca^{2+} ions have an important role in the dynamic activity of the cells, as can be observed in the Table 3.2.

Table 3.2. Cellular response as a function of positive potentials at the substrate, in 1.7 mM phosphate sucrose buffer + 100 μM Ca^{2+}

1	2	3	4	5
Imposed	Measured	Calculated	Observations	
Potential (V/Ag, AgCl) and time of application (s)	*Current average intensity (mA)*	*Minimal pH value*	*Attraction electrostatic effect Max:+++*	*Cellular dynamics and motility*
+1.5 (20s)	$5*10^{-3}$	*4.4*	+	*no effect on the cell's activity*
+2 (50s)	$3*10^{-2}$	*3.45*	+ +	*delay of activity, recovery after 10 - 90 s*
+2.3 (50s)	$2*10^{-1}$	*2.6*	+ + +	*activity stopped, cells were glued on the surface, some cells recover after 10 minutes*
+2.5 (50s)	$4*10^{-1}$	*2.3*	-	*explosion of the cells*

In comparison with the Table 3.1, we can notice (see column 3 and 5, Table 3.2) that the cells in the presence of Ca^{2+} are more active after a long exposure to a low pH. Regarding the attraction force, it did not change with Ca^{2+} concentration (see column 1 and 4, Table 3.1 and 3.2). We can notice that if the pH value decreases under 2.5 and the cells were submitted to such low pH for longer time than 50 seconds, the cell membrane is destroyed.

Influence of the negative potentials

We have seen that positive voltage pulse induce blackening of the cell membrane. On the contrary application of a negative potential of -1 V/Ag, AgCl ($I = -10^{-2}$ mA for 5 s) results in white spots which appeared on the surface of the cells in the first two seconds during the application of the negative potential (Fig. 3.17B). When the potential application time was extended to more than 60 s (see Table 3.3), the cell activity was also impaired.

Based on the RICM laws, we attribute the apparition of the white zones to an uplifting of the cell membrane from the surface, which suggests the apparition of a repulsive force between cell membrane and the ITO surface. Note that this uplifting is a not uniform, large aria of cell membrane remains dark (Fig. 3.17B)

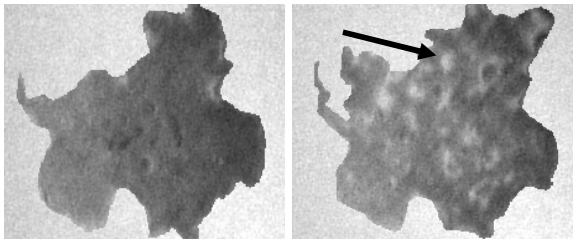

A **B**

Fig 3.17 Succession of RICM images before (A) and during (B) -1 V pulse application. In the first second of the pulse application white spots appeared (one of these is pointed by a black arrow) at the membrane-surface interface (B).

When a negative potential was applied, the cells in 1.7 mM phosphate sucrose buffer had different responses in function of the time of potential application (Table 3.3).

The minimum value of potential for which we obtained an effect on the cells dynamics was -0.5 V/Ag, AgCl, if the application time is greater than 60 seconds (line 1).

Table 3.3. Cellular response as a function of negative potential at the ITO substrate

	1	2	3	4	5
	Imposed	Measured	Calculated	Observations	
	Potential (V/Ag, AgCl) and time of application (s)	*Current average intensity (mA)*	*Maximal pH value*	*Repulsion electrostatic effect Max:+++*	*Cellular dynamics and motility*
1	-0.5 (60 s)	$-1*10^{-3}$	*9*	no effect	*delay of activity, recovering after 15 s*
2	-1 (100 s)	$-1*10^{-2}$	*10*	+	*delay of activity, recovering after 60 s*
3	-1 (5 s)	$-1*10^{-2}$	*9.6*	+	*activity is not affected*
4	-1.3 (5 s)	$-2.8*10^{-2}$	*10*	+ +	*activity is not affected*
5	-1.5 (5 s)	$-5*10^{-2}$	*10.3*	+ + +	*activity is not affected*

If we look at line 2 and 3, we can notice that for the same potential and current intensity value and for a significant difference of application times we obtained the same repulsion effect and an important delay of activity when the cells are exposed for a long time to a high pH (see column 3 and 5).

The repulsion of the membrane from the surface is related to the potential and current intensity values (line 3, 4 and 5).

For potential application times of a few seconds (1 to 5 s) and if the maximal pH value is smaller than 10.3 during the potential application, no visible cellular activity impairment was observed (see lines 3, 4 and 5, column 5).

We can attribute the membrane repelling from the surface to repulsive effect of negative surface charges and to electrophoretic force, helped by the rupture of adhering bonds by alkaline pH.

Are the cells affected by the positive or negative potential application?

In order to test the cell viability during the potential application on ITO surface, experiments with IP (propidium iodide) were performed. Thus, for maximal potential and

current intensity (+2.5 V/Ag, AgCl, I = $5 \cdot 10^{-1}$ mA for 5s and -1.5 V/Ag, AgCl, I = $-5 \cdot 10^{-2}$ mA for 30 s respectively) no damage of the membrane was observed. In both experiments, we identified one cell among 10^3 that was suspected for membrane damaging, similar percentages were found without using a potential pulse.

Can we prevent cell adhering on ITO using a negative potential and synchronize their spreading?

Even at the maximal value of the negative potential which can be imposed on ITO material (-1.5 V/Ag,AgCl for 30 s, $-5 \cdot 10^{-2}$ mA current), cells already adhering to the surface in 17 mM or 1.7 mM phosphate buffer could not be detached from the surface. Sedimenting cells also adhere despite a high negative potential which was applied on the ITO surface. So, the accumulation of negative charges of ITO surface (pH depending, see fig. 2.16) being less significant, also the electrophoretic effect was not sufficient to inhibit cell surface contact and spreading.

Thus, a new approach was taken into consideration: uses other conductive materials allowed us to impose higher potentials (and higher currents) in 1.7 mM phosphate sucrose buffer without destroying the substrate.

3.2.2 Influence of the electric field on the cells deposited on other conductive materials (Ti, Au and Pt)

Titanium surface

Deposited on a thin glass surface covered with Ti (see Materials and Methods), the cells in 1.7 mM buffer solution, were submitted to +2 V/Ag, AgCl (I = 10^{-1} mA, 1 minute). Even for long exposure time (1 minute), no cell attachment was observed but a very short delay of the cell dynamic appeared (Fig. 3.18C); we presume that in this case all faradaic current was mainly due to the titanium oxidation (the surface becomes transparent, fig. 3.18B) involving the following steps:

$$Ti - 2e^- \Leftrightarrow Ti^{2+} \quad E^0 = 1.63\ V/SHE$$

$$Ti^{2+} - e^- \Leftrightarrow Ti^{3+} \quad E^0 = 0.368\ V/SHE$$

$$Ti^{3+} + H_2O - e^- \Leftrightarrow TiOH^{3+} + H^+ \quad E^0 = 0.055\ V/SHE$$

In this case, protons are produced in a fourth lesser amount than when water electrolysis occurs on the ITO surface at the same potential difference. This could explain the absence of effect on cellular dynamics. A strong cell attraction effect was not observed because of the dissolution of the titanium film, which possibly created a natural convection effect, accelerating the dissipation of proton gradient.

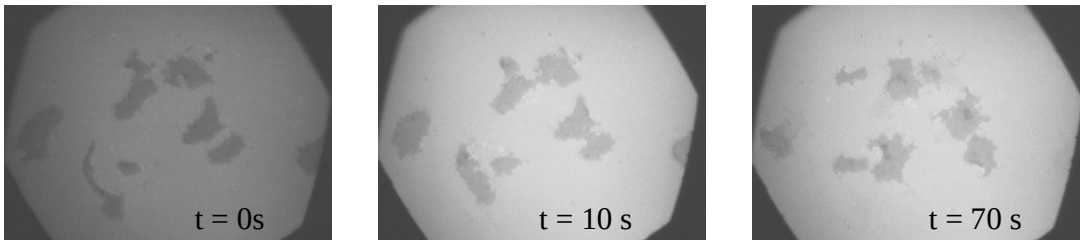

A **B** **C**

Fig. 3.18 RICM images showing the relative contrast changes during experiment. (**A**) adhered cells on Ti surface at the beginning of 2 V/Ref. pulse application (60 s) (**B**) only after 10 s it can be observed a contrast change (background becomes brighter) without effect on the cell dynamic (**C**) 70 s after the pulse, the cells are apparently no affected by the formed protons.

When we applied in 1.7 mM phosphate sucrose buffer, a negative potential (-3 V/Ag, AgCl, I = $-5 \cdot 10^{-1}$ mA for 1 minute), to the titanium surface, the inner zones were pushed away from the surface (Fig. 3.19B). 60 seconds after the pulse onset, the cell contact area on the substrate decreased very much, the cellular edges being pushed away from the surface (Fig. 3.19C). 30 seconds after the end of the potential application the cells restored their initial state and dynamics (Fig. 3.19D). A total detachment was not obtained. The cells did not explode despite a high current intensity. In addition, the point of zero charge (p.z.c.) of TiO_2 is 6 (Pierre, 1998). All these suggest a high capacitive current due to the thick porous oxide layer (Schneider, 2009). Thus, less HO^- ions are produced by applying a negative potential, compared to ITO. In the same time, the electrophoretic forces acted to detach the cells.

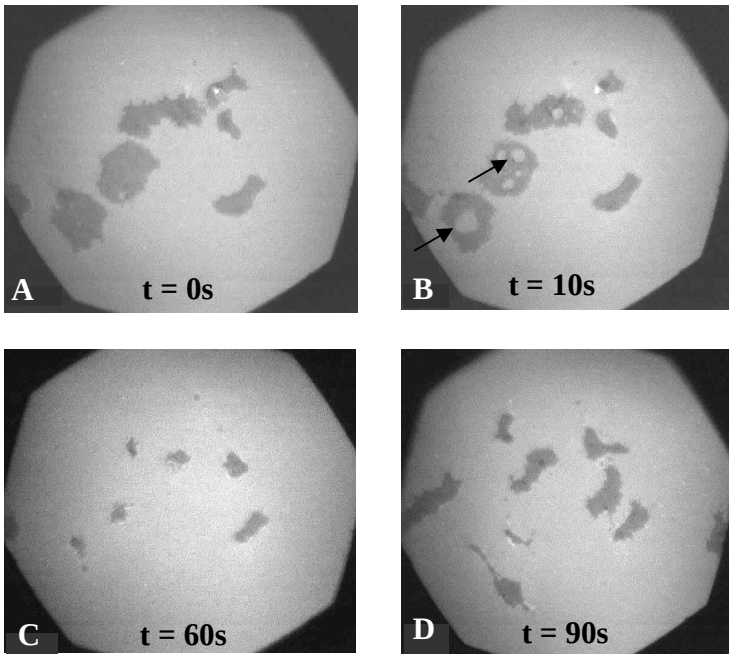

Fig. 3.19 RICM images for (**A**) before (**B, C**) during and (**D**) 30 s after the end of a -3 V/Ag, AgCl ($I = -5 \cdot 10^{-1}$ mA) negative potential pulse application on Ti surface (contrast was modified for a better visualization)

Platinum and gold surfaces

In order to increase the current intensity, so to increase the electrophoretic force, platinum and gold surfaces were prepared (see Materials and Methods). These materials indeed exhibit no oxide layer in standard conditions.

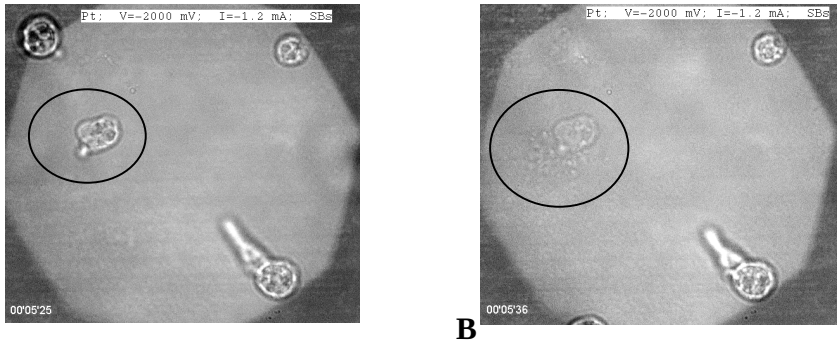

A **B**

Fig. 3.20 Phase contrast (PC) images (**A**) before and (**B**) during the cell explosion (ellipse); a -2 V/Ag,AgCl potential was applied on a Pt surface.

The cells were submitted to -2 V/Ag, AgCl negative potential, (I = 1.2 mA for 1 minute). Because of the high current intensity (platinum is a catalyst for water reduction), a large amount of HO^- is produced and, after only 1 minute, the adhered cells exploded (see figure 3. 21B, ellipse).

The same explosion effect was also observed when cells were submitted to a strongly basic NaOH 10^{-2} M solution during 1 minute.

Conclusions

Using different conductive materials (ITO, Ti, Pt and Au) we tried to detach the adhering cells in 17 mM and 1.7 mM buffer solutions or to impair their contact with the surface by imposing a negative potential (current) at the material surface while they are falling under the gravity. Even for the highest negative potentials the materials or the cells can support, we did not prevent cell adhesion.

In order to synchronize cell spreading, a new approach was then taken into consideration:

- in a first step we will keep the living cells in suspension at a certain distance from the surface (*d*, in Fig. 3.21) by decreasing the ionic strength of the buffer solution (the osmotic pressure was kept at 36 mOsm by adding sucrose) and so, this will increase the repulsive force (F_e).

- in a second step we will induce cell contact and spreading on the surface either by increase of the ionic strength or by electrochemical means.

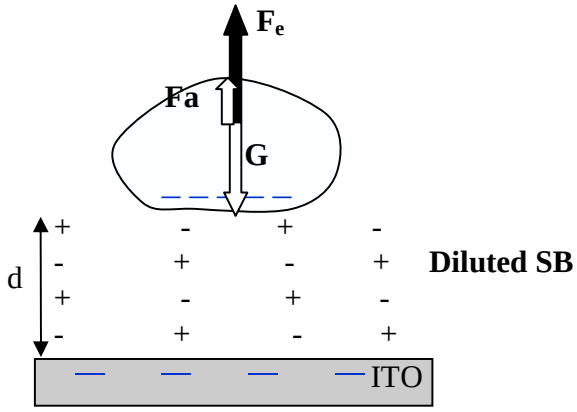

Fig. 3.21 Scheme of a levitating cell; the electrostatic repulsion prevents the cell adhesion.

3.3 Control of cellular adhesion by changing buffer concentration, salts nature or by surface chemical treatment

3.3.1. Electrostatic repulsion between *D. discoideum* cells and a glass surface

Introduction

In order to synchronize cell spreading, a new approach was taken into consideration: to keep the living cells in suspension at a certain distance from the surface, despite the apparent gravity (G_a). It is very well known that the ionic screening effect which decreases with decreasing of the ionic strength (Debye radius is inversely proportional to the ionic strength) influence cell adhesion (Gingell, 1976, 1982; Trommler, 1985). Wolf and Gingell (1983) studied the effect of dilution on unfixed red cells pre-adherent to glass in isotonic solutions and got interferometric evidence for spatially uneven separation on dilution. Cells that settle at low ionic strength make smaller and more uniform contacts with glass than do cells that initially settle at higher ionic strength and are then subjected to dilution.

Vigeant and Ford (1997) evaluated whether the attractive potential component considered in the DLVO method could explain the reversible adhesion of *E. Coli* bacteria to the glass surface. They did not find quantifiable changes with ionic strength for either the tendencies of individual bacteria to approach the surface or the overall times bacteria spent near the surface but, they did observed that the diameters of the circles which the smooth-swimming bacteria traced out on the glass increased in low ionic strength solution.

According to these results, decreasing the ionic strength of the buffer solution (the osmotic pressure being kept at 36 mOsm by adding sucrose), could increase the repulsion force (F_e) and then equilibrate the apparent gravity at a given distance *d* (Fig. 3.22).

The strength of ionic interaction forces in solution depends on the surface charge density and on the Debye radius (or Debye distance). The first one depends on pH for the oxide materials and the second one depends on the ionic concentration of the solution and on the nature of ions, at a given temperature.

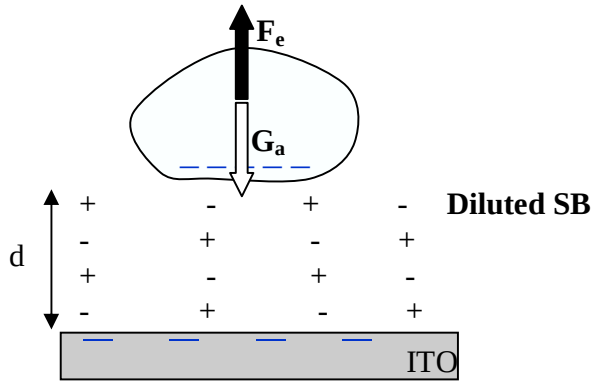

Fig. 3.22 Scheme of a levitating cell; the electrostatic repulsion prevents the cell adhesion; $\mathbf{G_a = G - F_a}$.

Dilution effect on Dictyostelium cells

D. discoideum cells exhibit a negative charge in a physiological solution *ie* a phosphate buffer (SB, see Materials and Methods).

It is known that glass surfaces are also negatively charged (20). In order to quantify these surface charges we measured the zeta potential for the living cells and different surfaces in SB solution (Table 3.4). The zeta potentials for the surfaces were deduced from the measurements of the streaming potentials (see Materials and Methods). Although the method does not apply to conductive surfaces, our ITO material is a doped semiconductor with a resistance of 20 Ω·cm, for which zeta potential measurements in 10^{-2} M 1: 1 electrolyte solution reflect the real values with a good accuracy.

Table 3.4 Zeta potential of different substrates and for the *Dictyostelium* cells in SB (pH = 6.13)

Substrate	PMMA	APTES	Glass	NaOH Treated Glass	ITO	Active cells	Latrunculin-treated cells
Zeta Potential (mV)	-32±3	+1±2	-20±5	-31±4	-16±5	-17±3	-18±2

The glass surfaces treated with aminopropyltriethoxysilane (APTES) have a positive zeta potential which can be explained by the apparition on the surface of ammonium cations ($R\text{-}NH_3^+$) in contact with the electrolyte. The ITO material and the

borosilicate glass have approximatively the same negative zeta potential, thus the same negative surface charge due to hydroxyl groups (R-OH) which in contact with an electrolyte form negative groups ($R\text{-}O^-$) in equilibrium with the solution (pH depending). A chemical treatment of the glass substrate with NaOH 14.5 M for 5 minutes (see Materials and Methods) increases the number of surface hydroxyl groups. The polymethylmethacrylate (PMMA), the reference material in this method, exhibited the grater negative zeta potential.

In view of varying the electrostatic repulsion between the cell membrane and the surface, we first studied the effect of salt concentration, giving that the ionic screening effect decreases with the decrease of ionic strength. The latter depends both on the ionic ratio of the salt and on its concentration (Gingell D., 1982). We used sucrose to maintain a constant osmotic pressure (Materials and Methods).

Phase Contrast was used to localize cells and Reflection Interference Contrast Microscopy (RICM) to monitor their relative position to the glass surface.

On a glass coverslip, in 17 mM phosphate buffer containing mainly monovalent KH_2PO_4, all cells adhered to the surface (Fig.3.23A). It can be observed that they are surrounded by a bright fringe (inset of Fig. 3.23A, pointed by arrow)

At 0.17 mM phosphate concentration, we observed the presence of round spots that are brighter than the grey background and which are surrounded by a dark fringe (inset of Fig. 3.23B and cell **1** from Fig. 3.23C). Such effects suggest the presence of cell membranes at a minimum distance of 100 nm from the surface (impair multiple of a quarter of the wavelength of the incident light divided by the refractive index of cytoplasm, see Material and Methods). The bright spots were not fixed which indicate that the cells were submitted to Brownian motion, but on average, they remained on definite location and at definite distance from the surface. These cells can be easily displaced by moving the experimental setup or creating a small turbulence in the medium.

The brightness of these spots continuously changed between gray and white, showing that no adhesion takes place. Although the cells remained near the surface, they did not succeed to start the adhesion process. When decreasing five times the concentration of the 0.17 mM buffer solution, we obtained a different RICM image for the levitating cells, which is now darker than the grey background (cell **2** in Fig. 3.23C).

When decreasing ten times the concentration of the 0.17 mM buffer solution, RICM image (cell **3**) shows the almost the same optical characteristics like initially.

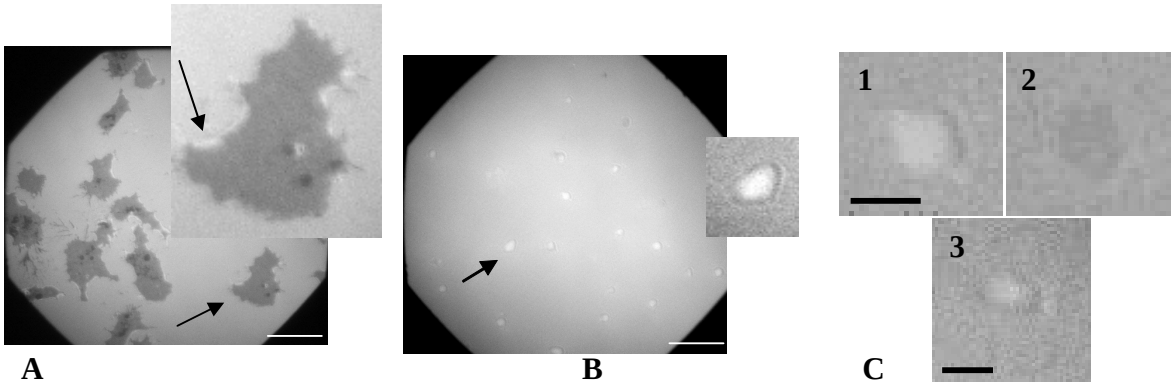

Fig 3.23 A, B: RICM images of *D. discoideum* cells on glass, in 17 mM (A) or 0.17 mM (B) phosphate concentration (insert : magnification of the area pointed by the arrow). Bar length = 20 μm. (C) levitating cells in 0.17 mM (cell **1**), 0.034 mM (cell **2**) and 0.017 mM (cell **3**), Bar length = 1 μm.

In the above figure, the RICM contrast difference of the levitating cells in the three buffer solution suggests that the distance between cell membrane and the substrate is different at 0.17 mM, at0.034 mM and at 0.017 (see Discussion).

Quantitative measurements of the percentage of adherent cells as a function of concentration and nature of the ions

When the ionic concentration was raised, cells were able to come into close contact with the surface and spread onto it, as revealed by the appearance of dark spots that enlarged gradually. The percentage of cells able to spread on the glass surface during 10 minutes increased sharply with the phosphate buffer concentration between 0.4 and 1.2 mM (Fig. 3.24).

Under a critical ionic concentration, 0.7 mM for SB, more than 50% of the cells levitate over the glass surface (Fig. 3.24). At 1.2 mM phosphate buffer, it takes 10 minutes for all cells to spread, and this time is reduced to 7 s at 1.7 mM.

Therefore, an increase in ion concentration speeds up cell spreading. On the other hand, the nature of the salt solution plays a significant role, as shown by the shift and the

steepness of the cell spreading response to $CaCl_2$ concentrations (Fig. 3.24, black diamonds).

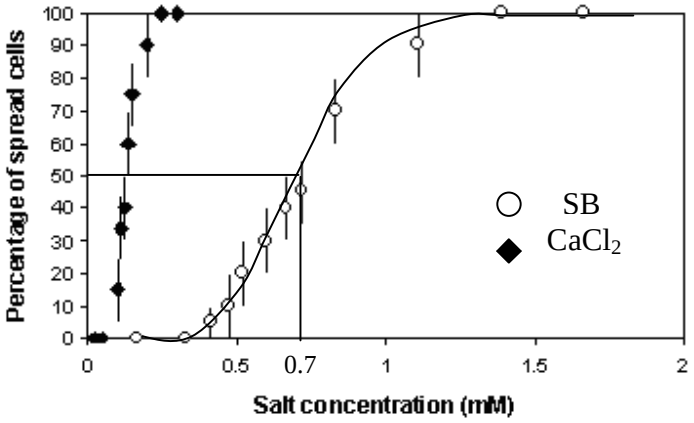

Fig 3.24 Percentage of *D. discoideum* cells spreading onto glass during a contact time with the surface of 10 minutes, as a function of calcium chloride concentration (full diamonds) and phosphate buffer concentration (open circles).

Divalent ions were more efficient than monovalent ones, since cells adhered at salt concentrations comprised between 0.05 and 0.25 mM $CaCl_2$.

When cells, previously spread on glass in 1.7 mM phosphate sucrose buffer (Fig. 3.25A), were submitted to a reduction of the surrounding ionic concentration down to 0.17 mM at a constant osmotic pressure, they remained attached to the surface, but the brightness of the contact area monitored by RICM slightly increased (Fig. 3.25B). Since the sucrose concentration is almost constant, the refraction index of the solution remains unchanged.

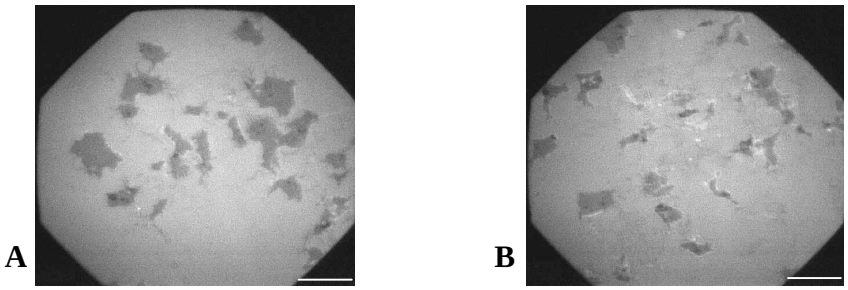

Fig 3.25 RICM images of *D. discoideum* cells on glass, in 1.7 mM phosphate sucrose buffer (**A**) and after dilution of the same sample to 0.17 mM (**B**). Bar length = 20 µm. Time between **A** and **B** is 150 s.

Therefore, the variation in the grey level is due to an increase in the distance between the cell and the surface (10-50 nanometers). Under these conditions, protrusive

activity still occurred along the cell margin, as indicated by the presence of fluctuating white areas around the central stable dark zone.

The extent of dark cell-surface contact area was slightly reduced, but all cells remained attached to the surface. Cells are even able to move on the surface, forming new contact zones despite electrostatic repulsion (figure 3.25A and B represent the same cells, B was taken 150 seconds after A). Taken together, these observations show that binding of the cell membrane to the surface, but not full detachment, is sensitive to the nature and the concentration of ions (Wolf, 1983).

In view of all these experiments, we examined whether, besides the existent electrostatic repelling between the cell membrane and a negative charged surface, the specific nature of ions or molecules in experimental solutions surrounding the cells also influence cell adhesion.

Is there a specific role played either by Na^+, K^+ or both cations ?

It could be envisaged that a specific ionic channel for Na^+ or K^+ could be responsible for cellular adherence. A specific role for H^+ channel is out of question because the two buffer solutions that fully allow or prevent cell spreading (17 mM phosphate buffer and respectively 0.17 mM sucrose phosphate buffer) have approximately the same pH (6.1 and 6.3, respectively). We, thus, prepared two buffer solutions that contain only one type of cation: one solution was made of NaH_2PO_4 and Na_2HPO_4 (we denominated it for simplicity, SB-Na) and the other one of KH_2PO_4 and K_2HPO_4 (SB-K) in the same ratio as for Sörensen buffer (SB). The pH values of SB-Na and SB-K were 6.07 and 6.00, respectively. The cells adhered normally in both 17 mM buffer solutions, whatever the nature of the cation is. Supplementary experiments with four completely dissociated salts were performed. These ones were composed of different types of cations and anions and do not contain the phosphate group: NaCl (pH = 5.85), KCl (pH = 5.6), CsCl and $LiClO_4$. In each case, the cells adhered normally. Thus, the hypothesis of the existence of a specific mechanism involving sodium, potassium or phosphate ions was rejected.

Therefore, in conclusion, the cellular adherence seems to be energy involved in close contact under the control of the electrostatic repulsion between cellular membrane and substrate and is not the consequence of a biochemical process involving specific ions or ion channels.

Could sucrose play a role in electrostatic repel ?

Another possibility would be the impediment of ion transport or cell movement by sucrose. Thus, we replaced the sucrose with a small organic molecule: a hydrophilic amino acid cysteine. We prepared a buffer solution of 0.17 mM diluted SB, maintaining osmotic pressure constant by using cysteine. As the cells were levitating in this buffer, we concluded that the sucrose did not interfere in cellular adherence.

Moreover, we choose two big organic molecules, soluble in water, to replace the sucrose and prepare 0.17 mM buffer solutions: MES (2-(N-morpholino)ethanesulfonic acid, pKa = 6.09) and HEPES (4-(2 hydroxyetyl)-1-piperazineethane sulfonic acide, pKa = 7.67) – Table 3.5, Column 3.

Table 3.5: **Organic zwitterionic salts replacing the sucrose**

Solution: type and composition	Inorganic Salt (C=17 mM)	Organic salts (concentration of inorganic salts 0.17 mM)		Combined solution
		HEPES [HEPES] = 36 mM	MES [MES] = 36 mM	MES+NaOH [NaOH] = 11 mM [MES] = 17 mM
Observations	The cells attach immediately	The cells didn't attach	Very few cells attached very slowly (after 2-3 minutes)	The cells attached immediately and exploded after 1-2 minutes

It can be noticed that the voluminous organic molecules could successfully replace the sucrose in view of maintaining constant osmotic pressure without helping the cellular adherence. The second column is shown as reference for the organic salts.

When we used MES + NaOH solutions, the cells become round and stopped to move because of the extreme pH values; the final concentration of NaOH ($5 \cdot 10^{-3}$) induced adhesion of all the cells on the surface (column 5).

3.3.2. Electrostatic attraction between D. discoideum cells and a APTES treated glass surface

In order to reverse the electrostatic interaction from repulsive to attractive we changed the glass surface charge by silanization (see Materials and Methods).

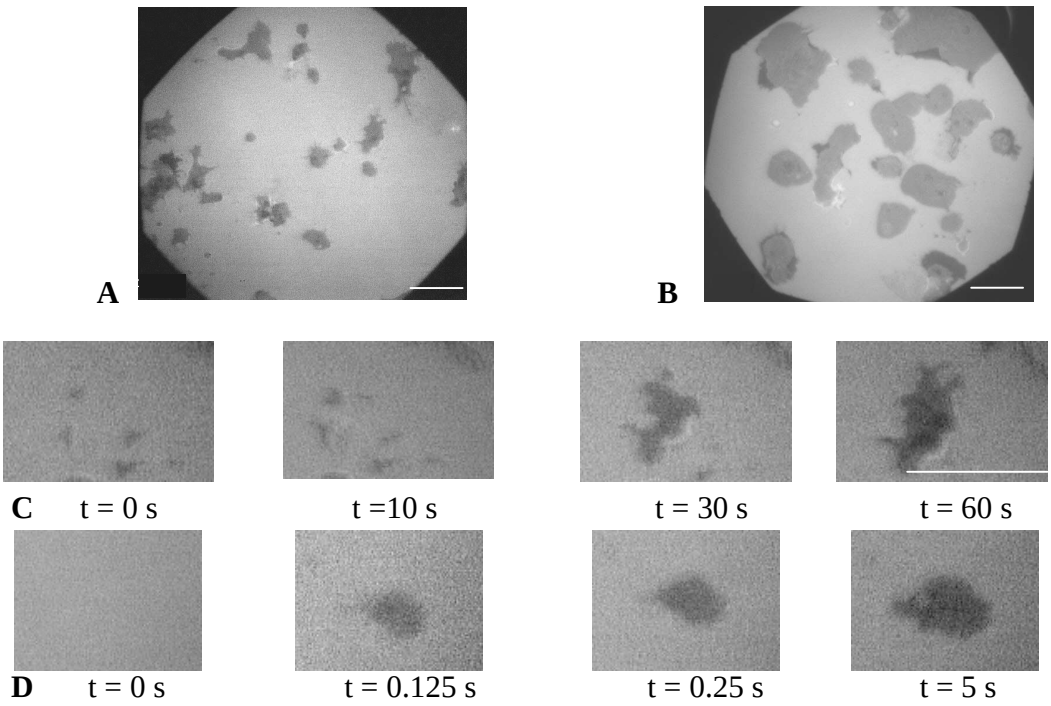

Fig. 3.26 Effect of ionic concentration on *D. discoideum* adhesion on aminopropyltrimethoxysilane treated glass. **A**, **B**: RICM images of *D. discoideum* cells on aminopropyltriethoxysilane (APTES) treated glass in 17 mM (**A**) or 0.17 mM (**B**) phosphate concentration. Bar length = 20 μm. **C**, **D**: Kinetics of cell spreading on aminopropyltriethoxysilane treated glass in 17 mM (**C**) or 0.17 mM (**D**) phosphate concentration. Bar length = 20 μm. The last image of each sequence is the maximal contact area of the spreading cells.

At physiological pH (6.1), aminopropyltriethoxysilane (APTES) replaced silanolate anions by ammonium cations. On this surface, cells spread whatever the ionic concentration is (Fig. 3.26A and B). Furthermore, at 0.17 mM, the cell-surface contact area increased faster than at 17 mM (Fig. 3.26C and D) and for most cells, the maximum area reached by the fully spread cell was larger (Fig. 3.26A and B). This shows that electrostatic interactions between the cell membrane and positively charged surfaces are significant at low ionic concentration and that they can be used to control cell adhesion.

As can be noticed, at low ionic concentration, positive surface charges exert forces strong enough to attract the cell to the surface and force spreading. After contact, about 20 μm^2 of cell membrane spread on the surface in less than 1 s, which is ten times the average spreading rate observed at physiological ionic concentration (Fig. 3.26D). This shows that electrostatic forces can be very strong at short distances, and thus be able to control cell adhesion.

3.3.3. Actin polymerization of *D. discoideum* cells in state of levitation

Is there an oscillating actin polymerization activity for levitating cells like in adherent cells ?

In order to follow the actin dynamics in LimE-GFP cells levitating over glass or ITO covered glass surface at 0.17 mM phosphate sucrose buffer, GFP fluorescence variations were recorded over time.

Fig. 3.27A shows sequential pictures highlighting different actin polymerization events (white arrows). Distinct fluorescence events appear randomly all over the cell and are moving with respect to the surface while visible. Fluorescence recording over time shows that actin polymerizes with peaks appearing more or less regularly (Fig. 3.27B).

The first three events are separated by 8.4 s whereas the time interval for the next event is 16.8 s, indicating that one event might be missing. Indeed, as the focal plane for fluorescence recordings was fixed, the levitating cell, which was continuously moving, was not fully accessible and fluorescence events out of this plane are not recorded. These experiments reveal that fluctuating actin polymerization occurs even in the absence of cell spreading. Some of these events might be related to endocytosis (see fluorescence peak at 55.2 s in Fig. 3.27A).

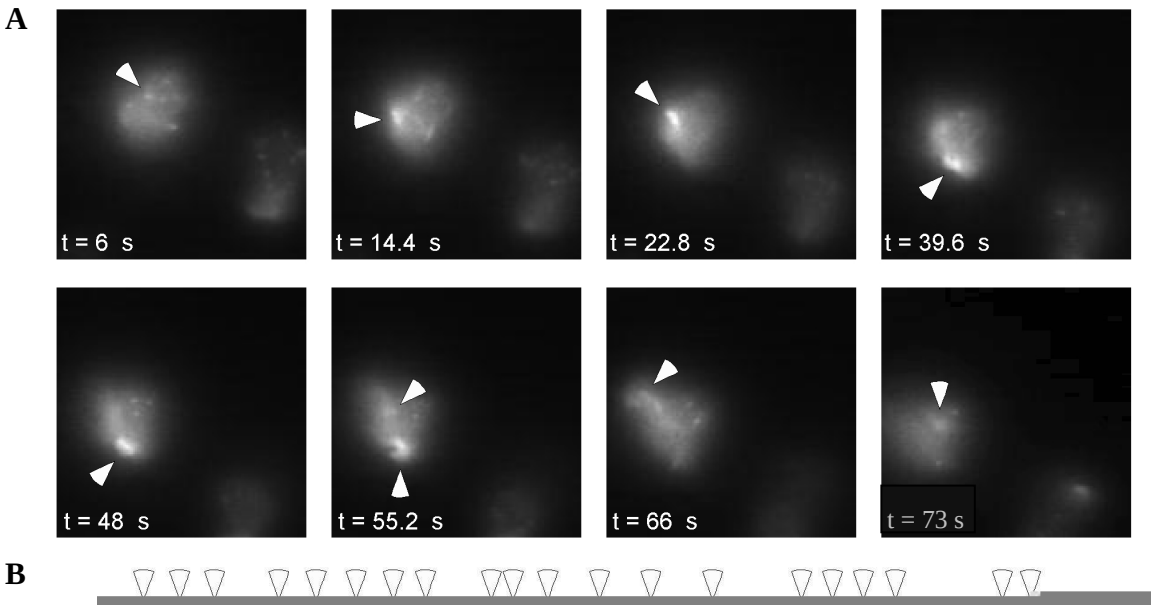

Fig. 3.27 LimE$^{\Delta coil}$-GFP fluorescence kinetics in levitating cells. **A**. Sequential images of *D. discoideum* expressing LimE$^{\Delta coil}$-GFP levitating in 0.17 mM phosphate sucrose buffer over a glass surface. Arrows indicate fluorescence maxima of individual events.
B. LimE$^{\Delta coil}$-GFP fluorescence variation as a function of time for the cell shown in (**A**). Vertical lines correspond to the same events highlighted in (**A**).

Analysis of 8 levitating cells, confirms more or less the existence of regular oscillatory actin polymerization activity during levitation. The origin of this activity will be discussed later.

In this subchapter, we showed how the living cells could be kept in suspension at a certain distance from the surface, despite the apparent gravity, using electrostatic properties of the cells and surfaces. In the following two subchapters, we analyze two different methods for adherence activation.

ERROR: undefined
OFFENDING COMMAND: ord

STACK: